# FLOW INDUCED VIBRATION AND NOISE CONTROL WITH FLOW

LIU YANG

Degree of Doctor of Philosophy

THE HONG KONG
POLYTECHNIC UNIVERSITY

2011

THE HONG KONG POLYTECHNIC UNIVERSITY

DEPARTMENT OF MECHANICAL ENGINEERING

# FLOW INDUCED VIBRATION AND NOISE CONTROL WITH FLOW

LIU YANG

A thesis submitted in partial fulfilment of the requirements for the Degree of Doctor of Philosophy

November, 2010

# Certificate of originality

*I hereby declare that this thesis is my own work and that, to the best of my knowledge and belief, it reproduces no material previously published or written, nor material that has been accepted for the award of any other degree or diploma, except where due acknowledgement has been made in the text.*

(Signed) ___________________

LIU YANG

NOVEMBER, 2010

# Abstract

The objective of this project is twofold. One is to understand the features and mechanism of the instability phenomena of the duct with flexible wall, and the other is to use the tensioned membrane to control noise source with flow such as fan noise in the duct.

In pursuing noise and wave control with minimal aerodynamic or hydrodynamic effect, a tensioned membrane backed by a cavity, namely the drum-like silencer, is used to partly line on the rigid duct wall. The membrane segment vibrates in response to the grazing incident sound and the vibration of the membrane acts as reflector to reflect the sound towards the noise source. The reflection of sound can be maximized at low-to-medium frequency range when the axial tensile force on the membrane is high to support the dominance of the first and second modes of vibration. The device has been tested successfully to achieve a good performance of transmission loss without flow and with mean flow at very low speeds. The effect of the flow on this device in practical usage has not been extensively investigated. In case of high flow speeds, tensile force on the membrane is highly increased in order to compensate and maintain the same amount of sound radiated energy. As a result, flow induced vibration is also observed at moderately high flow speeds and the unstable vibration of the membrane also generates much noise itself. Firstly, to

characterize the instability of vibration, direct measurement of the wall pressure fluctuation in the boundary layer is conducted as a preliminary to evaluate the characteristic and distribution of both aerodynamic and acoustic loadings on the membrane by using two-microphone with multiple measurement points. The experimental results revealed that the vibration of the membrane depends on the aerodynamic fluid loading rather than the acoustic loading. In order to allow for the free vibration at the lateral edge of the membrane in drum-like silencer for achieving effective sound radiation, there is an extremely small gap along the lateral edge which leads to the flow leakage through the gap. This is very crucial to the occurrence of vibration instability. In this regard, the aerodynamic effect on the vibration instability is investigated in details in case of the axial-flow and cross-flow directions. The instability phenomenon is found at the moderately high flow speed and it tends to disappear as the axial tensile force on the membrane is increased. Through a series of experiments, it is found that the vibration mode of membrane under the cross-flow condition will experience a three-stage process at different flow speeds: 1st mode of vibration at low flow speed, 1st and 2nd coupled modes of vibration at critical flow speed, and higher order modes of vibration at high supercritical flow speed. These findings are beneficial for the design of the membrane typed device and the method of clamping membrane in case of flow practically such as drum-like silencer so that the instability of the vibration can be avoided.

On the other hand, the configuration of the membrane with cavity can be used to reduce the strength of noise source directly instead of sound propagating path. This may share the same features of drum-like silencer but the working principle is different. The noise source is preferred to be dipole in nature and it can be an axial fan which is commonly used in the duct system. The noise suppression of it was successfully demonstrated both numerically and experimentally. The axial fan put at the middle of the membrane along the axial direction is regarded as the dipole source, which can induce the second mode of vibration of the membrane. The radiated sound from the membrane propagates towards upstream and downstream and is cancelled with the dipole source due to the full couplings between the vibration of the membrane and acoustic field inside the cavity. The two-dimensional simulation model is constructed to explore the sound and structure coupling as well as to understand the mechanism of the sound propagations, sound cancellation and the response of the membrane. The effects of several controlling parameters on the performance such as membrane length, the structure to air mass ratio and the tensile forces on the membrane are also investigated. From the view point of practical usage and installation of the fan, the performance of using membrane with cavity to cancel the axial flow fan noise is explored in a comprehensive three-dimensional simulation model. Optimization is conducted in searching the optimal shape of cavity for a given volume and for the optimal structural properties of the membrane. It is found that the optimal insertion loss can achieve more than 20dB over the frequency range of interest when the tension applied is low. It is much better than that by using expansion chamber with the same expansion ratio to control the dipole source. Besides, the experimental result agrees fairly well with the numerical prediction, showing the effectiveness and reliability of the numerical model. Apart from the effective control of noise source, the membrane lined on the wall can eliminate the pressure drop in the flow through duct and hence no extra power consumption of the engine is required and energy can be saved.

# Acknowledgements

I would like to express my deepest gratitude and appreciation to my chief supervisor, Dr. Yat-Sze Choy, for her inspirations and insights on the directions of my research project. I attribute the level of my PHD degree to her encouragement and support throughout my thesis. The thesis would not have been completed without her effort.

I am also deeply grateful to my two co-supervisors Professor Li Cheng and Dr. Lixi Huang, who give me the invaluable guidance and enlightenment that significantly strengthen my academic level and improve my research ability. Their suggestions broaden my knowledge and motivate me during the discussions.

I would also like to express gratitude to my friends Dr. Chunqi Wang, Mr. Lin Shao and Mr. Qiang Xi who offer assistance in my experimental work. In addition, the generous help from Mr. Chowning Tang, the technician in the acoustic lab and other technicians in the Project Lab is also appreciated.

Finally, I am grateful to my parents and my friend Hongning Kou for their everlasting love, warm care and everything.

# Table of contents

# List of figures and tables

# Nomenclature

| Symbol | Description |
|---|---|
| $A$ | Cross section area of the membrane |
| $A_0$ | Cross section area of the duct |
| $A_2$ | Cross section of the cavity |
| $A_n$ | Signal reading of microphone n before swapping, n=1,2 |
| $A'_n$ | Signal reading of microphone n after swapping, n=1,2 |
| $a_n$ | Acceleration of membrane vibration |
| $B$ | Rotor blade number |
| $c$ | Sound speed |
| $c_n$ | Modal phase speed |
| $D_f$ | Drag force of the fan |
| E | Young's modulus |
| $E_f$ | Radial force of the fan |
| $F$ | Force exertion of the dipole source |
| $f$ | Frequency |
| $f_1$ | Low frequency limit of the stopband |
| $f_2$ | High frequency limit of the stopband |
| $\Delta f$ | Frequency step in the calculation |
| $H$ | Heavside function |

| | |
|---|---|
| $h$ | Height of the duct |
| $h_c$ | Height of the cavity |
| $i$ | Imaginary unit |
| $J_n$ | Transfer function between signal voltage and the real sound pressure defined by $J_n = p_n / A_n$, where n=1,2 |
| $J_{n1}$ | Complex calibration factor between the nth microphone and the first microphone |
| $j$ | Index of vibration mode |
| $IL$ | Insertion loss |
| $IL_{cr}$ | Criterion level of the insertion loss |
| $IL_d$ | Insertion loss for the dipole radiation after decomposition |
| $IL_t$ | Total insertion loss |
| $IL_{up}$ | Insertion loss directly from the raw data |
| $k, k_0$ | Complex wave number, defined as $k = \omega / c$ |
| $k_n$ | Modal wave number |
| $L, L_m$ | Length of the membrane |
| $L_c$ | Chamber length |
| $L_d$ | Duct length at downstream |
| $L_j$ | Structural impedance of $j^{th}$ mode |
| $L_{up}$ | Duct length at the upstream |

| | |
|---|---|
| $m$ | Mass ratio of the membrane |
| $n$ | Local outward normal direction |
| $P$ | Pressure loading on the wall or membrane |
| $P_{rad}$ | Radiation pressure in the duct |
| $p$ | Acoustical pressure |
| $p_{cav}$ | Pressure inside the cavity |
| $p_d$ | Amplitude of the dipole part of the source |
| $p_{\exp}$ | Acoustical pressure at the exit of a straight duct |
| $p_m$ | Amplitude of the monopole part of the source |
| $p_s$ | Pressure of the sound source |
| $p_{str}$ | Acoustical pressure at the exit of the duct with the silencer |
| $Q$ | Monopole source |
| $q$ | Dipole source |
| $R_j$ | Complex amplitude of the radiated sound by the $j^{th}$ modal vibration |
| $r_f$ | Bandwidth of stop-band, defined as $r_f = f_2 / f_1$ |
| $S$ | Strut number |
| $T$ | Tensile force on the membrane |
| $T_f$ | Thrust force of the fan |
| $T_{opt}$ | Optimal tensile force |
| $t$ | Time |

| | |
|---|---|
| $U, U_\infty$ | Upstream mean flow speed |
| $U_c$ | Critical flow speed |
| $U_{con}$ | Convective flow speed, phase speed |
| $u$ | Particle velocity |
| $V$ | Vibration velocity of the membrane |
| $V_j$ | Amplitude of the $j^{th}$ mode |
| $V_{rms}$ | Root mean square of the vibration amplitude |
| $W$ | Total power radiation at the exit of the duct |
| $x, y, z$ | Cartesian coordinates |
| $\Delta x$ | Space between two electret microphones |
| $Z$ | Acoustic impedance |
| $Z_{cav}$ | Mode impedance in the cavity |
| $Z_{jl}$ | Modal impedance, $l^{th}$ mode coefficient of fluid loading caused by a bed $j^{th}$ vibration of unit amplitude |
| $Z_{rad}$ | Mode impedance in the duct |
| $\alpha$ | Cross radiation coefficient |
| $\beta$ | Reflection coefficient at the open ends of the duct |
| $\gamma_j$ | Modal radiation contribution |
| $\delta_{0n}$ | Kronecker delta function |
| $\varepsilon$ | Strain |

| | |
|---|---|
| $\eta$ | Displacement of the membrane |
| $\theta$ | Angle between microphone and the near side duct opening |
| $\lambda$ | Wave length |
| $\nu$ | Frequency index differential, defined as $\nu = m_f B - k_f S$ |
| $\xi$ | The distances between the measuring microphones and the reference microphone |
| $\xi_0$ | The distance between one fixed microphone and the reference microphones |
| $\tau$ | Time delay |
| $\phi$ | Velocity potential |
| $\psi_n$ | Modal velocity potential |
| $\omega$ | Angular frequency or radian frequency |
| $\omega_0$ | Fixed angular frequency |

# Chapter 1 Introduction

## 1.1 Review of the noise reduction methods in acoustics

The ventilation and air-conditioning systems play a significant role in providing comfortable environments, but there is a problem of noise, especially at the low frequencies. The low frequency component is very difficult to control. The noise can be propagated into the working area through the duct from the air handling unit. To control the noise effectively, there are three key elements to attenuate noise transmitted to the receiver and thus reduce the annoyance. The first element is to control the source which is the most effective solution. The second one is to control the sound in the propagating paths so that the noise can be prevented from being propagated and the last one is to reduce the noise at the receiver such as ear muff. The methods in controlling the noise in the sound propagating paths can be generally categorized into passive and active. The former method can be further classified as dissipative and reactive noise control methods according to their physical perspective.

The dissipative silencer in which there is sound absorption material is frequently utilized in the intake and exhaust ducts of gas turbines and ventilation ducts connected with industrial fans or cooling-tower installations. The noise is reduced through the dissipation of sound energy into heat by the relative friction motion between the air and the absorbing materials resulting from the oscillations of the acting sound pressure, the air molecules and their random thermal motion in the interstices of a porous material, such as carpet, draperies, spray-applied cellulose, aerated plaster, fibrous mineral wool and glass fibre, open-cell foam, and felted or cast porous ceiling tile. However, this type of silencer is usually bulky, costly, and ineffective at low frequencies. Besides, they usually have an allowable pressure and momentum loss and there are also environmental problems as fibres are exposed to flow trap dusts. On the other hand, active noise control (ANC), which is good at controlling low frequencies, produces sounds with same amplitude and anti-phase through electronic technique to interfere with the original sound so that the noise will be cancelled. Nevertheless, it remains difficult to implement such as the requirement for extra power and robustness in a given range of operating conditions.

The reactive means is used to control noise by sound reflection such as expansion chambers that remains attractive in noise control. These can be achieved by either the abrupt expansion/contraction of the cross-sectional area or a by-pass resonating chamber which consists of a cavity-backed opening and a panel for sound radiation at resonance. However, they are usually limited to narrowband and are ineffective at low frequencies. In order to widen the stop-band, Yi (1986) investigated a series of expansion chambers with a side inlet and outlet theoretically and experimentally. He also demonstrated the effect of high-order modes on the performance of the side-in/side-out type of a chamber with consideration of the offset inlet/outlet locations. Xu(2003) examined the performance of a finite-length cylindrical dissipative expansion chambers. The results showed that the performance is a function of the radius, sound-absorbing properties such as thickness and flow resistivity of the fibre. Besides, the increment of fibre thickness and area ratio of the inlet radius to the silencer radius at the junction would improve the performance at the high frequencies.

Helmholtz resonator is another classical device, where the air layer moves back and forth as vibration. The resonance frequency is determined by the speed of sound, the neck cross-section area, the neck length and the resonator volume. The transmission coefficient is zero which means reflection is totally baffled when resonating at the single frequency, so the efficiency is fairly high but with a narrow frequency band. Until now, Helmholtz Resonator still attracts many scholars to investigate and improve it in new ways; many adaptive techniques have been developed. Griffin (2001) computed the transmission loss (TL) of coupled Helmholtz Resonators. His works demonstrated that the TL was increased at the resonance frequency if the resonators had the same geometry but the overall performance was still limited to a narrow bandwidth. The combination of several Helmholtz Resonators with different sizes could widen the stop-band effectively. Afterwards, Kim (2005,2006) developed a novel silencer by serial and parallel arrangements of Helmholtz Resonators in the absence of mean flow both theoretically and experimentally based on mutual radiation impedance and reflection of the incidence acoustic energy and attenuation in the resonator's neck. It indicated that the amplitude of TL could be increased by the serial arrangement while the bandwidth of TL could be widened by parallel arrangement. To obtain maximum TL, the distance between the resonators should be equal to a quarter of its wavelength. This meant that the silencer with multiple resonators should be very long to reduce low frequency noise. Selamet (2004) investigated the acoustic performance of a concentric circular Helmholtz resonator lined with fibrous materials. The effects of the density and thickness of this material on the resonator behaviour were examined. The results showed that the resonance frequency and the peak value of the TL were decreased with increasing the thickness of fibrous material.

It is known that pressure/momentum loss always leads to the requirement for higher power consumption and higher cost, and the higher power also leads to extra noises from the flow driving system. Therefore, side-mounting silencer without insertion of any splitter in the middle of the main duct would be an ideal configuration for noise control device. To eliminate the sudden change of cross sectional area in the duct, Fuchs (1988) developed the membrane absorber which consists of the vibrating metal membrane and a lightweight metal honeycomb structure to absorb noise at resonance. Afterwards, Frommhold (1994) investigated the physical mechanism of such membrane absorber in detail and the influence factor on its performance. The membrane absorber was actually a combination of an array of Helmholtz Resonators which were covered by panels. There were two obvious peaks in TL spectrum. The two peaks were attributed to the resonance of Helmholtz resonator and vibrating plate. Fuchs further developed the patented device called ‘membrane absorber box’, which had a broadband performance in the low to medium frequency range. It is made by a host of combined Helmholtz and panel resonators in a honeycomb structure. A typical resonator unit consists of a rectangular cavity covered by a perforated membrane. Another impervious thin membrane was placed in front of the perforated membrane to form a narrow channel between the two sheets. The system of perforated panel with cavity resonates at a frequency about twice the resonant frequency of the Helmholtz system formed by the cavity and the aperture. The two resonance peaks are only weakly coupled. This device to control noise is by dissipation. Compared with the dissipative mechanism, the reactive mechanism of sound reflection is more effective in achieving a desirable TL in a duct system constructed mainly by membrane. Recently, Huang (2002) proposed such a wave reflection device in which flexible membranes were used to form part of the duct wall and the structure to air mass ratio was small. This is called drum-like silencer. As shown in Figure 1.1, it consists of a tensioned thin membrane backed by a slender cavity with a depth equalling to the duct height. When an incident sound wave propagates from the upstream-side of the duct and passes over the membrane, it will induce the membrane to vibrate. As a result, with a subtle coupling of the whole system, part of the acoustic waves is reflected back to the upstream-side due to the sound radiation from the membrane and the strength of acoustic wave propagating to the downstream side will be reduced.

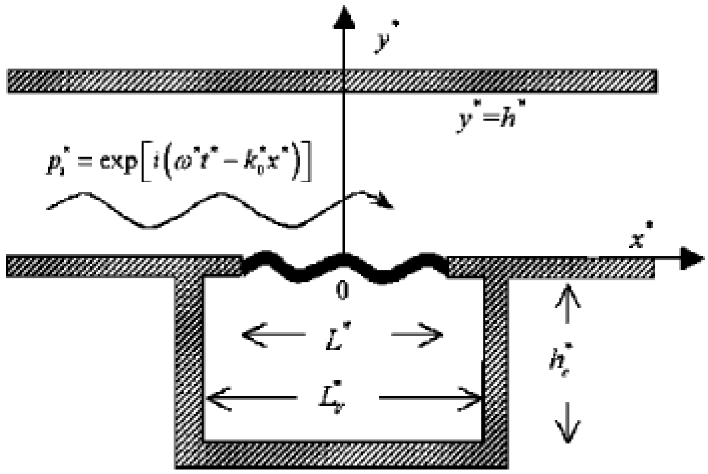


Figure 1.1 Schematic of the drum like silencer configuration (Huang, 2002)

The optimal results showed that the membrane with a length of five times the duct height can achieve a good performance from low to medium frequencies over an octave band. However, the optimal tension required to achieve good performance is high and it is difficult to be implemented practically. To minimize the sideway space, the cavity of the drum silencer was filled with helium gas and it was investigated through mathematical analysis, physical explanation, and experimental study by Choy (2005). Significant enhancement of noise reduction at low frequencies was observed when it was used with very shallow cavities. The light helium gas can release the massive fluid loading on the second *in vacuo* mode of the membrane and thus it helps to increase the noise reduction at low frequencies. But there will be many problems on the injection of helium gas practically.

In order to solve the problem of implementation, plate with high bending stiffness can replace the tensioned membrane. Huang (2006) proposed to adopt a plate with high bending stiffness and very low density which was used as a side-branch wave reflector to replace the tensioned membrane. The *eigen* frequency of the second *in vacuo* mode for plate vibration was changed to four times as much as that of first mode compared with twice for the tensioned membrane. For a given cavity volume, the widest stop-band for the configuration of using long plates with two free lateral edges parallel to with the duct axis has been found. Wang (2007) optimized it with the boundary condition of clamped support, which was easier to implement in practice. The results revealed that such a plate silencer could function effectively as a low frequency wave reflector over a broad frequency band, and a stop-band above one octave was achieved when the plate-to-air mass ratio was less than 3.5. The performance of the clamped plate silencer could be further enhanced by using plates with softer ends. This can be done by using non-uniform plate with different bending stiffness in different region. Optimization studies showed that, with a proper distribution of the bending stiffness along the plate, the widest stop-band of the clamped plate silencer might be up to $f_2 / f_1 = 6.0$ for a mass ratio of m=1, which was even wider than that of a simply supported plate silencer.

Furthermore, modification on the properties of the plate was made in order to provide better performance. For instance, the plate can be made of perforated surface. The acoustic behaviour of perforated facings was analyzed by Bolt (1947), the acoustics wave interaction between the holes of the facings will become significant if the spacing between holes was less than diameter of each hole. In this regard, micro-perforated structures were designed and developed for room acoustics by Maa (1975). Many new ideas such as non-fibrous, non-abrasive materials with non-polluting, almost closed and optically attractive surfaces had evolved from the pioneer work. With resource to the breakthrough of the innovative technology, now there are many improvements, for example micro-perforated panels (MPA), double layer MPA, mixed MPA with fibrous materials. Kang (1999) explored the combination of MPA and membrane based on the theories for both the membrane absorber, namely a limp lightweight tensioned membrane backed by an air space, and the micro-perforated absorber, namely a cavity backed plate with low aperture ratio but many apertures of sub-millimetre size, such as a glass-fibre textile or a micro-perforated membrane mounted over an airtight cavity. The effectiveness of one element relies on its relative impedance to the other. In other words, if the acoustic impedance of the apertures is much greater than that of the membrane, the absorption of the structure depends mainly on the characteristics of the membrane.

The apertures play a dominant role if their acoustic impedance is much less than that of the membrane. In order to improve the absorption capability, the acoustic impedance of the structure can be adjusted by varying the appropriate parameters of the membrane and apertures.

The proposed noise reduction technology in the duct is normally investigated in case of no flow. In reality, almost all the silencer should be used in case of flow such as air conditioning and ventilation system. Usually, the effect of flow is divided into two parts in the current study. The first is the effect of a uniform flow on the performance of silencer including the sound reflection capability. In other words, the physics behind the coupling between the fluid dynamics, acoustic waves and membrane becomes more complicated because of the extra fluid loading on membrane due to the moving fluid. The second is the effect of turbulence on the plate vibration. If the sound energy radiated from the turbulence is comparable to or even larger than the incident sound, the performance of the silencer greatly deteriorates, and this problem may be important in the air conditioning system with branches, tuning points and elbows.

For these two aspects, the effects of a mean flow and turbulent flow excitation on the performance of aforementioned drum-like silencer were examined by Choy (2005). For the flow speeds less than 15m/s in ventilation system, there was no flow-induced instability of vibration. Besides, the quantitative effect of flow on the silencing performance obtained both theoretically and experimentally was mainly the smoothing and the shifting of the peaks, especially the second peaks in the transmission loss spectrum. For the flow-induced vibration of the two dimensional membranes, both vibration and flow measurements were also carried out by Choy (2007). Several parameters were studied to find out the region for the occurrence of instability such as the tension and the upstream flow speed. The results revealed that there was no flow-induced vibration when the flow speed was either too low or too high. The phenomenon is described as below. For a given tension value, the flow-induced vibration occurred when the flow speed increased, however, it was interesting that the linear growth of the membrane responses will be observed when the flow speed is lower than 12m/s or higher than 18m/s. As shown in Figure 1.2, the exponential growth of the amplitude with respect to time is observed when flow speed varies from 12m/s to 18m/s. Otherwise, the vibration growth tends to be stable concerning the linear transition. Furthermore, the rigid-walled cavity which is beneath the membrane and outside the duct significantly influences the flow-induced vibration by shifting the velocity ranges of the instability.

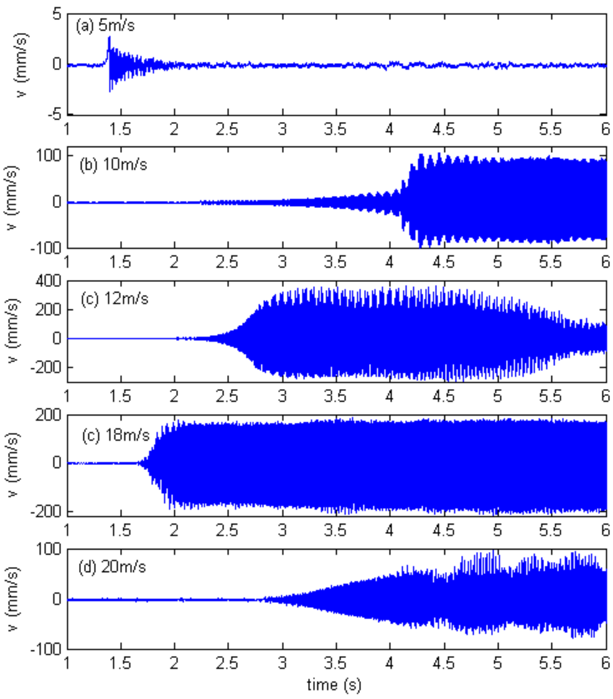


Figure 1.2 Time trace of the amplitude growth of the vibration at different flow velocities (Choy, 2007)

Although there are several aerodynamic phenomena observed in the experiments, only some of possible mechanisms for the flow induced vibration were discussed. Additionally, the vibration and noise in structures excited by turbulent boundary layer (TBL) flow on flexible surfaces is commonly seen in many applications such as pipe systems, aircraft structures and car manufacture. Duct walls in the air conditioning system are flexible to some extent. It is indispensable to study the extra sound generation associated with a realistic flow condition and explore the features of the turbulence wall pressure.

## 1.2 Motivations and objectives of current work

The objectives of the current project comprise two aspects. The first objective is to investigate the instability phenomenon occurred on the drum-like silencer. For the drum silencer in ventilation system, the combination of both the fluid and the acoustical loadings will influence the vibration of the membrane. To clarify this, the first task is to distinguish the pressure components of both acoustical and fluid loadings exerting on the membrane. Therefore, the characteristics of the wall pressure are investigated to determine the main controlling factor on the vibration of the membrane. Another proposed task for the further study is to understand the features of the vibration such as the influence parameters and its coupling effect of those parameters. It is believed that the vibration instability can be diminished and precluded with some modifications on the present configuration. The full understanding of the physical phenomenon serves as a fundamental research and will facilitate the design and modification in the practical application.

On the other hand, the second objective of the thesis, which is the most important part in the project, is to develop the noise reduction of a dipole source by using the silencer with tensioned membranes. Although it can be regarded as the extension work on the drum silencer in respect that it shares the same features of the silencer, the principal concept and methodology is quite innovative and independent. In more details, the configuration of the membrane with cavity can be used to reduce the noise source directly instead of sound propagating path. In fact, the noise source is preferred to be dipole in nature and it can be an axial fan which is commonly used in the duct system. By doing so, there are two specific steps throughout the study regarding the performance and mechanism of the dipole noise control by tensioned membranes. The first step is to establish the computation and simulation method of calculating the dipole noise abatement by the silencer with tensioned membranes in two-dimensional (2D) configuration. The optimization procedure on the performance is carried out to search for the optimal physical parameters of the structure and aerodynamic properties. The second step is to examine the performance of such kind of silencer in a three dimensional (3D) model, which is to be validated by the realistic experiment. The axial flow fan is employed as the dipole noise source. The numerical calculation results of the noise reduction are experimentally verified with the aid of the realization of the prototype silencers.

## 1.3 Review of wall pressure features in fluids and the instability of flow past the flexible panel

The pressure developed beneath a boundary layer on the hard wall is called the blocked pressure. The response of flexible panel excited by the wall pressure fluctuations arising from the boundary layer turbulence depends on both the temporal and spatial characteristics. Turbulence is an intrinsically nonlinear process, which can only be expressed in statistical terms and is generally described by some semi-empirical models.

To quantify the properties of the fluctuation pressure on a planar wall, previous theoretical works focused on understanding how turbulent velocity fluctuations induced wall pressure fluctuations and many experimental efforts were put on obtaining the wave number-frequency spectrum of the wall pressure field. This spectrum represents the distribution of the energy of these pressure fluctuations in frequency and wave number. Mathematically, it is the Fourier transform of the space-time correlation of the wall pressure. Howe (1987) firstly performed a theoretical investigation of the wave number frequency spectrum of wall pressure fluctuations induced by turbulent boundary layer flows of low Mach number. The findings indicated the existence of a spectral peak at wave numbers in the vicinity of the acoustic wave number. This peak was of infinite amplitude for an ideal homogeneous boundary layer on an infinite plane wall, but was finite in practice because properties of the flow generally had little or no impact on the structure of the pressure spectrum at other wave numbers. Howe (1991) also summarized the empirical models of the turbulent boundary layer wall pressure spectrum and radiated sound. A very useful model was proposed by Chase (1980), in which there were several adjustable coefficients and the values were confined in both the convective and low wave number regions. However, this theoretical study was restricted to isentropic boundary layers at low Mach numbers without a mean pressure gradient. And the understanding of the properties of the sub-convective and acoustic domain is still insufficient. Chase (1987) then extrapolated his empirical model related to the acoustical parameters but the result had not been validated experimentally. Chase (1991) also reviewed the properties of the wave vector-frequency spectrum of fluctuating pressure on a smooth planar wall in turbulent boundary layer flow at low Mach number. He pointed out that in the range of low wavenumbers, the amplitude in the spectrum would be expected to depend on the square of the wave number; in a higher sub-convective range, most pertinent experiments showed that the spectrum became wave number-white. Both Howe and Chase asserted that the reliability of the various models had remained controversial and the model was totally invalidated by experiment in the acoustic domain although those formulae representing wall pressure in the flow convective region could probably be used.

Numerous experimental studies of the fully developed turbulent boundary layer and wall pressure spectra were conducted by Karvelis (1975), Bull and Norton (1981), Sherman (1990) and Farabee (1991). Typically, the studies include that the air flows over a surface , called external flow and the air flows flow through a tube/pipe, called internal flow. The measurements were basically similar. Two-point measurements were used to infer the wave number frequency characteristics of the wall pressure from the cross spectrum analysis. Those results were very useful in the theoretical modelling but the variation of the pressure along the wall was still unknown because there was no spatial analysis for the wall pressure. Then arrays of pressure transducers were adopted to obtain wave number spectrum. Direct measurements of turbulent boundary layer wall pressure fluctuations in streamwise direction were conducted by Abraham (1998) in an acoustically quiet water tunnel. The results showed that the highest energy is observed along the convective ridge. Many physical parameters of the boundary layer such as mean wall shear stress, boundary layer thickness, displacement thickness and momentum thickness were derived to normalize with the time and length scales. And the scaling provided an excellent collapse of the spectrum over all resolved wave numbers for the Reynolds number range covered in the experiment ($8100 < Re < 16700$). For the drum-like silencer, an important character of the wall pressure spectra is that both the aerodynamic and acoustic components should be considered at the same time. To quantify and separate these two excited loadings, Auguillat (2005) developed a rotative array method to measure the complete map of cross-power spectral densities over a large area. Through analysis of the spectra, acoustic energy inside the boundary layer was about 5% of the aerodynamic energy. This measurement was also used to find out the surface pressure fluctuations in case of turbulence flow such as the separated and reattaching flows over a forward/backward-facing step or by an unsteady wake (Lee and Sung, 1999, 2001, 2002, Chun, 2004, Hudy, 2003, Camussi, 2008, Josser 1990, Park, 2008). Apart from studying the spectrum of the pressure variation in the external flows, there are some studies on the characteristics of the pressure fluctuation inside the duct which is also to be investigated in the current project. Gerald (1987) investigated the turbulent boundary layer wall pressure fluctuations inside a pipe with fully developed turbulent flow of glycerine by the signal processing method. The non-dimensional spectra measured in that study agreed quite well with those measured under a turbulent boundary layer on a flat plate in air. Lai et al(1992) presented the turbulence wave number spectra were in fully-developed smooth pipe flow for a range of Reynolds number from 6900 to 26800. The most intense waves were characterized by the spectral peaks and found to convect approximately at the local mean fluid velocity. Agarwal (1992) compared the wall pressure fluctuations under the undisturbed flow condition in fully developed turbulent pipe with that under disturbed flow condition due to the existing of an orifice plate. It was revealed that the power spectral density for the wall pressure in undisturbed flow was much higher than that in the disturbed flow. Such huge difference was attributed to propagating acoustic waves generated by the flow disturbance. Additionally, the acoustic component obtained by subtracting the hydrodynamic component from the total wall pressure fluctuations was dominant in the nominally undisturbed flow at the upstream-side of the orifice as well as the reattaching and recovering flow at the downstream-side of the orifice.

Some of the prediction models for the turbulent boundary layer wall pressure were examined by many researchers. Choi (1990) predicted the wall pressure by using numerical simulation of turbulence in the channel. It was shown that the similarity pattern of the pressure spectra for all models can be obtained at high frequencies and high wave numbers. Capone (1995) made a great effort on studying the effects of the transducer spatial averaging. When a comprehensive set of new empirical constants were provided based on the experimental findings, the results exhibited that the Chase model(1987) gave the best method for predicting the turbulent boundary layer wall pressure spectra at convective and sub-convective wave numbers for the low and medium frequency range (below 1000Hz). Lysak (2006) developed a stochastic model based on the Poisson pressure equation to predict the wall pressure inside the pipe. When the parameters such as the turbulent mixing length and Reynolds stress are known, the model could be very accurate to predict the wall pressure over a large range of Reynolds number.

Apart from the wall pressure distribution along the wall of the pipe, another important issue is to see whether there is instability of the flexible structure of the duct wall in the axial flow. Generally, the instability for the flexible panels exposed to fluid flows could be classified into three types. The first type is Tollmien-Schlichting instability (TSI) which is mainly concerned at the early stages of flow transition from laminar to turbulent in the boundary layer. The energy was transferred from mean flow to the perturbation by the enforcement of the wall friction layer. The second type was the travelling wave flutter and the energy was transferred within the gradient of vorticity at the critical layer where the mean flow speed was the same as the wave speed generated by wind (Miles, 1957). The third type is the static divergence and Kelvin-Helmholtz instability which is regarded as class C instabilities (Landahl, 1962). It was observed that the destabilizing effect was determined by the structural damping. In principle, the main causes to the three distinct instabilities were, respectively, fluid viscosity, vorticity gradient and fluid inertia. The flutter could be caused by self-induced structural vibration due to linear disturbances. For the axial flow past the flexible panel, different types of instability on various boundary conditions at the leading and trailing edges will be observed (Guo and Paidoussis, 2000). The understanding of the phenomena for the flow induced vibration on the tensioned flexible wall is still not enough based on the existing literatures. Huang (1997) pointed out that two physical parameters were required to be considered in the wall pressure perturbation. One is the wall displacement and the other is the velocity of the wall motion. The first component was the only one leading to destabilize for potential flow while the second component produced a wave drag and irreversible transfer of energy from the flow to waves. These were considered to be the possible mechanisms for the self-excited oscillation. Afterwards, Huang (2001) studied the coupling between Poiseuille flow and a tensioned membrane of finite length. The results showed that there are crucial effects on the characteristics of the membrane instability at the upstream-side and downstream-side of the channel. Furthermore, the elastic waves over a finite membrane had a standing wave pattern which could be decomposed into up- and downstream-travelling waves. And the downstream travelling wave was responsible for the energy transfer from the fluid to the wall. Stewart *et. al.* (2009) explored the instability of the laminar flow past the flexible wall which is made of a massless membrane under a longitudinal tension at high Reynolds number. Two particular classes of oscillatory instability were considered in his study. One of them is the instability due to the high wall tension at uniform flow condition while the other is the non-uniform flow condition. It was found that the former disturbances could extract energy from the mean flow in a different manner to the latter one that emerged from a non uniform base state. In short, several assumptions such as the velocity profile and the external pressure distribution were often made to execute the numerical analysis. As far as the author's knowledge, the experimental investigation was not seen in precedent work. The current research mainly focuses on the vibration measurement of the membrane under a real flow condition. It is expected to describe the characteristics of the instability and the flutter vibration through a systematic parameter study.

## 1.4 Review of the reduction of fan noise

The aerodynamic noise generated from the fan contains a combination of discrete frequency noises, which are related to the blade passing frequency (BPF), its harmonics, and broadband noise. In general, the basic physical mechanism was put forward by Gutin, who revealed the sound radiation by the rotation of the steady loading in his pioneer study (1936). Later, Lighthill(1952) developed the well known acoustic analogy as the general theory of the aerodynamic sound. And in an extensional work by Ffowcs Williams and Hawkings (1969), their famous equation was widely used for considering the effect of all solid boundaries in arbitrary motion. Concerning the broadband noise, Sharland (1964) pointed out that the possible sound sources arose from the unsteady surface pressure by the separation of the boundary layers at the trailing edges, and random inlet flow turbulence. More recently, the source characteristics of the computer cooling fan were briefly reviewed by Wang (2004), the main mechanism of fan noise consists of five aspects: the tip leakage flow, the non uniform inlet flow condition, turbulent and separated flow condition on a rotor, trailing edge noise and the rotor-stator interaction. Afterwards, Huang (2005) succeeded in quantifying the important noise sources from the inlet flow distortion that was attributed to the incomplete bell mouth and the interaction of rotor blades with the downstream struts.

As for the typical fan operating in the duct or mounted within a cylinder shroud in the ventilation system and aircraft applications, the sound waves inside the duct are confined by the duct walls and the number of propagating duct modes can be diminished. The unsteady fluid loading inside the duct comprises two components. The first one is the thrust force along the duct in the plane wave mode and the second one is the drag force in the circumferential direction which would not propagate below the first cut on frequency of the duct. The importance of the ducted fan is that, however, it is more efficient in producing thrust than a conventional propeller, especially at higher rotational speed by reducing the blade tip losses and directing its thrust towards the back only. Due to the complexity of the mechanism involved in the generation and propagation of fan noise, the problem can be tackled by dividing it into a sound source and a propagation aspect. In the current study, the abatement of sound radiation and propagation at the duct exits is the main concern, which is different from traditional methods. The fan noise is totally modelled as a distributed dipole source, and the effect of non compactness is considered to be very small because of near zero spinning pressure mode of the leading radiation (Huang, 2005). Thus the advantage of such strategy lies in the little requirement of source prediction because it is regarded as an internal one.

Before introducing the current methodology on fan noise control, the major techniques of the fan noise reduction were reviewed herein. Basically, there are two major techniques on reducing the fan noise: passive and active methods. In terms of the passive control, although the acoustical duct liner such as porous sheet or metal foams can be used to increase the acoustic treatment area over the tip of the rotor and absorb the radiated noise, it suffers from inherent limitations, such as size, weight, hygiene problem and harsh environment. Besides, it becomes less effective with increasing engine bypass ratio and a reduction of the nacelle thickness, thus a decrease of the liner depth. The state of the art of reactive techniques that mainly rely on the design experience of the fan may be otherwise another promising replacement. Edmane (2001) reviewed some developments in the low noise fan stage design, for instance, swept and leaned outlet guide vanes, fan flow management and scarfed inlet. Recently, an overview of the major accomplishments from NASA research programs was conducted by Dennis (2007). The findings indicated that the reduction of fan noise could be obtained by delaying the onset of multiple pure tones with forward swept fan, by increasing the phase changes from hub to tip of the unsteady aerodynamic with the swept stators, or by controlling the incidence angle of flow near the rotor and stator with variable area nozzles.

Other than the design consideration of the noise source, some researchers focus on the reduction of sound propagation in the duct. Nijhof (2004) investigated the fan noise reduction by means of circular side-resonators both theoretically and experimentally. Two typical kinds of tube geometries including the prismatic tube and a cylinder air layer were modeled and integrated in the duct to cause an impedance change, and acted as an acoustic mirror reflecting the noise back to the fan. Nevertheless, the performance shares the features of other resonators and can only achieve a narrow band insertion loss of high magnitude when the dimensions and location of the resonator were properly chosen. Moreover, the two and three coupled circular resonators of developed configurations have been validated with experiments.

The active noise control method to abate the sound radiation from the source is similar to traditional active control method in which a given acoustic field is cancelled by a secondary sound source with same amplitude but opposite phase from the reference signal. The array of actuators to produce the cancelling field was used and these array actuators generally composed of an arrangement of microphones (Koopmann et al, 1988, Gerhold, 1997), or resonant type drivers (Walker, 1999) or conventional electromagnetic drivers (Lauchle et al, 1997). Wang and Huang (2005, 2006) investigated the reduction of both drag noise and tonal noise from a small axial flow fan by virtue of active control scheme consecutively. A mini electret microphone was used to measure the rotational acoustic sound field and an ordinary loudspeaker was used as cancelling source. The experimental results showed that the globally integrated sound power was reduced by about 13 dB for the drag noise and by 11dB for the radiated tonal noise, respectively. Nevertheless, one important point in the reported studies is the application of the baffle in the rotational plane of the fan to simplify the acoustic field. Consequently, the acoustic directivity pattern cannot be quantified owing to interference among different components in the global field. The acoustic directivity shows a tilted pattern as a result of the interference among various radiated waves, which means that there is the partial cancellation of sound (Gerard, 2005, Huang and Wang, 2005). Furthermore, the assessment regarding the practical application of the active noise control remains in question due to the stability of the whole system. Some hybrid systems that integrate the acoustic treatment are also explored. Wong (2003) investigated the attenuation effectiveness of the combination of passive and active method. He used thick wool blanket to reduce fan noise and active noise method with the aid of an infra red device as a reference signal source to reduce the low frequency discrete noise with high amplitude. Such combination can produce an overall attenuation of about 6dB of the A weighted sound pressure level.

Although much effort was spent on fan noise reduction, the discussions and understandings lacked of concerning the control of the noise source itself, especially in a broadband frequency range, in literature. Note that the noise source was usually regarded as a monopole, while the fan is more like a dipole in nature, particularly placed in the duct. Huang (2010) proposed a reactive method to control the dipole noise source by using expansion chamber to enclose the dipole source. Two aspects in the noise reduction mechanism in this design are considered: (a) the length and expansion ratio of the expansion chamber and (b) the acoustical interference between the noise radiation and the reflection at the duct junctions due to the impedance mismatch. The results show a desirable performance of an octave over 10 dB insertion loss in the frequency range below the cut on frequency. It is quite effective to control noise radiation from the source at low frequency towards zero frequency. Such kind of configuration with sudden change of cross sectional area will cause the back pressure problem in case of flow. In order to avoid it, membrane is used to line along the inner tube of the chamber segment. In principle, this may share the same features of drum-like silencer but the working principle is different. There are several potential advantages of thin membrane to line along the expansion chamber. (a) Pressure drop can be eliminated in case of flow condition and (b) It is expected that there will be high noise reduction on the broadband frequency noise near the BPF of the fan and its harmonics when the membrane vibration is fully coupled with the acoustical field. Such broadband abatement can be more pragmatic and sustainable even though the fan speed varied.

## 1.5 Outline of the current work

The study involves both theoretical and experimental efforts. The objective of the current study lies in two main aspects. One is to understand the occurrence of vibration instability on the tensioned membrane in case of different flow speeds, and the other is to investigate the application of the expansion chamber with tensioned membrane on the noise source control of the axial flow fan. The background and objectives of the current project including the overview of the relevant works are introduced in Chapter 1.

Direct measurement of the wall pressure fluctuation in the boundary layer of the rigid wall is conducted by using two-microphone with multiple measurement points and the analysis is described in Chapter 2. The characteristic and distribution of both aerodynamic and acoustic loading on the membrane have been evaluated in terms of the wave number frequency spectrum analysis. The response of the flexible panel can be qualified by the pressure field near the surface of the panel. The pressure field can be measured by the electret microphones and analyzed by the correlation and coherence with the panel vibrations.

In Chapter 3, the flow effect on the unstable vibration of the membrane lined along the duct is to be investigated experimentally. The flow behaviour is divided into the axial-flow and cross-flow, separately. Two kinds of new configurations are fabricated for investigating the instability of the tensioned membrane with different flow speeds in the axial-flow and cross-flow respectively. The modal pattern and deformation of the membrane vibration in case of instability are measured by scanning the whole surface with a scanning laser vibrometer. Meanwhile, the critical velocity of the occurrence of instability vibration of the membrane and the affecting physical parameters are to be found through a series of experiments.

The feasibility of the control of the dipole noise source by using an expansion chamber with tensioned membranes is to be studied in Chapter 4. The feature is similar to drum like silencer but the mechanism is different. The performance of such a kind of silencer controlling the noise source is investigated by using the numerical simulation in 2D configurations. The optimization is also performed in order to obtain the maximum noise reduction in a specific frequency range. The insertion loss of 10 dB everywhere over a frequency range more than an octave for an infinite duct can be achieved. In addition, the physics behind is to be explained in detail by using the modal analysis and impedance explanation.

The validation of the performance of the theoretical model with experiment is to be described in Chapter 5. For the accurate prediction, the performance of the silencer with tensioned membrane will be investigated by using finite element method in 3D configuration with a finite rectangular duct and a backed cylindrical cavity. In the experiment, both the loudspeaker and the axial flow fan are modelled as the dipole source, and the acoustic pressure is measured at the open end of the duct. The insertion loss spectrum obtained from the measurement is to be compared with that predicted from the calculations. Conclusions and the main findings in the instability vibration measurement of flow past over the membrane and the dipole noise controlled by the silencer with tensioned membranes are to be summarized in Chapter 6.

# Chapter 2 Measurement of the pressure wave number frequency spectrum on the rigid wall

## 2.1 Introduction

This Chapter describes the wall pressure characteristics on the rigid wall in terms of the wave number frequency spectrum through a series of measurements. The pressure loading on the flexible wall can be qualified based on the pressure spectrum analysis on the rigid wall.

Generally, for flow passing through the duct in any configuration and noise control device, the wall of the duct suffers the combination of the aerodynamic and acoustic loadings. Such loadings may cause the instable vibration of the flexible wall. To clarify the relation between the loadings and the instable features, the phenomenon of the instable vibration occurred in the drum like silencer was summarized in two aspects as below. First, the critical flow velocity of the instability increases with the increment of the tension. The velocity range from 7m/s to 15 m/s and the tension range from 100N to 900N were considered in the previous experiment (Choy, et al 2007). Second, the dynamic response of the membrane is mainly dominant at low frequency range of 100Hz to 200Hz.

For the rigid duct, wall pressure under the different flow velocities is measured experimentally by two-point method. The two components of the pressure loading such as aerodynamic and acoustic loadings beneath the boundary layer are analyzed based on the correlation of the pressure at different measuring points. There are flow convection and sound propagation inside the duct simultaneously and their propagating speeds are quite different. These two different wave speeds can be found out through the time space analysis. The wave number frequency spectrum can be obtained from the Fourier Transform of the time space results. It represents the energy distribution of these pressure fluctuations with respect to the frequency and wave number. From the result of wave number frequency spectrum, two lobes with different slopes will be observed which stand for the flow and the sound parts respectively. Mathematically, the slopes signify the wave speeds in the spectrum. The pressure distributions along the duct are to be studied and the results are expressed in the power spectrum, correlation map. According to the energy distribution over the spectrum in frequency domain and amplitude, the aerodynamic and the acoustical loadings due to the flow can be quantified. The relevance of the peak frequency of the vibrating membrane to the pressure distribution is to be analyzed in order to find out the dominant factor to induce the instability of the membrane vibration.

## 2.2 Experimental setup

The experiment set-up including the test rig, equipments, instrument calibrators and the measuring procedures are to be introduced. The data post-processing and analysis are also to be described.

### 2.2.1 Acoustical wind tunnel and test rig

The experiment is conducted in the specially designed acoustical wind tunnel in which the noise of the fan driving the closed-loop flow is absorbed by the acoustic linings. A schematic diagram of the wind tunnel is shown in Figure 2.1.

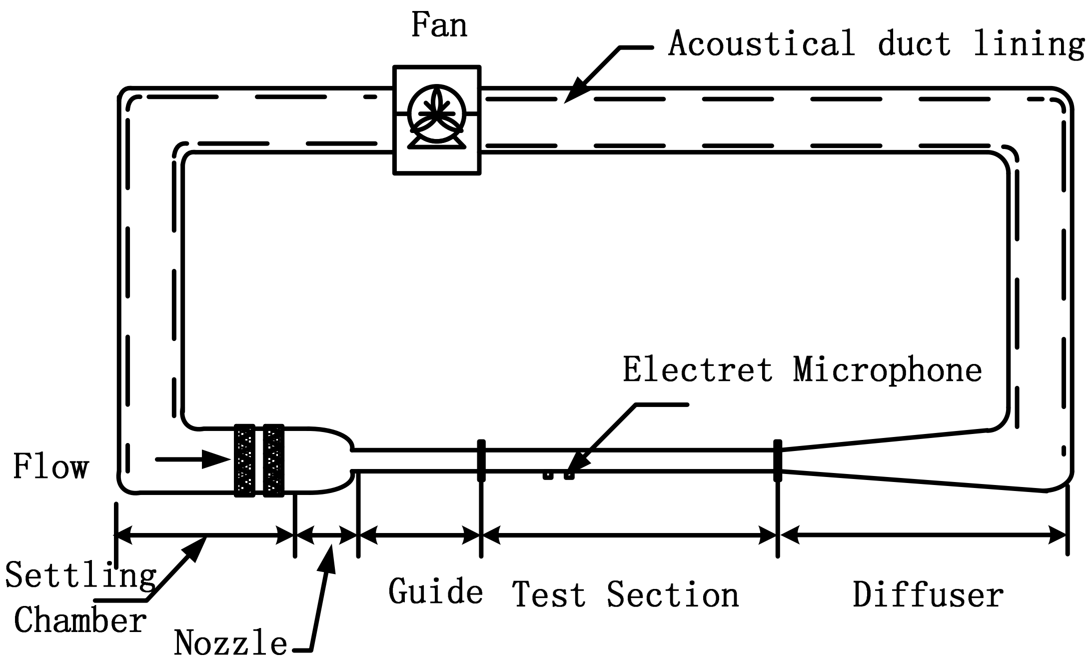


Figure 2.1 Acoustical wind tunnel facility schematic

This acoustic wind tunnel comprised six main sections such as the settling chamber, the nozzle (contraction cone), the guide, the testing section, the diffuser, and the fan housing with a variable speed fan motor. The speed is controlled by a fluid clutch, and the centerline stream wise mean velocity can be varied up to 50m/s. The velocity is measured by the anemometer with the Pitot tube located at the upstream of whole test section. The mini CTA 54N81 and Probe P11 hotwire system from Dantec Dynamics® is also used to measure the fluctuation of the velocity and turbulence intensity.

The test section of the wind tunnel is 100mm by 100mm in cross section and 1.8m in length. To ensure the uniformity of the flow, the turbulence intensity and the flow velocity are checked by traversing the hotwire across the working section with an interval of 5mm. The turbulence intensity is less than 1% on average.

### 2.2.2 Microphone performance

The pressure-type microphone (151-series product from Tibbetts® industries) with a diameter *d* of 2.56mm was used to measure the fluctuating pressure on the surface of the wall. The pressure response at different frequencies is shown in Figure 2.2 and there is no any obvious change of amplitude in the frequency range of 200 Hz to 6000 Hz. For frequencies below 100Hz, although there is roll-off at 3 dB per octave, it is still in an acceptable range.

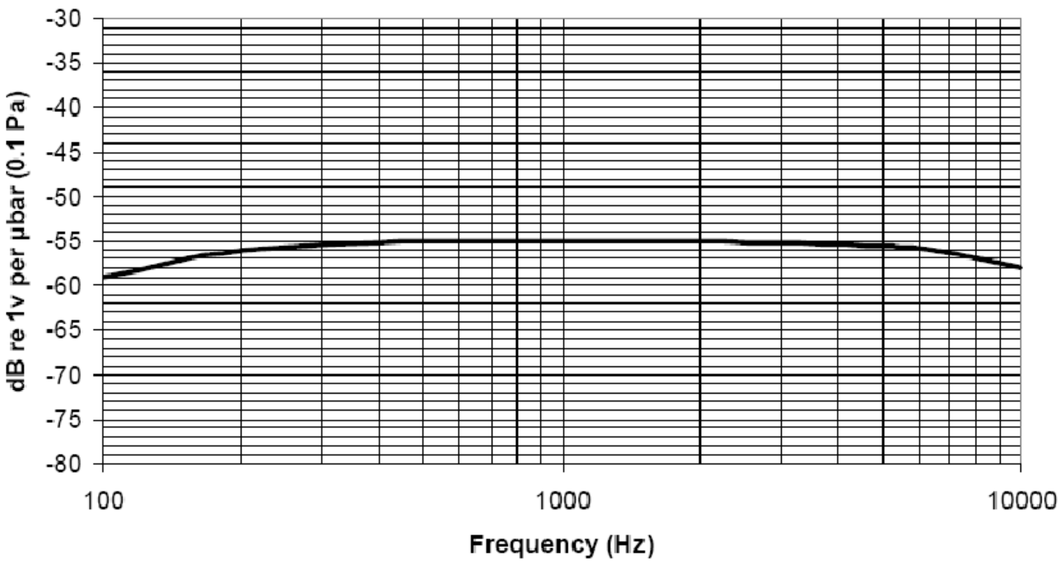


Figure 2.2 Frequency response of 151-Series miniature microphone

With reference to the measuring approach used by Farabee and Geib (1991) and Manoha (1991, 1996), an array sensors were mounted in the center line of the bottom wall of the testing section with spanwise direction to measure the wall pressure distribution. In the current study, two-point measurements with two sensors by moving the positions were adopted because of high price of the good quality of the electret microphones.

Figure 2.3 shows the layout of the measuring position which is similar to that of the array sensors used by Manoha (1991, 1996). In order to increase the spatial resolution, the measuring positions on the bottom of the duct surface are equally spaced in the streamwise direction with an increment, Δx, of 10mm. The total measured length is 500mm, which equals the membrane length and the position of the holes are referred to locations of the membrane in the previous study of (Choy

2005, 2007). The resolved wave number is $-\pi/\Delta x < k < \pi/\Delta x$ ( $\lambda > 2\Delta x$ ) according to the Nyquist–Shannon sampling theorem. Generally, the sensor spacing is always larger than the sensor diameter. To avoid the pressure drop and leakage, all the holes are plugged with a cylinder bar except the two measuring points. Theoretically, the membrane type silencer is investigated in two dimensions. The loading on the membrane is along the streamwise direction. For the characteristics of the wave number frequency spectra in the spanwise direction, it is basically a symmetric distribution with respect to the center in similar tests(J Kim and HJ Sung,2005; Ronald L Panton,1998). And this reveals a two-dimensional structure of wall pressure fluctuations.

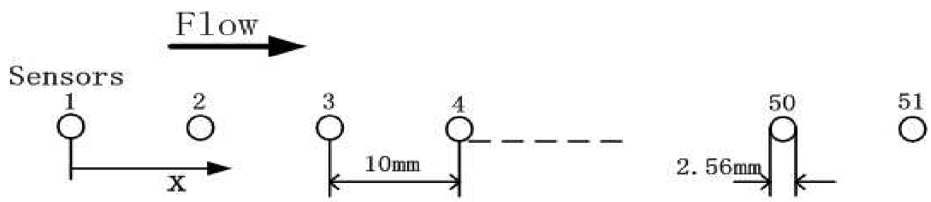


Figure 2.3 Layout of the measuring point position

### 2.2.3 Microphone calibration

Basically, two microphones have different frequency response upon excitation even if they are the same model. The extent of the mismatches in amplitudes and phases will depend on the frequency of excitation. Thus, a correction or calibration is needed for accurate measurement. One calibration method is to put two microphones at the same rigid end of the duct (Sullivan and Crocker, 1978) and the amplitude ratio and phase difference can be obtained. However, the microphone holder used in the experiment should also be considered as well. On the other hand, the calibration can be done by flush mounting two microphones in the wall of the duct (ISO 10534_2:1998, Choy 2003) and swapping their position in order to gain their transfer function. Figure 2.4 displays the set-up for calibration of microphones with the duct which is filled with absorption materials at the end.

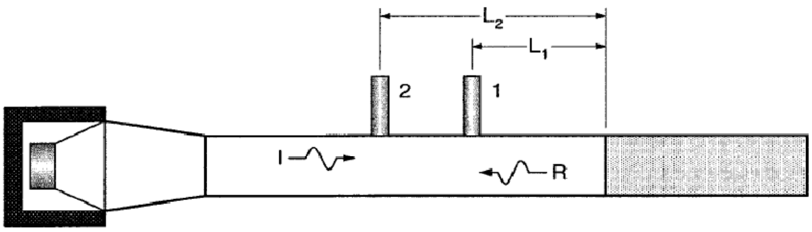


Figure 2.4 Set-up for the calibration of the microphones

For the two electret microphones used in the present experiment with microphone 1 and 2 located at the distance $L_1$ and $L_2$ from the surface of sound absorption material respectively. $J_{21}$ is defined as the transfer function between the microphone 1 and 2, then we will obtain the following relationship:

$$\frac{J_1 A_1}{J_2 A_2{}'} = \frac{J_2 A_2}{J_1 A_1{}'}, \tag{2.1}$$

Finally the $J_{21}$ can be found and can be expressed as

$$J_{21} = |J_{21}| e^{i\theta_{21}} = \frac{J_2}{J_1} = \sqrt{\frac{A_1 A_1'}{A_2 A_2'}}. \tag{2.2}$$

Figure 2.5 shows the amplitude and phase of the calibration factor and a regression curve with polynomial n order of 9. In general, the amplitude ratio curve is very smooth and remains constant above 250Hz. The time lead by microphone 2 over microphone 1 is 10.887 $\mu$s according to the results of phase difference (in radian) and the equivalent sound travelling distance is 3.7361mm, which is about 1.6 percent of 0.2267m wavelength corresponding to the 1500Hz. The value is very small which shows that these two microphones are well matched.

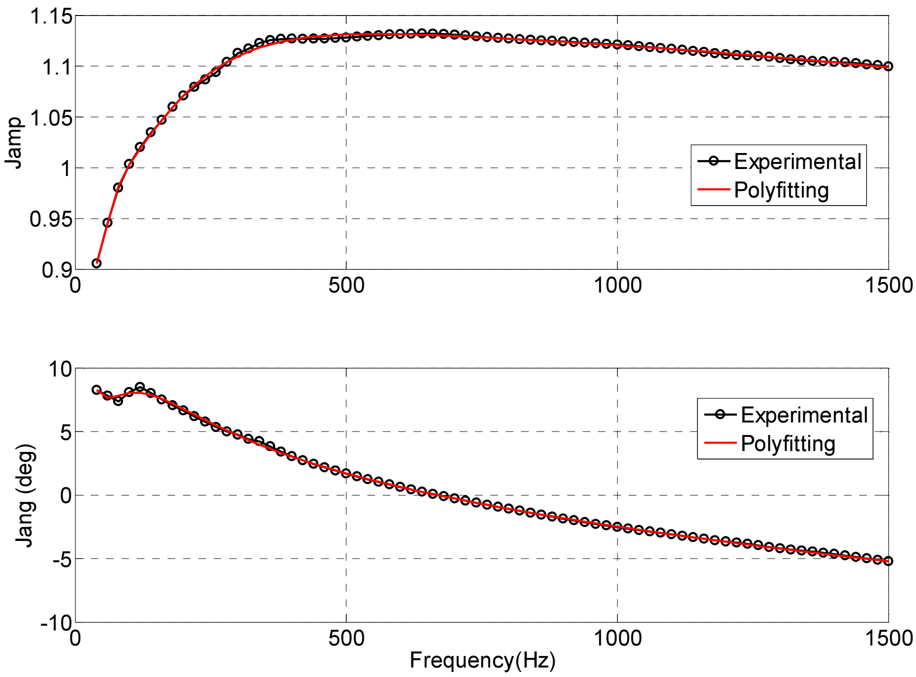


Figure 2.5 Calibration results of the microphones

### 2.2.4 Data acquisition system

Two-point measurements were used in the present experiment. Therefore, we use one microphone kept at the fixed position at point 1 as the reference which is the same in the calibration process. The microphone 2 will be moved to the other holes along the streamwise direction one by one for each measurement. Figure 2.6 shows the flow chart for the whole data acquisition system. The microphones are supported by a B&K's Nexus four channel condition Amplifier (type 2691). To minimize tunnel noise influences and prevent aliasing in the frequency domain, the noise components associated with planar wave propagation through the duct were removed using a low pass filter YE3760 set at Fs/10, which is connected with the preamplifier. The signals are acquired through the National Instrumental conversion card DAQCard-6062E with a sample frequency at 10000Hz for 10 seconds. A MATLAB code is also written for the data acquisition on the terminal laptop.

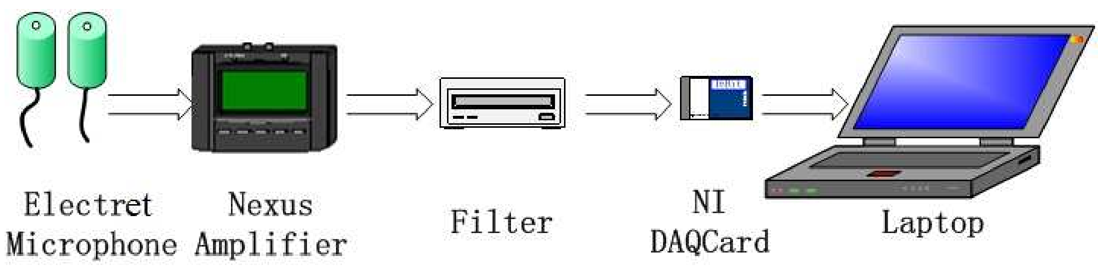


Figure 2.6 Flow chart for the data acquisition system

Before doing the experiment, the electric current noise was checked and evaluated to find whether it will affect the results. Two tests were done. One of them was the no load test which is used to find out noise of the electrical signal and the other was the measurement with harmonic exciting by the fluid loading at the velocity of 10m/s. The results in the spectrum showed that the energy at 50Hz was much lower than other signals at very low voltage, the signal to noise level is higher than 20dBand the influence on the target signal by electrical noise is very small.

### 2.2.5 Post processing

The transformation of the space-time data into the wave number frequency spectra is described in this section. Since the response of the flexible wall excited by fluid loading inside the boundary layer depends on both temporal and spatial characteristics of the pressure fluctuations, cross correlation between those measuring points along the duct to find out the characteristics of the fluid loading is required.

Let $P(x,\mathrm{t})$ be the wall pressure fluctuation where $x$ is the measuring location along the streamwise direction, $t$ is the ergodic time. Then the cross correlation function of pressure fluctuations:

$$R(x,\tau) = < P(x_1,t)P(x_1+x,t+\tau) >, \tag{2.3}$$

where the angle brackets < > denote an ensemble average and $x_1$ is location of the first hole in the coordinate as seen in Figure 2.3. In order to find out the convection velocity, the method of finding the maximum correlation coefficient at each separation point is used (Abraham,1998). According to his method, the correlation coefficient of each point at different time with the respect to the reference point can be plotted in the space time contour map. And the points with maximum correlation for a given separation distance can be located on this contour map. A regression line will also be plotted based on those points with maximum correlation coefficient and hence the slope of this line is used to estimate averaged convection velocity. Note that the slope value can be positive or negative in actual processing, this is determined by the relationship of the measured points with the reference point. In other words, the time can be regarded as delayed or advanced depending on the location of the reference point.

By using the 2D Fourier transform of the space-time data (the cross correlation result), the power density function

$$P(k,\omega)=\frac{1}{(2\pi)^2}\int_{-\infty}^{+\infty}\int_{-\infty}^{+\infty}R(x,\tau)e^{-i(kx-\omega\tau)}dxd\tau \ , \qquad (2.4)$$

where $k$ is the wave number and $\omega$ is the radian frequency. However, in practice, it is impossible to obtain the measurement for the infinite distance and time. Hence, the actual computation of power density function will be expressed as

$$P(k,\omega)=\frac{1}{(2\pi)^2}\sum\sum R(x,\tau)e^{-i(kx-\omega\tau)}\Delta x\Delta\tau \quad . \tag{2.5}$$

Additionally, one may note that the cross correlation can also be obtained by the inverse Fourier transform of $P(k,\omega)$. In the wave-number frequency spectrum, the Fourier amplitude coefficients are displayed to represent the space time field by a sum of waves with frequency and wave number. In the real experiment, the energy distribution at different frequencies can be observed and the relationship of the maximum amplitudes at those frequencies is usually estimated by linear regression. The convective velocity can be calculated with the slope fitting and the characteristic wavelength at a particular wave-number is calculated as $\lambda = 2\pi / k$ based on the travelling wave analogy. In order to validate the implementation of the post processing, the analysis is to be done by measuring wall pressure along the duct wall with the harmonic sound wave excitation. As shown in Figure 2.7, for the harmonic wave excitation at 300Hz, the highest energy level (maximum amplitude) appears at the coordinate *f*=300Hz and the corresponding $k/2\pi$ = 0.84 $m^{-1}$, which is very close to the theoretical value $k/2\pi$ =0.87 $m^{-1}$ when the travelling wave is at the speed of sound. Therefore, the current method is capable for post-processing the real experimental data correctly.

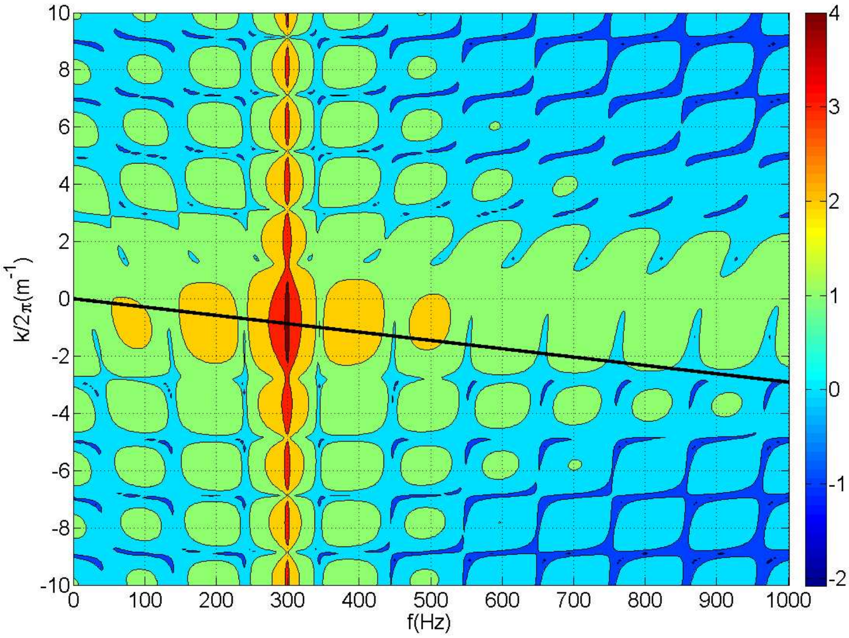


Figure 2.7 Wave number frequency spectrum benchmark for the harmonic wave

## 2.3 Results and discussions

### 2.3.1 Auto power spectrum

The auto power spectra for each measurement point were examined in order to characterise the energy distribution of the wall pressure and to identify the frequency peaks where most energy was centralized. Before this, a curve smoothing method with 5 point average is used to pre-process the data. The five point average method is used to smooth the curve and minimize the noise level before the data processing because there is fluctuation of the measured data. The method is to average the values of five close points with certain weighting function(Sun,2007). To do the analysis from the spectrum more accurately, a Welch method of averaged periodogram Fourier transform was often used (Welch, 1967; Oppenheim and Schafer, 1975). Meanwhile, Burg (1967) developed the maximum entropy spectral analysis technique to improve the frequency resolution. For the analysis of the auto power spectrum in the current project, Welch method and Burg method as well as the direct calculation for the averaged periodogram were used. The results show similar patterns, but for clear illustration only one result is displayed below.

Figures 2.8 shows the auto power spectrum at every fifth microphone location for different flow speeds which are in the range of the vibration instability of the membrane investigated by Choy (2007). For the occurrence of membrane vibration, there is the linear growth of vibration response when the flow speed is lower than 9m/s or that is higher than 30m/s under their corresponding tension. Generally, the spectrum curves typically have a broadband character in frequency with a collapse slope with the increment of frequency. As the flow velocity increases, both the magnitude and the bandwidth of the pressure fluctuations increase. This is consistent with the measured results of Willmarth and Wooldridge (1962), Bradshaw (1967). For the auto-spectrum at low flow speeds in Figures 2.8(a) to 2.8(b), there is a peak of about 60Hz at all the measured locations along the streamwise direction. When the flow speed increases to 27.5m/s, the second peak which is at about 180Hz can be observed as shown in Figures 2.8(c) to 2.8(e). The amplitude of the peak at the

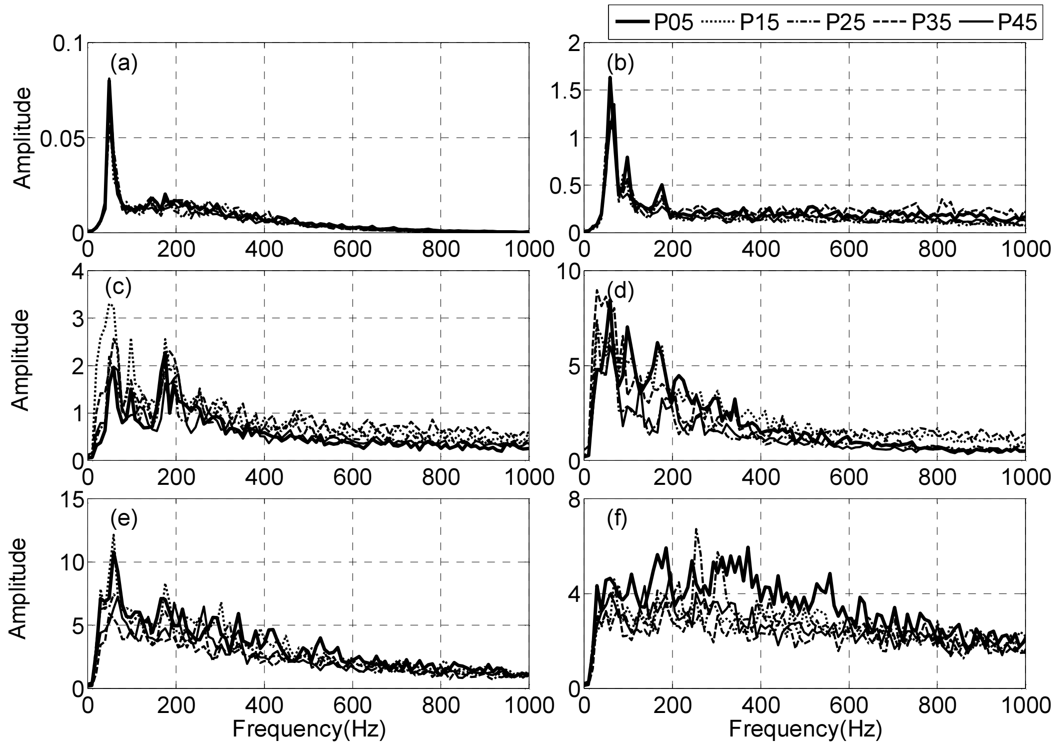


Figure 2.8 Auto power spectrum of the wall pressure at different longitudinal locations for various upstream flow speeds (a) $U_\infty$=6.5m/s (b) $U_\infty$=14m/s (c) $U_\infty$=21m/s (d) $U_\infty$=27.5m/s (e) $U_\infty$=35m/s (f) $U_\infty$=41m/s

upstream location is higher than that at the downstream locations at high frequencies. Similarly, as the flow speed increases to 41m/s as shown in Figures 2.8(f), although a lot of peaks at different frequencies can be observed because of the turbulent intensity and background noise coming from the high flow energy, the peak at 60Hz can be generally considered to be dominant in the whole spectra along the stream wise centre line under moderate high flow speeds. In addition, the energy at the higher frequencies also becomes relatively very low at any measuring locations from upstream to downstream. Such small amplitude at high frequency is attributed to the high amount of energy dissipation at the high frequency for both the acoustical and aerodynamic loading. Nevertheless, these two loadings cannot be separated in this preliminary analysis.

### 2.3.2 Cross correlation analysis

To globally observe the air flow pattern in the stream wise direction, the cross-correlation coefficients obtained from all the measured positions with the first microphone were calculated with a 0.2s delay.

Figures 2.9 to 2.14 show the colour-scale contour maps of the cross-correlation coefficient of the signals against both the stream wise location and the delay time. It is evident from this plot that the high cross correlation region lies in two ridges or lobes: one inclined ridge or lobe at positive angles and the other horizontal lobe. The locus of the peaks along the lobes represents the time delay at which the cross correlation is a maximum for different stream wise direction locations. Furthermore, the peak correlation at each measuring location with respect to the first point can be found by using the time delay signal recorded with delay time $\tau$ . This delay time $\tau$ stands for the average time needed for the air flow passing over the structure and from upstream to farther downstream. Therefore, when the slopes of the lobes have been found, the average convective velocity of the dominant flow structure can be deduced.

Concerning the features of air flow, convective velocity is a very important indicator to characterize the translational speed of fluid within the boundary layer. A commonly used definition of the convective velocity is the ratio of the stream wise separation to the temporal separation which will maximize the cross correlation coefficient. Typically, the ratio is about 0.5 to 0.8 $U_\infty$ in both experiment and numerical simulations in the literature (Chase, 1980; Choi, 1990), depending on the upstream flow disturbance condition, model geometry, location of measurement and measuring technique.

The presence of horizontal lobe in the Figure 2.9 to Figure 2.14 might be attributed to the acoustic mode, which attains a near zero time delay because of the high speed compared with the short measured length. The correlation coefficient of the acoustic mode becomes lower and lower as the flow speed increases and that of the aerodynamic loading becomes more and more dominant. Similar trend can be found in the wave number frequency spectrum below.

Another feature in the contour map is that the negative cross correlation coefficient ridge is also observed in the vicinity of the positive cross correlation peak. Theoretically, both negative and positive coefficient peaks can be used to estimate the slopes and the convective velocity. Those slopes to predict the flow convective velocity in all the contour maps were found by plotting the positive peak locus of the lobes with a linear regression line. Table 2.1 lists the result of the slopes of the regression line at the different measured flow velocities. The strong convective nature of the pressure field gives a convective velocity of about 0.77 $U_\infty$ to 0.82 $U_\infty$ which is very close to the typical value in the previous studies (Bull,1996; Leclercq,2002).

For the acoustic ridges, although the slopes can be predicted for the decomposition of sound wave speed and the flow speed, there is no obvious change on the result since the sound speed is much higher than the flow speed. And at the near zero time, the slope predicted based on the linear regression line is not accurate.

**Table 2.1 Result of the flow convective velocities**

| | | | | | | |
|---|---|---|---|---|---|---|
| $U_\infty$ (m/s) | 6.5 | 14 | 21 | 27.5 | 35 | 41 |
| $U_C$ (m/s) | 5 | 11.5 | 16.5 | 22.5 | 27 | 33 |
| $U_C / U_\infty$ | 0.7692 | 0.8214 | 0.7857 | 0.8182 | 0.7714 | 0.8049 |

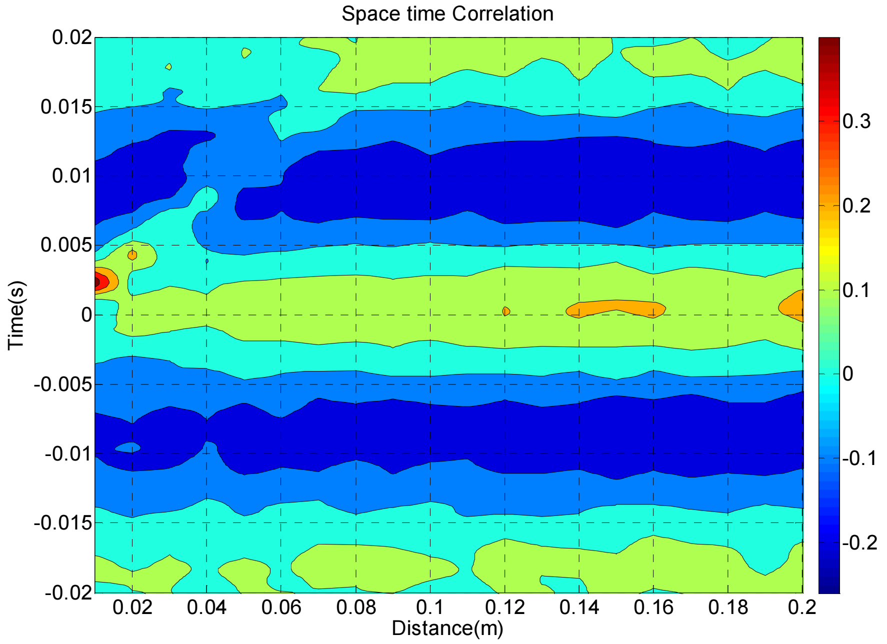


Figure 2.9 Cross correlation coefficient colour contour map( $U_\infty$=6.5m/s)

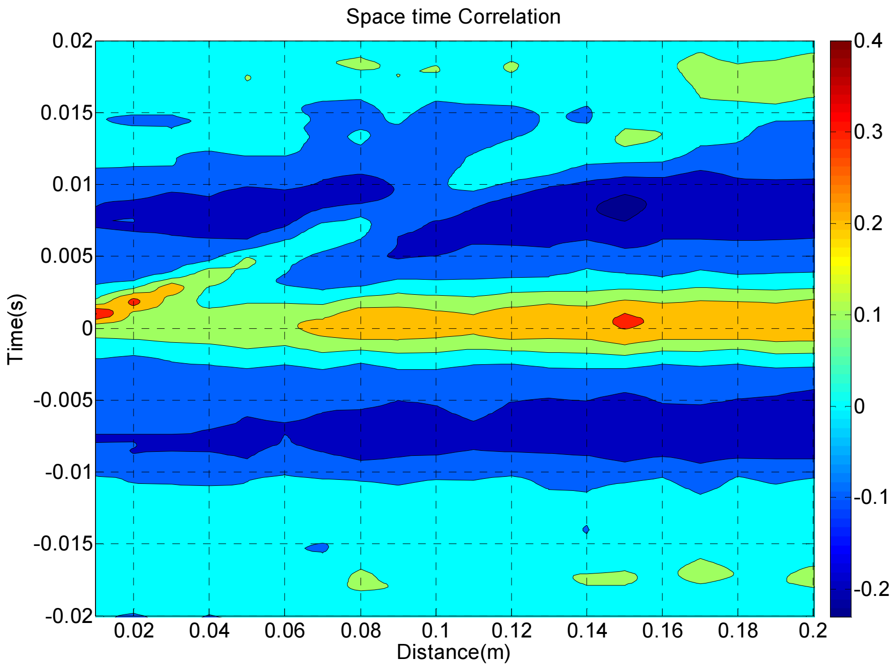


Figure 2.10 Cross correlation coefficient colour contour map( $U_\infty$=14m/s)

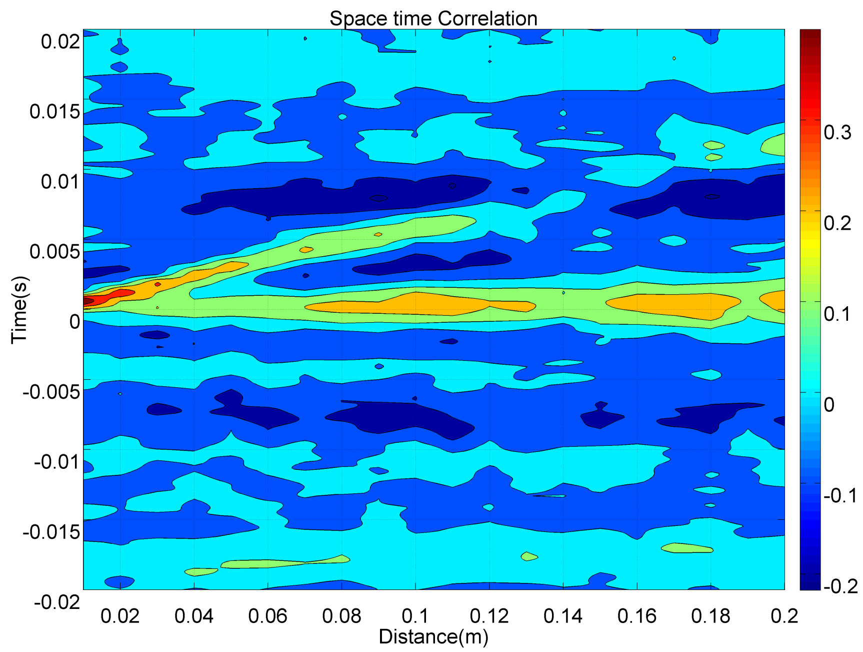


Figure 2.11 Cross correlation coefficient colour contour map( $U_\infty$ =21m/s)

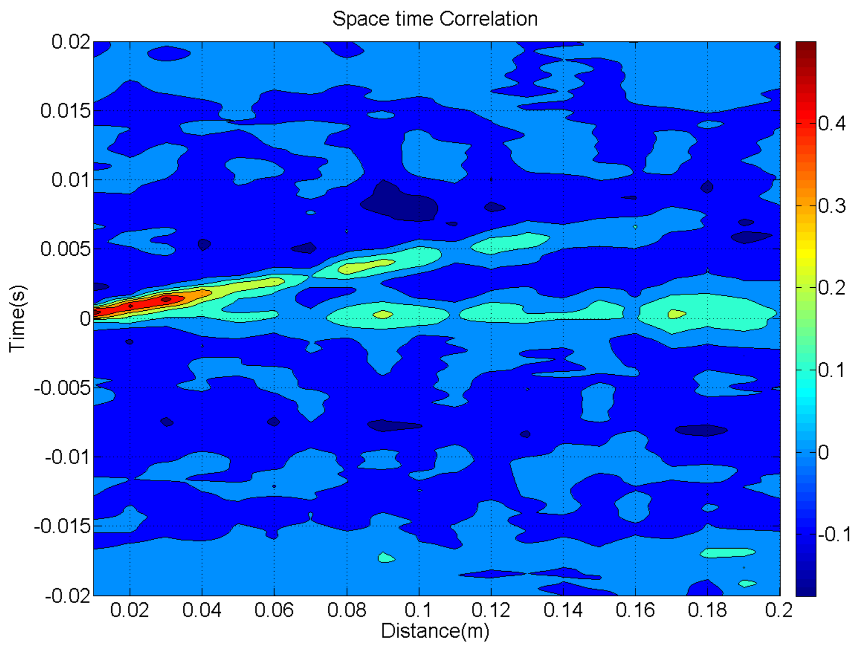


Figure 2.12 Cross correlation coefficient colour contour map( $U_\infty$ =27.5m/s)

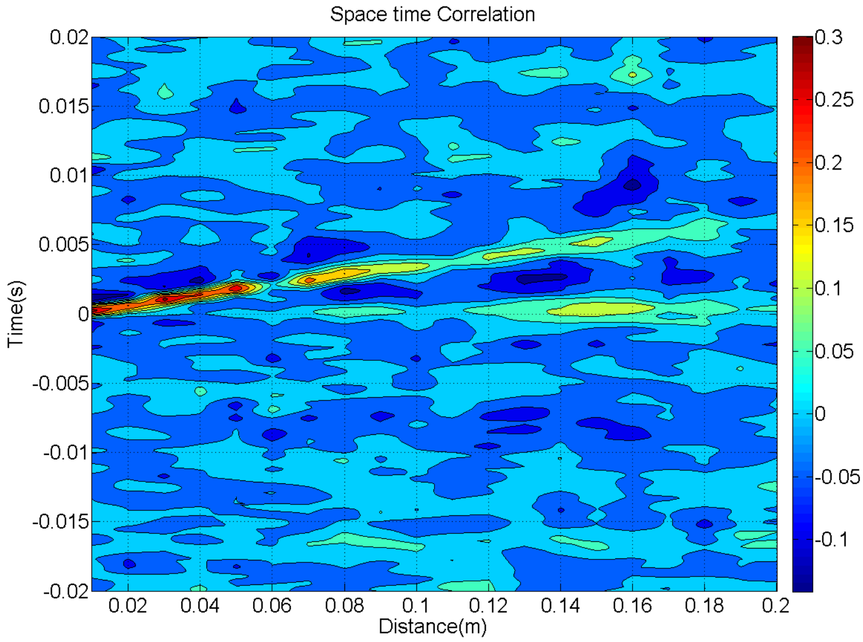


Figure 2.13 Cross correlation coefficient colour contour map( $U_\infty$=35m/s)

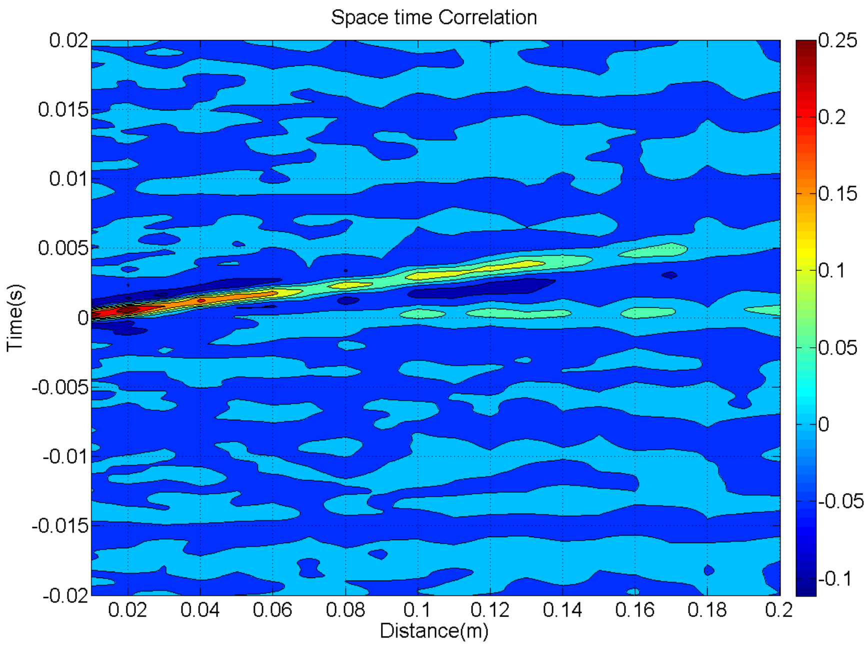


Figure 2.14 Cross correlation coefficient colour contour map( $U_\infty$=41m/s)

### 2.3.3 Wall pressure coherence

The effectiveness of the Corcos exponential decay model is to be taken to examine the coherence for the measuring points. In this model, the loss of coherence between two separated points is expected to be equal to the loss of the coherence in the stream wise direction multiplied by the loss of the coherence in the span wise direction.

$$\Gamma(\xi_1, \xi_2, \omega) = e^{(-\alpha_1\omega\left|\frac{\xi_1}{Uc}\right|)} e^{(-\alpha_2\omega\left|\frac{\xi_2}{Uc}\right|)}, \qquad (2.6)$$

where $\alpha_1$ and $\alpha_2$ denote the empirically determined decay constants in streamwise and spanwise direction, respectively. In the experiment of the current project, however, the model can be simplified in the application of stream wise direction only. One of the air flow condition that is flow speed at 27.5m/s is to be examined.

The coherences in the stream wise as a function of frequency are plotted in Figure 2.15. The coherence decreases exponentially with both increasing frequency and distance for frequency above a certain threshold value. On the other hand, below this threshold, the coherence is stronger with increasing frequency. One important observation is that the threshold frequency decreases when the distance increases. The observation is consistent with the findings in the references (Lee, 2001;

Farabee, 1991). At high frequencies, the turbulent structures generating high frequency pressure fluctuations are rapidly destroyed as they are convected to the downstream. On the contrary, at low frequencies size of the turbulence structures are large and the movement is very slow. The large turbulence structures can probably be destructed by the shear stress beneath the boundary layer, therefore a tradeoff symbolized as the maximum coherence at certain frequency can be observed in the figure. The coherence as a function of separated distance at fixed frequencies is shown in Figure 2.16. The results show that the wall pressure at two measuring points becomes uncorrelated and Corcos model gives a reference of the collapse behavior with $\alpha_1 = 0.2$ for a coherence level of 0.1.

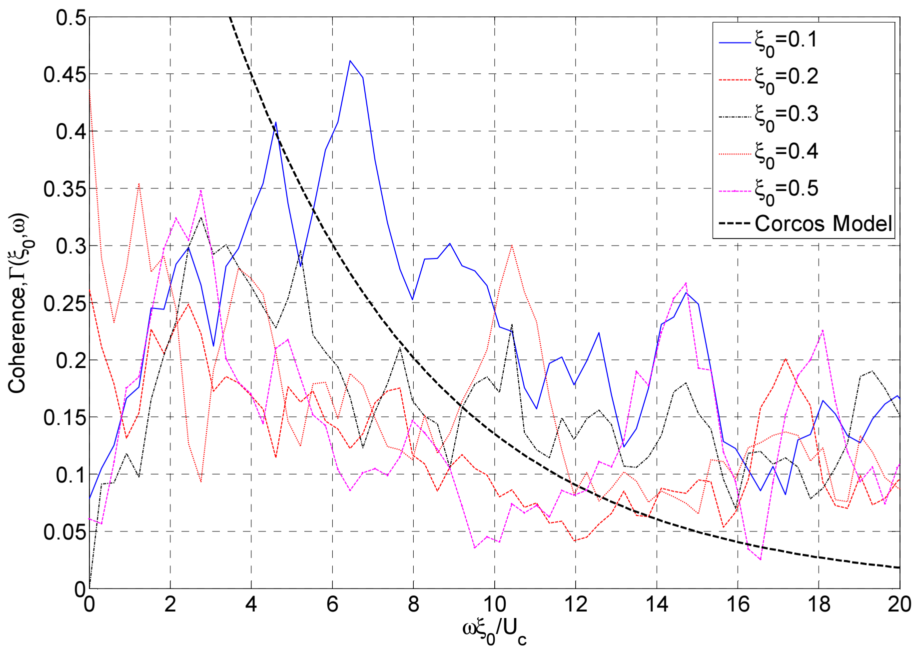


Figure 2.15 Streamwise coherence measured between two points

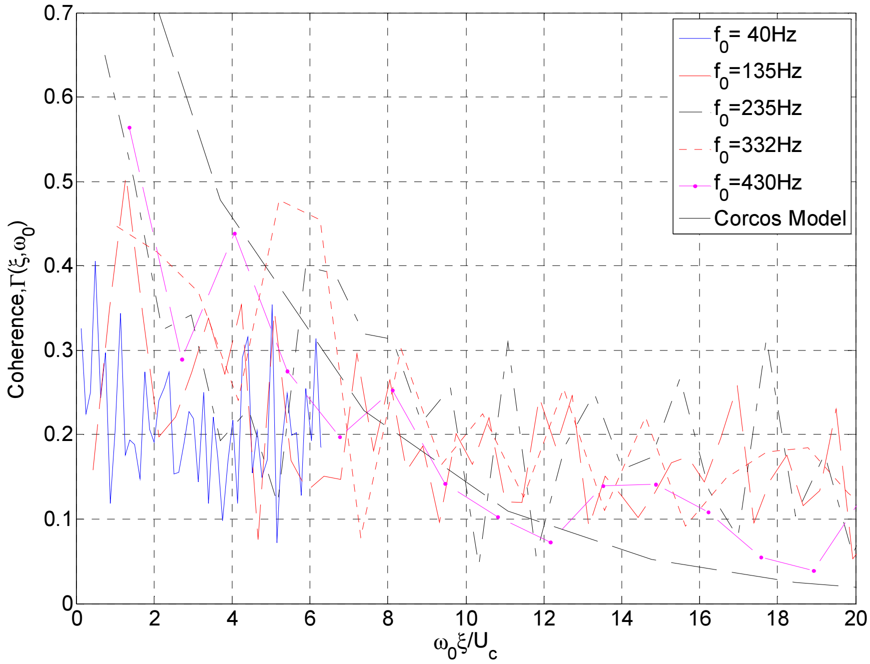


Figure 2.16 Streamwise coherence versus distance

### 2.3.4 Wave number frequency spectrum

To further understand the air flow characteristics beneath the turbulent boundary layer, we now consider the wall pressure fluctuations in terms of the wave number frequency spectra, which will be examined as shown in Figures 2.17 to 2.22. Data below 20Hz are filtered out because of the limitation of the response of microphone.

Several noticeable features can be found from the figures. The acoustic noise is limited to a wave number band near zero as the horizontal ridge. There are two

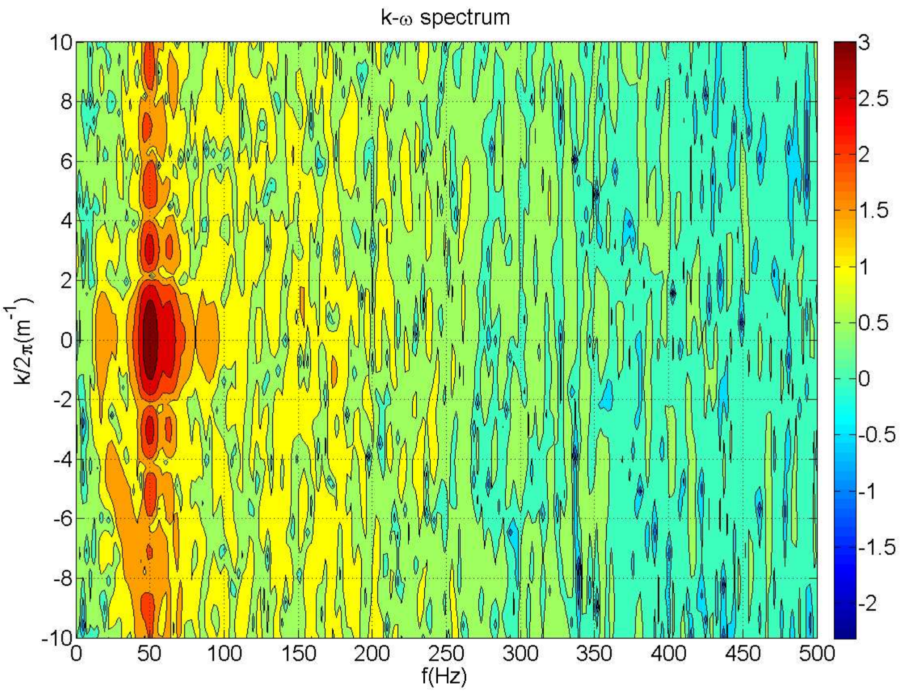


Figure 2.17 Measured wave number frequency spectrum at $U_\infty$=6.5m/s

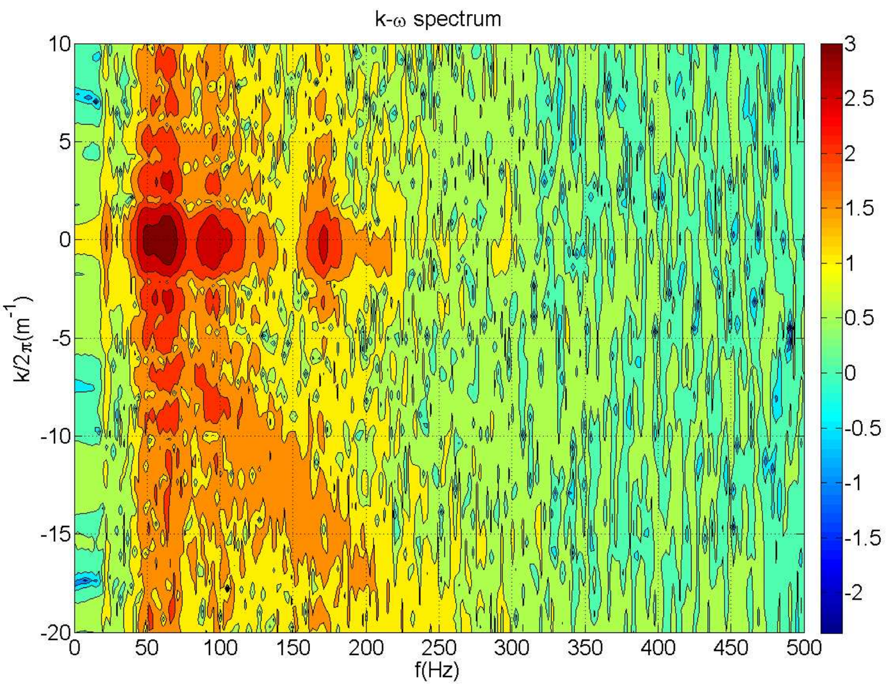


Figure 2.18 Measured wave number frequency spectrum at $U_\infty$=14m/s

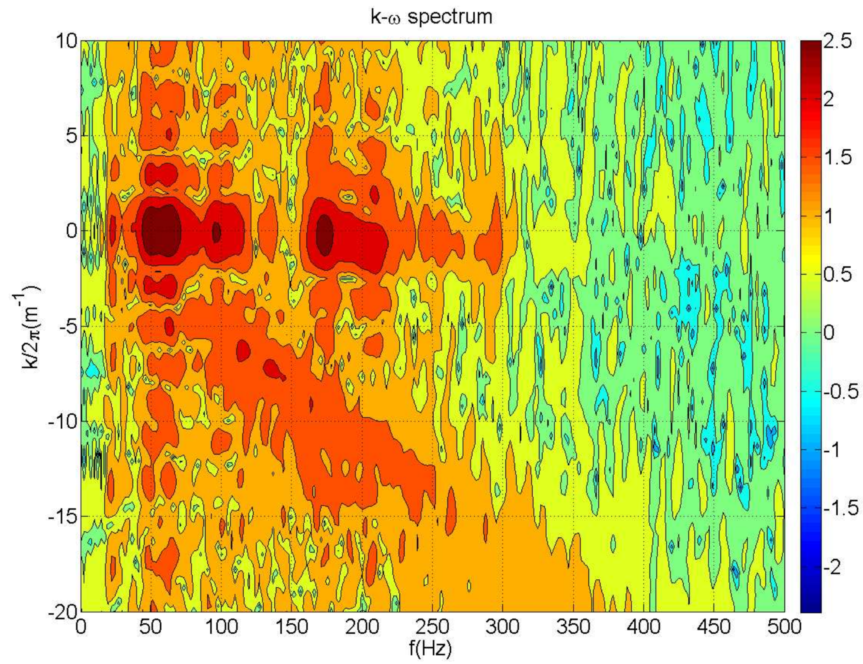


Figure 2.19 Measured wave number frequency spectrum at $U_{\infty}$=21m/s

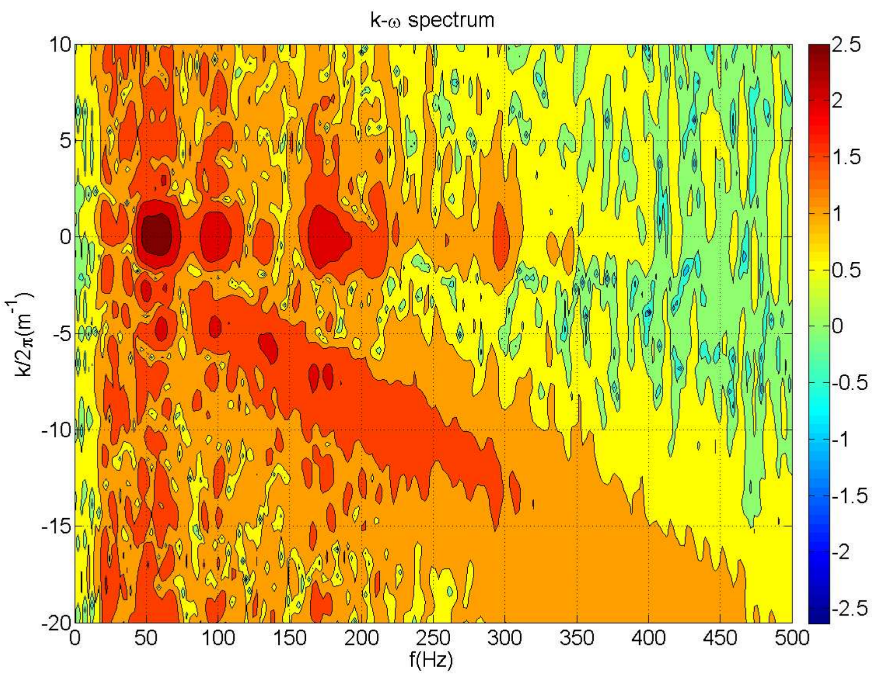


Figure 2.20 Measured wave number frequency spectrum at $U_{\infty}$=27.5m/s

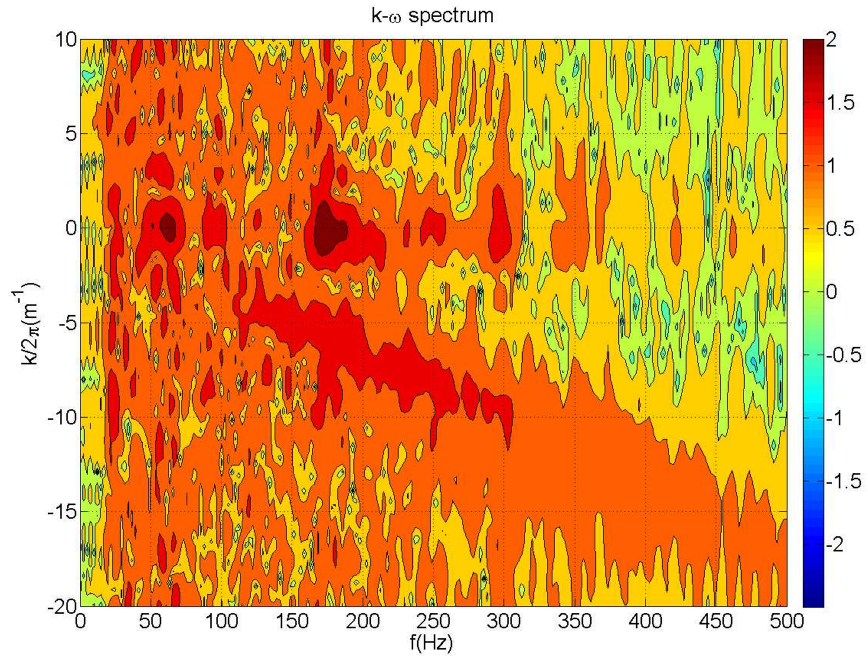


Figure 2.21 Measured wave number frequency spectrum at $U_\infty$=35m/s

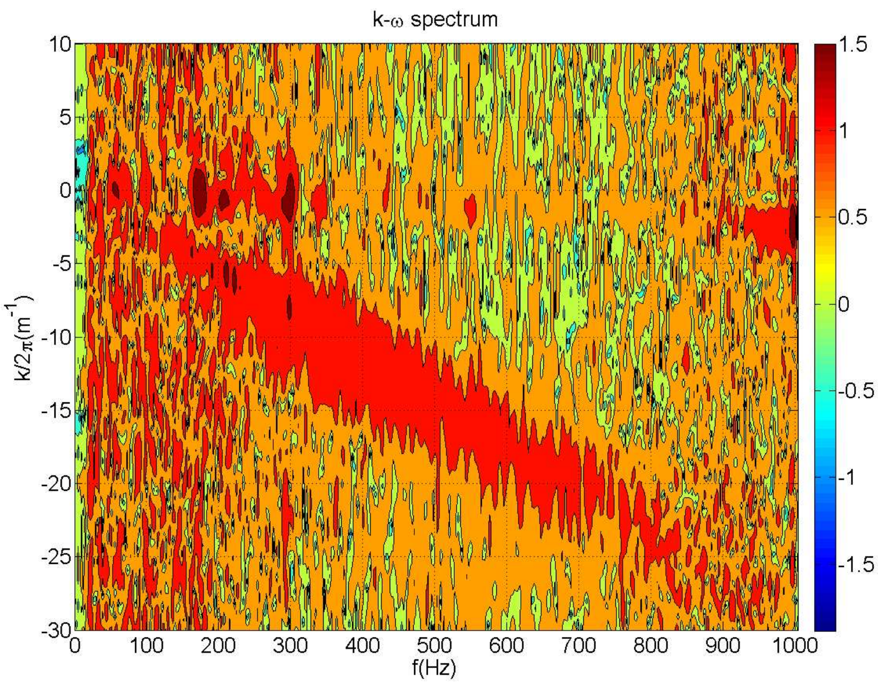


Figure 2.22 Measured wave number frequency spectrum at $U_\infty$=41m/s

peaks with highest energy level along this ridge. The peaks are located at 60Hz and 175Hz, respectively. At the near zero time delay, the corresponding ridges can also be found and the corresponding frequency band is between 110 to 160Hz at all the velocities. For this frequency range, there is no acoustic loading.

The wave number spectrum reaches a local maximum at a particular frequency and disperses in all wave numbers, which is in agreement with previous studies (Lee, 2001). This frequency is identical to the acoustic peak frequency as mentioned in the first feature. As the flow speed increases, the peak frequency has been shifted from 60Hz towards 175Hz, which means low frequency noise becomes less and less dominant.

The flow convective ridge is more and more obvious with the increment of the flow speed except at the lowest speed. This may be attributed to the low energy contribution from the flow convection such that it is difficult to discern at the very low speed. According to the correlation map which shows the slopes of the ridges and the convective velocity, the decreasing slope indicates increasing velocity. Besides, most of the energy along the ridge will shift to high frequency at the high flow speed. This means that there is less energy at the low frequency range below 100Hz at very low flow speed, so we can conclude that the effect of flow on this frequency range is significant only at medium flow speed.

### 2.3.5 The analysis on the phase and convective components

In order to determine the convection velocities associated with individual frequencies, phase angle in the stream wise development was investigated at arbitrarily selected flow velocity. From cross spectrum $\varphi(\xi,\ \omega)$ shown in Figures 2.17 to 2.22, the convective velocity $U_c$ can be found as $U_c$=-$\frac{2\pi f\xi}{\varphi(\xi,\omega)}$, where $\frac{\varphi(\xi,\ \omega)}{\xi}$ can be obtained from linear regression line. Figure 2.23 and Figure 2.24 show the phase angle as a function of the stream wise location for 120 Hz and 50Hz respectively at the flow velocity of 27.5 m/s. These two frequencies were chosen because the maximum and minimum of the correlation are observed in the wave number frequency spectrum. The convective velocities can be deduced from the linear fitting slopes, the result shows that the velocities for the frequencies of 50Hz and 120Hz are listed in Table 2.2. It is found that the air flow convective velocity is 22.5m/s while the acoustic convective velocity is 349m/s. Figure 2.24 shows the phase angle oscillations with the distance. This is due to the existence of standing waves formed from the combination of reflection waves at the downstream of the wind tunnel, the wave speed deduced is not very accurate according to the present method. It can be regarded as the reference value.

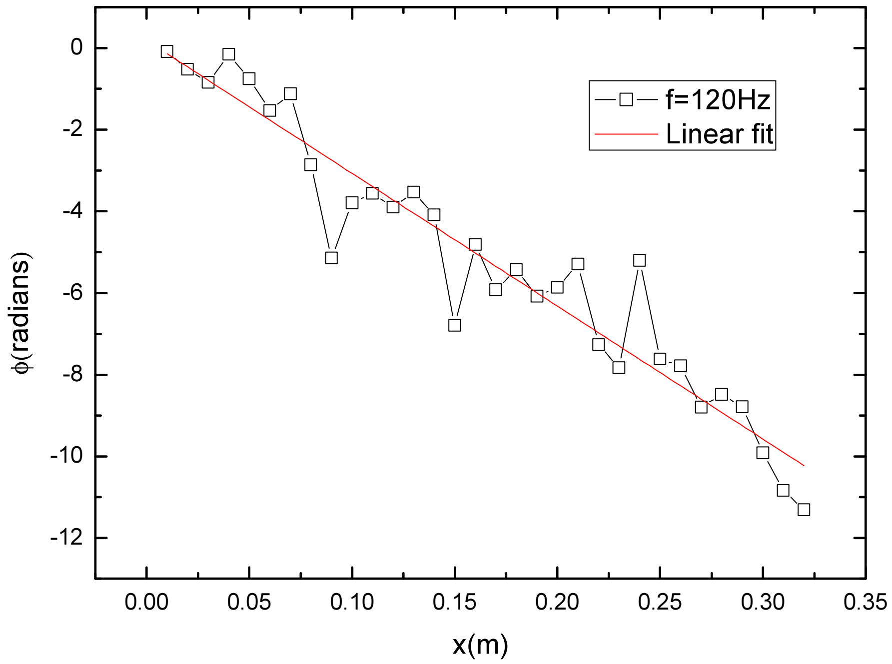


Figure 2.23 Phase angle against the distance for f=120Hz and $U_\infty$=27.5m/s

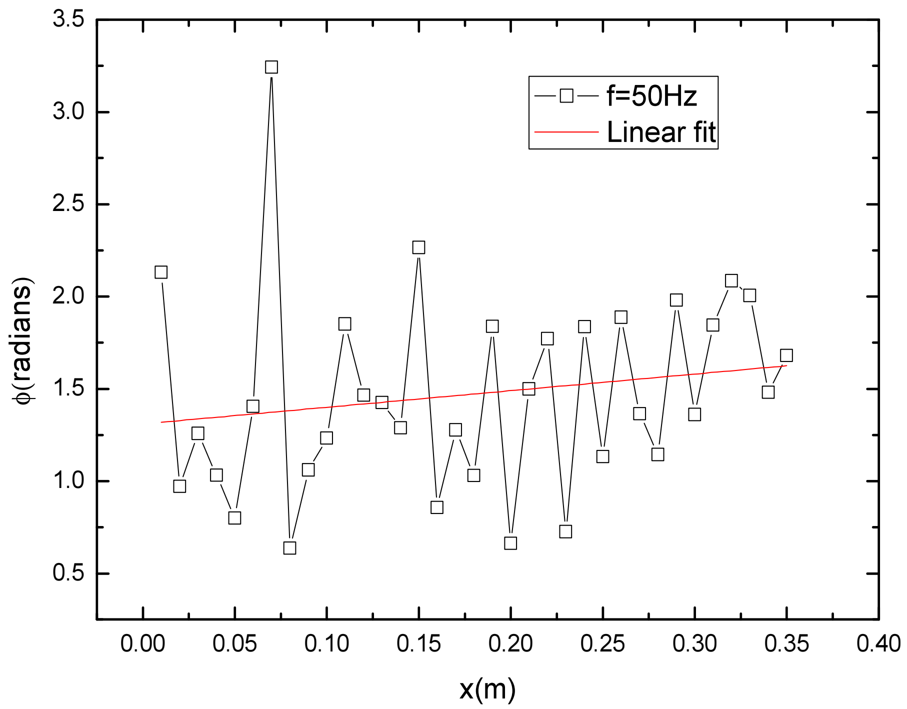


Figure 2.24 Phase angle against distance for f=50Hz and $U_\infty$=27.5m/s

**Table 2.2 Convective velocities for two frequencies**

| Frequency(Hz) | Convective velocity(m/s) |
|---|---|
| 120 | 22.5 |
| 50 | 349 |

## 2.4. Conclusions

Direct measurements of the wave number frequency spectrum of the wall pressure fluctuation in a rigid duct were conducted to evaluate the distribution characteristics of both aerodynamic and acoustic loadings with the Reynolds number from $4\times10^4$ to $2.8\times10^5$ based on the height of the test section (equivalent diameter) in the closed-circuit wind tunnel. Several conclusions can be drawn from the primary measurements:

(1) Generally, the acoustic energy overweighs the aerodynamic energy at frequency range lower than 60Hz, while the aerodynamic pressure dominates at higher frequencies.

(2) The acoustic pressure is dominant when the air flow velocity is low while aerodynamic pressure becomes dominant at high Reynolds number. As the Reynolds number increases, the frequency range at which the power of the fluid loading is

very high and shifts from low frequency to high frequency.

(3) The acoustic loading is not significant in the frequency range of 110Hz to 160Hz. Convective velocity or the phase can be computed by cross-spectrum and the condition for such computation is that there are expected to be about 80% of the free-stream velocity.

(4) When referring to the dominant vibrating frequency range of 100 Hz to 200Hz , the response of the membrane is determined by the aerodynamic fluid loading rather than the acoustic loading because of the acoustic limited frequency Besides, the relative influence of acoustic loading and aerodynamic loading is estimated by comparing the amplitude of the correlation. The result also indicated that in the frequency range of 120Hz to 170Hz, the correlation of the acoustic loading is basically less than 50% of that of the aerodynamic loading. Thus, the instable vibration can be attributed to the aerodynamic loading.

# Chapter 3 Vibration measurement on the instability of flow past a tensioned membrane

## 3.1 Introduction

Based on the findings in Chapter 2, the flow effect is significantly important in controlling stability of the vibration on the innovative tensioned membrane silencer such as drum-like silencer, which consists of a tensioned membrane backed by a cavity and thereby achieves a broadband noise reduction in the air ventilation system (Huang in 2002). The duct silencer with moderate flow condition to simulate the realistic situation is to be explored in this chapter. Choy (2007) reported that there is flow-induced vibration when the flow speed increases. The exponential growth of vibration and flutter were observed. The occurrence of the instability of the membrane vibration inside the drum like silencer with different aerodynamic conditions is to be investigated in detail in this chapter. The characteristics of the flow-induced vibration are also to be studied.

For the design of drum silencer, in order to simulate the two-dimensional configuration from the three dimensional model and allow for the free vibration at the edges, there is small gap membrane edges and duct walls as shown in Figure 3.1(a). The sound leakage in this deliberate design has been proved to be very small. However, there is flow leakage through this gap which may induce the instability vibration of the membrane. Thus, there exist the multi-flow loadings on the membrane. Besides, with the cavity covered by the membrane, critical velocity which is defined as the starting velocity of the air flow for the occurrence of instability of the membrane vibration has been shifted because of the acoustic loading change on the membrane when the cavity is added.

To elaborate the complication of multi-flow effects, the characteristics of air passing over the membrane will ultimately be divided into two typical aspects. The first kind of flow condition is the so called parallel flow which means that main air flow is in axial direction and parallel to the gap shown as Figure 3.1(b). The second condition is the so called cross flow which means that the air can leak through the gap perpendicularly to the main flow direction as shown in Figure 3.1(c). For preventing the sound leakage, the width of the membrane is wider than the height of the duct and this will cause the air flow leakage through the gap between the lateral edges of the membrane and the duct wall as displayed in Figure 3.1(c). This is a crucial point to induce the instable vibration.

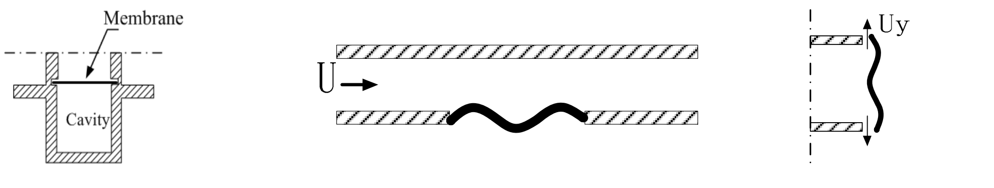


(a) Cross section (b) Parallel-flow (c) Cross-flow

Figure 3.1 Two conditions of the flow effect on the drum like silencer

These two typical phenomena can be commonly seen in the industrial applications in the manufacturing processes of thin materials such as paper and photographic film. During the operation, the membrane is under tension in one direction and transported over rollers and guides. In addition, the air flow is parallel to lateral free edges. For the current study, the membrane is flush mounted on the duct wall. One side of the membrane surfaces will be excited by the combination of the aerodynamic and acoustic loading when air passes over it while the other side will have no air passing by. Concerning the study of the instability vibration of the membrane inside the different configuration of the duct, few authors have hitherto investigated the instability phenomenon of a tensioned membrane in the flow direction as a flexible wall. Huang (2001) studied the effect of the Poiseuille flow passing over a tensioned membrane of finite length by using an *eigen*-value approach and analysis. The boundary condition at both upstream and downstream of the duct was found to be very crucial on the instability characteristics. Stewart et. al. (2009) developed a one-dimensional model of flow in a long flexible walled channel with the consideration of an integral approximation of the unsteady boundary layer equations. However, the Reynolds number is assumed to be small that means the laminar flow condition is considered in both simulations. Besides, there is still no experimental validation for those numerical results. Apart from this, turbulence flow is commonly seen in the realistic situation instead of laminar flow condition.

A large number of studies have been conducted into the flow-induced vibration vibrations especially for the case of fluttering due to the cross-flow on the stationary tensioned paper. Y B Chang (1992) devoted much effort to this topic with the considerations both analytically and experimentally. The cross-flow on the membrane is very similar to the flag flutter except for the existence of the in-plane tension. The major difference between the previous literatures and existing project lies in the boundary conditions of the four edges. Previous models frequently emphasized the dynamics of cantilevered plates that are clamped at the leading edge and free on other three edges (Huang, 1995; Tang et al, 2009; Howell et al, 2009). Most of their results succeeded in capturing the transient response of the plate vibration. However, there was a controversy on the corresponding mechanism such as the wake effect and the single/coupled mode flutter. The current study attempts to explore the flow-induced vibration of the tensioned membrane installed in the silencer with the consideration of the structural properties and aerodynamic condition. The aerodynamic conditions are categorized as axial (stream-wise) and cross (span-wise) flow condition. Three inter-related parameters are to be studied: membrane tension, the critical speed and the vibration mode shape. The experimental set-up, testing modal configuration and measurement procedure are to be discussed in Section 3.2. The experimental results are to be discussed in Section 3.3, which mainly focuses on both the axial flow and cross flow effects in terms of the spectra and mode of the vibration through the experiments. Finally, several conclusions are drawn based on the analysis in Section 3.4.

## 3.2 Experimental setup

The experiment is undertaken in a closed circuit wind tunnel with the cross sectional area of 100mm by 100mm that was introduced in Chapter 2. The maximum flow speed is 50m/s, which is sufficiently high for inducing the instability of the membrane vibration in the current test. The parallel flow and cross flow past over one membrane which is flush mounted on the rigid duct wall are shown in Figure 3.2(a) and Figure 3.2(b) respectively. To study the parallel flow as shown in Figure 3.2(a), the membrane with a length of 300mm and simply supported at both ends is mounted on the tensile machine and the lateral edges of the membrane are free. To eliminate the extra friction between the lateral edges and the duct and ensure the free vibration there, the width of the membrane 99mm which can give 1mm gap. To study the cross-flow, the membrane with a length of 100mm and a width of 100mm is flush mounted on the duct and three edges are fixed. The trailing edge of the membrane is free to vibrate and there is small gap (1mm) between the trailing edge of the membrane and duct wall. But the tension direction is perpendicar to the flow direction.

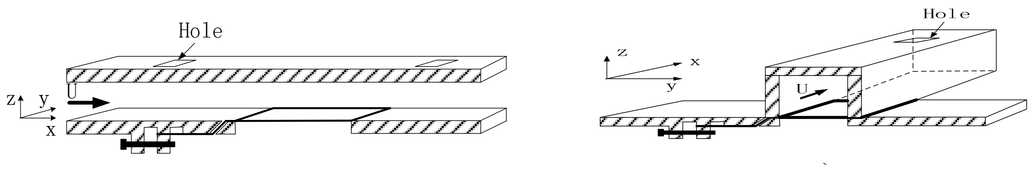


(a) Streamwise tensile force (b) Spanwise tensile force

Figure 3.2 Schematics of experimental configuration

The membrane used is made of stainless steel with density of 7.8g/cm$^3$, thickness of 0.025mm, Young's modulus of 193GPa. The tension can be applied by a tension machine, which is successfully used previously for the performance test of the drum like silencer (Choy, 2002), and the value is read with the aid of the strain gauge (FLA-3-11-1LT) which involves the temperature compensation and a strain gauge indicator by the stress force equation, $T = AE\varepsilon$ , where $A$ is the cross section area of the membrane given by the multiplication of the width and the thickness, $E$ is the Young's modulus and $\varepsilon$ is the strain obtained by the indicator.

The mean flow speed range in the acoustic wind tunnel for the current project can be varied from 5m/s to 45m/s with a turbulence intensity of less than 1%. In order to incorporate with a realistic ventilation system with open inlet and discharge condition, two holes with an area of 50mm x 50mm at the upstream and downstream of the membrane were made as shown in Figure 3.2(a). Note that the upstream hole in Figure 3.2(b) is not shown for clear illustration of the membrane. Therefore, constant atmospheric pressure is imposed at both entrance and exit of the membrane so as to obtain the initial static balance. In order to guarantee the uniformity of the flow the velocity profile is measured by the mini CTA 54N81 and Probe P11 hotwire system from Dantec Dynamics® at the inlet of the duct. Figure 3.3 describes a typical velocity profile in the boundary layer with thickness of about 11mm. There are two observations: (1) the boundary layer becomes thinner as the flow speed increases. And (2) it is also thicker on the wall opposite to the membrane owing to the larger flow separation at the edges of holes as shown in Figure 3.2.

The velocity signal of the membrane vibration is firstly recorded at one given point by the Polytec® single channel laser Vibrometer OFV-512 and OFV-3001. The critical velocity of the instability is found by calculating the growth of the root mean square of the vibration velocity at the centre point of the membrane as a function of the flow speed. Then, the vibration and its mode of the whole membrane are measured by Polytec® Scanning Vibrometer PSV-400, which is more powerful and capable to acquire the vibration signal of the whole membrane automatically in a short time. A low pass filter of 500Hz is used during the final data acquisition since the dominant frequency of the instable vibration measured both by Choy(2007) indicated that the frequency located in the range of 100Hz to 200Hz. The sampling frequency is 5000Hz. The reference signal is the vibration output of one selected point on the membrane surface ,in which there is an obvious vibration level，measured by the single channel Laser Vibrometer (OFV-512 and OFV-3001). The averaged spectrum of the vibration and the deformation and mode shape of the membrane will be analyzed in the post-processing procedure.

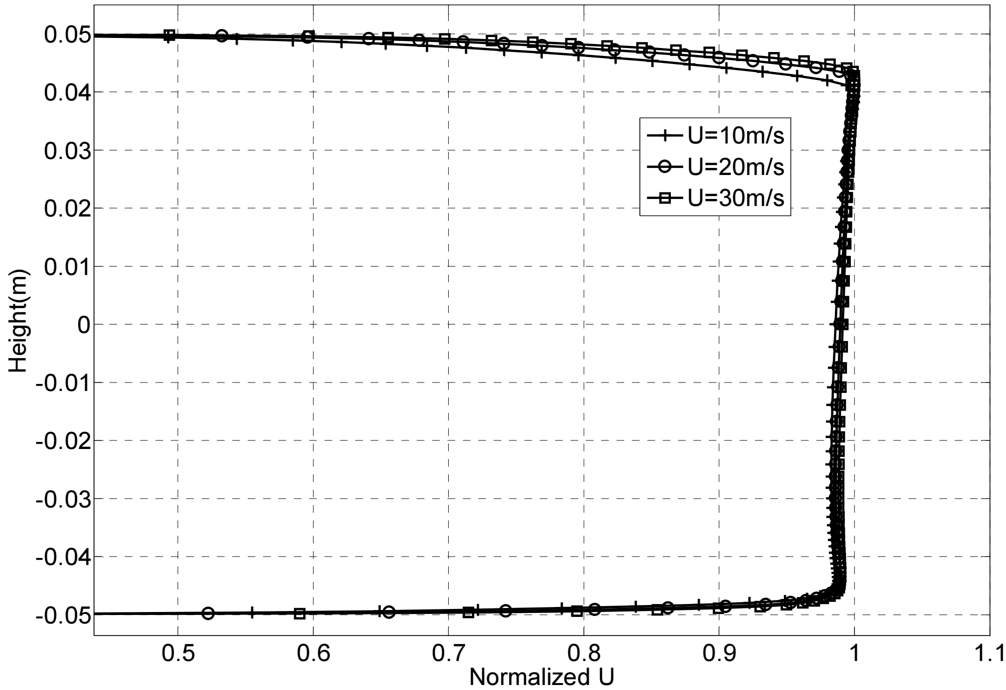


Figure 3.3 Velocity profiles at the inlet of the duct, the velocity is normalized by the upstream flow speed

## 3.3 Results and discussions

### 3.3.1 Onset of instability

The loss of stable vibration for the membrane is examined in this section. There are several concerns on the definition of a critical velocity to cause the instable vibration

(Chen, 1989). The flow velocity range below and above the critical velocity are called sub-critical and post-critical regions, respectively. It may be found out by time history of the vibration signal and frequency spectrum in the function of flow speed. Among these two methods, the most effective and convenient way in the real situation is to study the increment of the vibration amplitude with increasing wind speed.

The strength of the response of the vibration is quite different in the sub-critical and post-critical regions, and this method is very straightforward in practice. An example is indicated in Figure 3.4 which shows the variation of the vibration velocity of the membrane with the increases of the flow speed. The response of the membrane is monotonically increasing with the flow speed generally. From the flow speed of 5m/s to 15m/s, there is a linear relationship between the response of the membrane and the flow speed. The slope of the straight line depicted in the solid line is relatively gentle. From the flow speed of 15m/s to 20m/s, there is substantial change of the response of the membrane with the flow speed and thus the linear regression line has relatively steep slope. The critical velocity can be determined by the intersection of these two lines with the occurrence between the small oscillation and the start of violent vibration. In the range of supercritical range in which the flow speed is beyond 20m/s, the slope cannot be determined with some non-linear effect. In addition, a logarithmic scale for such plotting is seen to give better results in several works (Axisa *et al.*, 1984), but it is not often used.

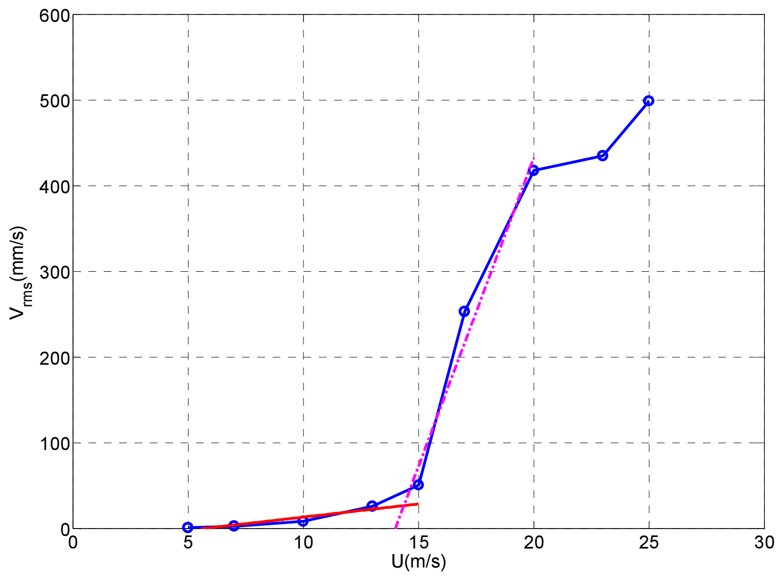


Figure 3.4 Root mean square of the vibration amplitude $V_{rms}$ versus wind velocity $U$, the experimental data of is labeled as the open circle, while the two straight lines indicate the fitting results in the postcritical and subcritcial regions

### 3.3.2 Instability of flow past a tensioned membrane

#### 3.3.2.1 Instability boundary

The structural property of the membrane such as tension is considered in this section. Figure 3.5 shows the variation of the vibration velocity of the membrane with the flow speed under different tensions. When the membrane is applied at the tension of 40N and 80N, the response of the membrane is increased gently with the flow speed when the flow speed is in the range of 5m/s and 15m/s, and then is increased rapidly with the flow speed when the flow speed is beyond 15m/s. When the tension is 120N, the response of the membrane no longer increases with the flow speed when the flow speed is above 20m/s. This shows that the vibration is suppressed significantly by high tension. In this case, the critical speed can be marginally found by the method of interception of two linear lines. In nature, the response of the membrane is fully coupled with the fluid loading and the structural properties of the membrane such as tensile force and dimension. The magnitude and frequency response of the membrane when the instability occurs depend on aerodynamic fluid loading, mass and tension of the membrane as well as the damping. The boundary conditions of the membrane also play a significant role in the divergence and flutter types (Guo CQ, Paidoussis, 2000).

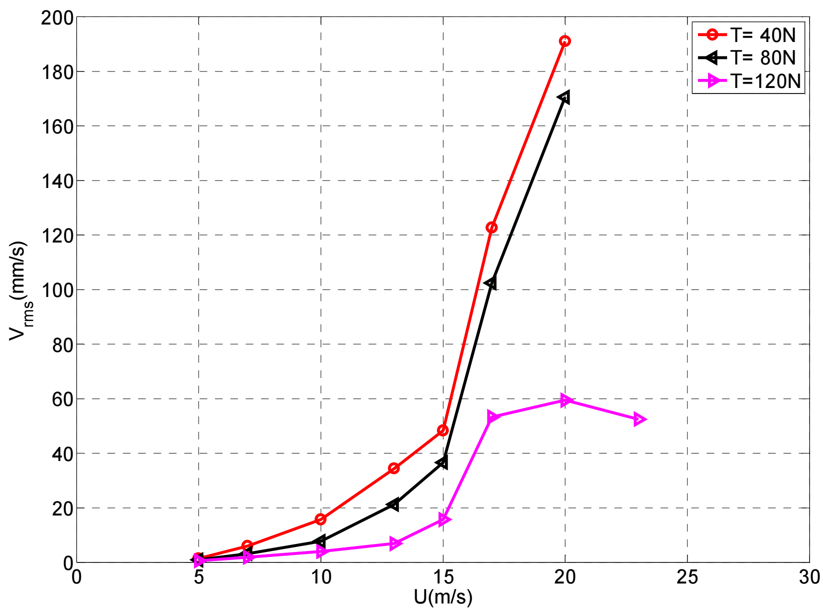


Figure 3.5 Comparison of amplitude growth process for different tensions

#### 3.3.2.2 Spectrum analysis and vibration mode shape

The influence of velocity and tension on the resonant frequency is described in Figure 3.6 which shows the spectrum of the vibration velocity at the center point on the membrane. It is conspicuous that the dominant frequency around 100Hz increases with the increment of both velocity and tension. The resonant frequency of the *in vacuo* membrane is related to the length and mass of the membrane as well as the tension. Roughly speaking, according to Figure 3.6(b), the resonance frequency is shifted to the high-side when the tension is increased. With reference to the Figure 3.6(a), the amplitude of the membrane vibration tends to increase with the flow velocity. The tangential aerodynamic force will be increased with the flow velocity. This will increase the in-plane membrane tension due to the unbalance force between the aerodynamic force in the wind tunnel and atmospheric pressure. Therefore the resonance frequency is also increased. In addition, the amplitude of the response of the membrane is obviously decreased when the tension is increased. This confirms that high tension will stabilize the vibration of the membrane.

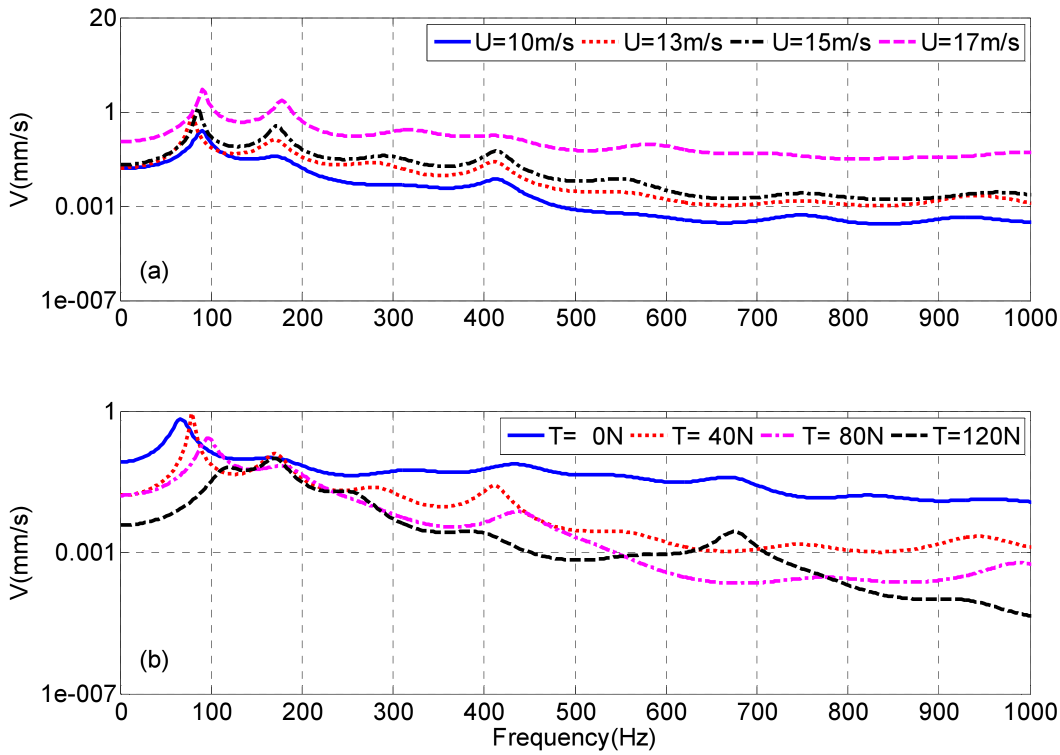


Figure 3.6 Effect of velocity and tension on the vibration frequency (a) The effect of the flow speeds at T=40N (b) The spectra comparison of the vibration velocities for various tensions at U=13m/s

Figure 3.7 shows the averaged spectrum of the membrane vibration at higher flow velocity. There are two observations: (a) the peaks are generally shifted to higher frequencies when the flow velocity is increased and this is consistent with previous analysis in Figure 3.6 and (b) several peaks in the spectrum can be seen. In order to have further understanding of the physics behind on the flow-induced vibration, modal analysis is to be carried out. The distribution of the membrane vibration of whole surface of the membrane under a tension of 40N at different flow speeds of 17m/s and 35m/s is shown in Figures 3.8(a), (b) and Figure 3.9 (a), (b) respectively. In Figure 3.8(c), there are two sharp peaks at low frequencies. The corresponding distribution of the membrane vibration at these two frequencies shows that the first mode is dominant. The displacement is considerably reduced at the lateral free edges. This may be attributed to the added mass on the membrane due to the air flow. Vaughan (2010) explored the coupling effect of flow on the free edges of a uniaxially tensioned web, which easily deflect under flow. The effective mass of the membrane is increased owing to the surrounding air. Consequently, the fluid inertia has a more prominent effect at the edges than at the center of the membrane.

As the flow speed is increased to 35m/s in the supercritical range, three peaks at the frequency of 90Hz, 150Hz and 202Hz can be found in Figure 3.9(d). There is some difference on the deformation of the membrane between low flow speed and high flow speed conditions. The first *in vacuo* mode of vibration is only observed at the first peak of 90 Hz which is shown in the subfigure 3.9(a). On the other hand, the second *in vacuo* mode shape becomes dominant at the second and third peaks of frequency 150Hz and 202Hz as shown in Figures 3.9(b) and (c). The modal vibration of the membrane at these three peaks can be referred to frequency clustering (Tzou *et al.*,1998) on condition that the ratio of bending stiffness to tension is as small as the order of magnitude of $10^{-5}$ . The ratio can be calculated by $h^3 E/(12a^2(1-\mu)T)$, where $E$ is the Young's modulus, $h$ is the membrane thickness, $a$ is the width, $\mu$ is the Poisson's ratio, and T it the tensile loading. In the current study, the value is the order of magnitude of $10^{-4}$ and can be considered to be very low.

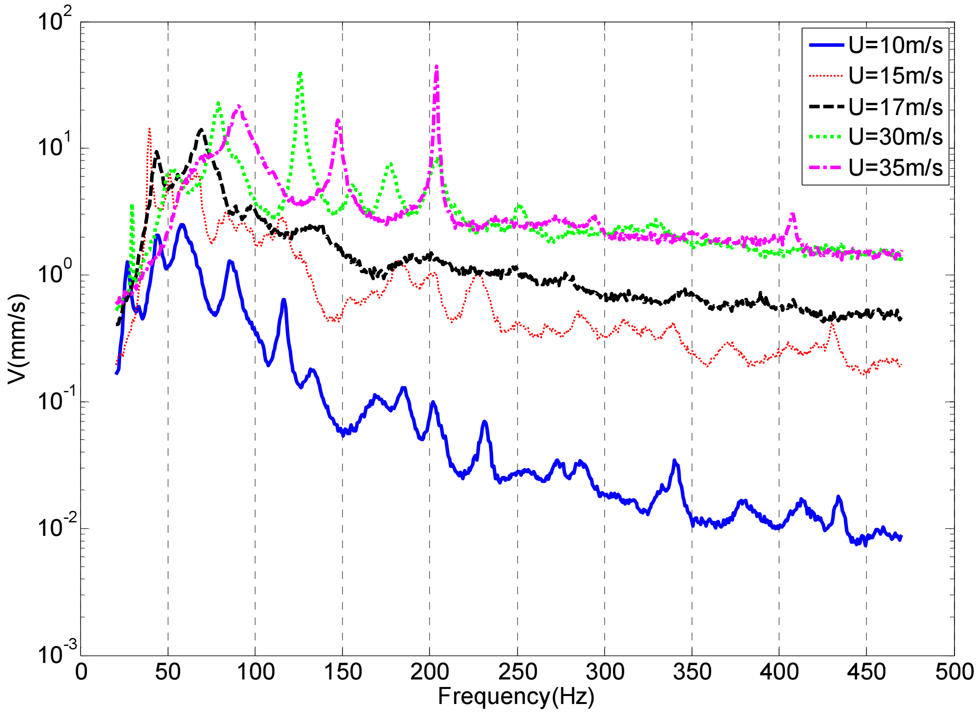


Figure 3.7 Averaged spectra comparison of the whole membrane surface at T=40N under different flow velocities

It is very important that the second *in vacuo* mode of vibration only appears at very high flow speeds. In other words, higher order modes can be observed at high frequencies when the flow speed is sufficiently high. Such vibration behavior of a structure with the effect of flow was previously seen (Vaughan, 2010), however, higher order mode excitation is not that obvious in the current investigation compared with previous works.

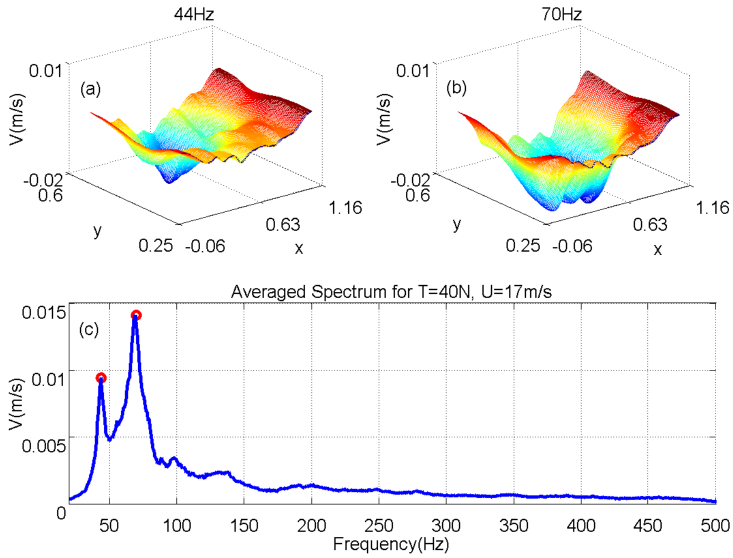


Figure 3.8 Frequency response of the membrane at T=40N, U=17m/s (a) The vibration velocity distribution of the membrane at the first peak of f=44Hz (b) The velocity distribution at the second peak of f=70Hz (c) The averaged spectrum of the vibration of the whole surface

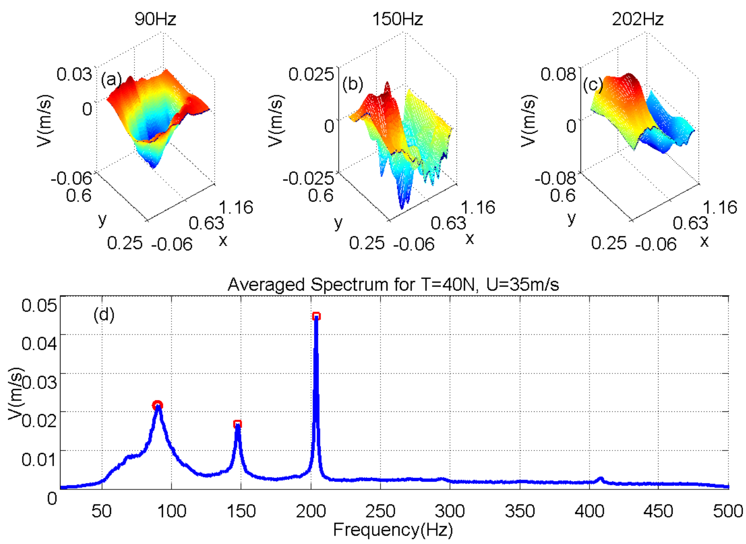


Figure 3.9 Frequency response of the membrane at T=40N, U=35m/s (a) The vibration velocity distribution of the membrane at the first peak of f=90Hz (b) The velocity distribution at the second peak of f=150Hz (c) The velocity distribution at the third peak of f=202Hz (d) The averaged spectrum of the vibration of the whole surface

### 3.3.3 Instability of cross flow past a tensioned membrane

#### 3.3.3.1 Critical velocity

In what follows, the vibration features of a tensioned membrane undergoing the cross-flow condition are discussed in this section. The growth of the vibration amplitude of the membrane in the fluttering under different tension is shown in Figure 3.10(a). Basically, such response of the membrane in the cross-flow is similar to that of the membrane in stream wise flow configuration. Similarly, the vibration is suppressed by the increment of tension. Figure 3.10(b) depicts the variation of critical velocity against the tension. In order to validate the experimental result, a simplified analytical model based on the potential flow theory (YB Chang 2002) is used to predict the critical velocity. The analytical model is reviewed briefly herein and the modification on this theory based on the current investigation will also be made and described in this section.

In this model, the air flow is assumed to be two dimensional, and the aerodynamic pressure is expressed by the in viscid flow equation given by

$$p_{\pm}=-\rho[\frac{\partial\phi}{\partial t}+U_{air}\frac{\partial\phi}{\partial y}]_{z=0\pm} \quad , \tag{3.1}$$

where $\phi$ is the velocity potential.

Notice that $p_-$ is set to be zero because there is no air flow on the outside surface of the membrane.

The governing equation of the out of plane motion of the membrane is described as

$$m(\frac{\partial^2 w^2}{\partial t^2})+(D_x\frac{\partial^4 w}{\partial x^4}+D_{xy}\frac{\partial^4 w}{\partial x^2\partial^2 y}+D_y\frac{\partial^4 w}{\partial y^4})-(T_x\frac{\partial^2 w}{\partial x^2}+T_{xy}\frac{\partial^2 w}{\partial x\partial y}+T_y\frac{\partial^2 w}{\partial y^2})+p=0 \qquad (3.2)$$

where the bending stiffness $D_x=\frac{\mathrm{E}_x h^3}{12(1-\nu_x\nu_y)}$, $D_y=\frac{\mathrm{E}_y h^3}{12(1-\nu_x\nu_y)}$, $D_{xy}=D_x\nu_y+\frac{Gh^3}{6}$ , $m$ is the mass per unit area of the membrane, $w$ is the displacement in the out plane direction, $t$ is the time, $T$ is the tension.

The deflection of the membrane is assumed to be expressed as a travelling wave:

$$w=\hat{w}\sin(\frac{\pi x}{L})e^{i(\omega t-ky)} \quad , \qquad (3.3)$$

The boundary conditions for the membrane are shown as follows. The vertical velocity of the membrane is

$$\left.\frac{\partial\phi}{\partial z}\right|_{z=0\pm}=\frac{\partial w}{\partial t}+U_{air}\frac{\partial w}{\partial y}, 0<x<L \ , \qquad (3.4)$$

The velocity at the leading and trailing edges of the membrane is zero, then

$$\frac{\partial\phi}{\partial x}=0 \quad \text{for } x\in[0,L] \qquad (3.5)$$

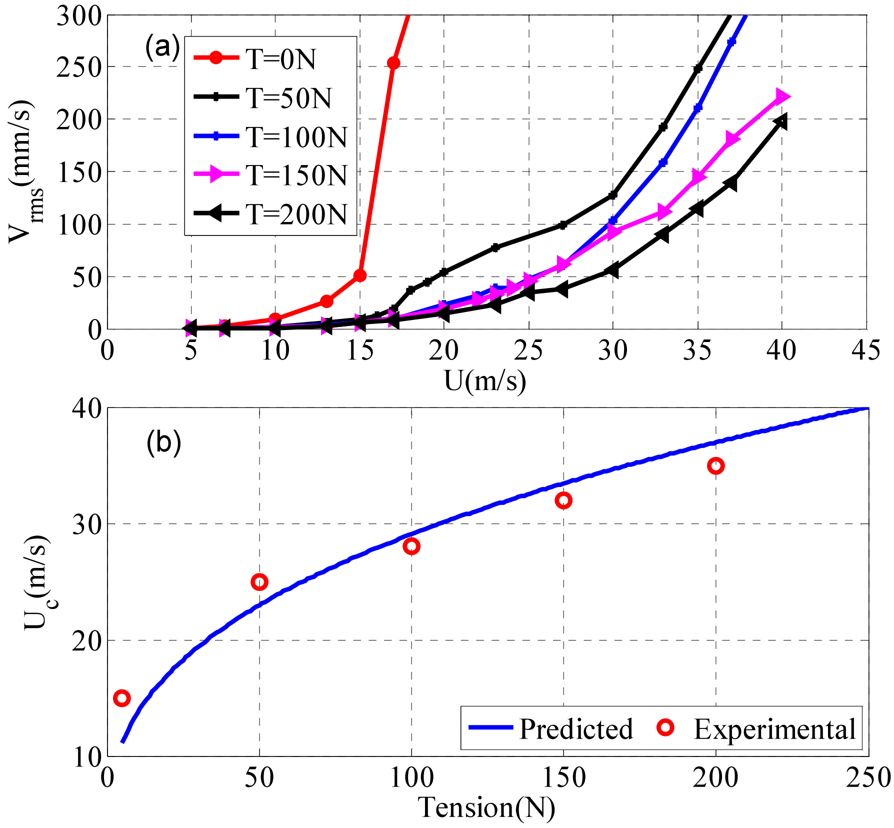


Figure 3.10 (a) Vibration velocity of the membrane at different flow speeds and (b) Variation of the critical velocity under different tensions

By using the traditional methods of the separation of variable, the solution of the characteristic equation can be obtained and the critical velocity can be determined from the following relationship according to the *eigen*-value analysis.

$$\bar{c}_r = \frac{4sMU_c}{\pi^2 + 4sM} \tag{3.6}$$

In all the results, parameters are normalized based on the mass ratio $m$, membrane length $L$ and speed of sound $c_0$. By doing so, the dimensionless parameters are expressed as follows:

$c_0^2 = \dfrac{\pi^2 D_x}{mL^2}$ , $\bar{c} = \dfrac{c}{c_0}$ , $\Lambda = \dfrac{\lambda}{2\mathrm{L}}$ , $\mathrm{M} = \dfrac{2\rho L}{\pi m}$ , and $s = \Lambda + \dfrac{2}{9\sqrt{4+\Lambda^{-2}}}$ .

The critical velocity under different tensions predicted from Eq. (3.6) is plotted with solid line in Figure 3.10(b). Compared with the experimental results (open circle point), roughly speaking, there is a good agreement between experimental data and prediction. Moreover, the critical velocity seems to be more sensitive at low tension since the slope of the predicted curve is relatively steep at low tension region.

### 3.3.3.2 Spectrum and vibration mode

The averaged vibration spectrum of the whole membrane surface at different flow velocities under the cross-flow condition is shown in Figure 3.11. Similar to the parallel flow condition, the amplitude of the membrane response is increased with the flow speed. There are several peaks and the modal vibration is to be discussed in the following section.

Figure. 3.12 shows the oscillation of the vibration of the membrane in the time domain. Figures. 3.12 (a), 3.12(b) and 3.12(c) shows the vibration pattern for flow speed of 15m/s, 25m/s and 35m/s respectively. From the observation of these three figures, the evolution of the vibration of the membrane in the span-wise center line can be divided into three typical stages in terms of the flow speed. (a) the 1st mode vibration dominates at low velocity, (b) coupled 1st and 2nd mode is observed near the critical velocity and (c) the higher order mode of vibration is observed at the velocity higher than the critical velocity. The modal coefficient contribution can be decomposed approximately using the Fourier analysis and the vibration velocity of the membrane can be expressed as

$$\mathrm{V}=\sum_{j=1}^{\infty} V_j \phi_j(x) , \tag{3.7}$$

and $$\mathrm{V}_j = 2\int_0^1 V \phi_j(x) dx \tag{3.8}$$

where $\phi_j(x) = (\cos\frac{\lambda x}{L} - \cosh\frac{\lambda x}{L}) + \beta(\sin\frac{\lambda x}{L} - \sinh\frac{\lambda x}{L})$ is the modal shape function for a cantilevered-free beam. And for the first four modal coefficients $\lambda$

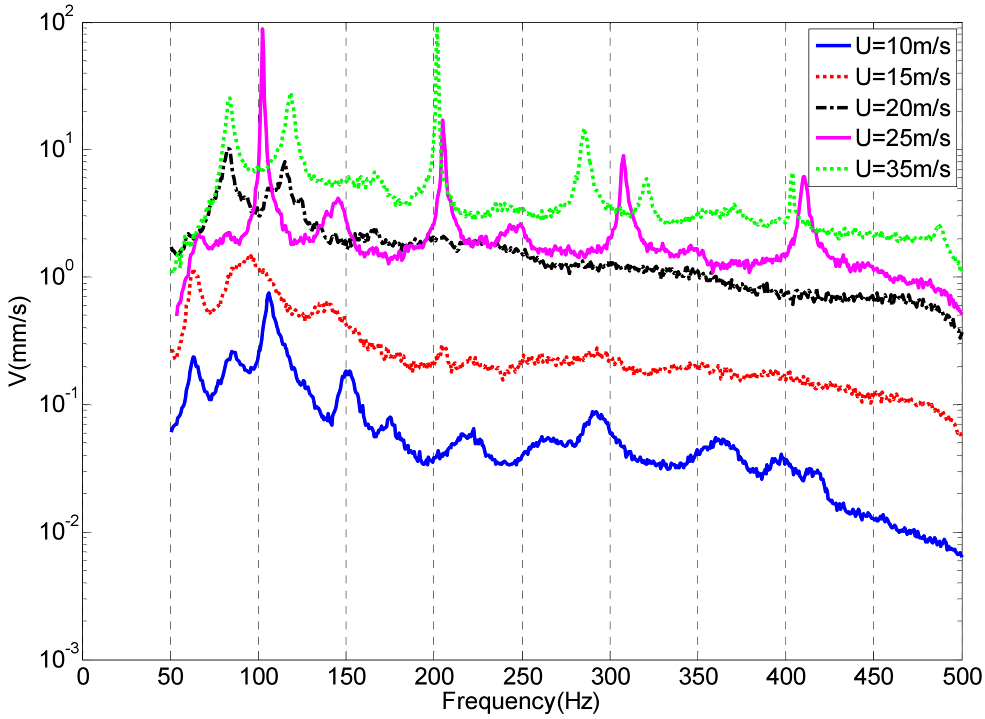


Figure 3.11 Averaged spectrum comparisons under different cross flow velocities

and $\beta$ are considered and they are given as

$$\lambda = 1.8751,\ 4.6941,\ 7.854757,\ 10.99554\ ,\quad \beta = \frac{\cos(\lambda)+\cosh(\lambda)}{\sin(\lambda)-\sinh(\lambda)}\ . \tag{3.9}$$

Higher order modes than the fourth mode were omitted since they have much smaller amplitudes. The vibration of the membrane can be modeled as the cantilevered beam motion and the strength from fluid loading is referred to the previous findings. Note that the whole surface of the membrane may not be fully excited at low flow speeds because of the fixed edges. During the modal decomposition, the leading edge of the excited membrane is not constant and it is approximated at the point where the amplitude is ten times as that of the leading edge point at the lowest flow velocity measured when the flow speed is lower than 30 m/s in the current study. The approximated point is labeled as an open square in Figures 3.12(a) and (b). The contribution of the modal amplitude of each mode in percentage is listed in Table 3.1. At the low speed, the contribution by the first mode of vibration to the overall membrane vibration is very high which is about 80%. When the flow speed is increased to about 35m/s, the contribution by the first mode part becomes less and even decreased by nearly 40%. The higher order mode portion becomes more and more obvious and such pattern can be seen in Figure 3.12(c).

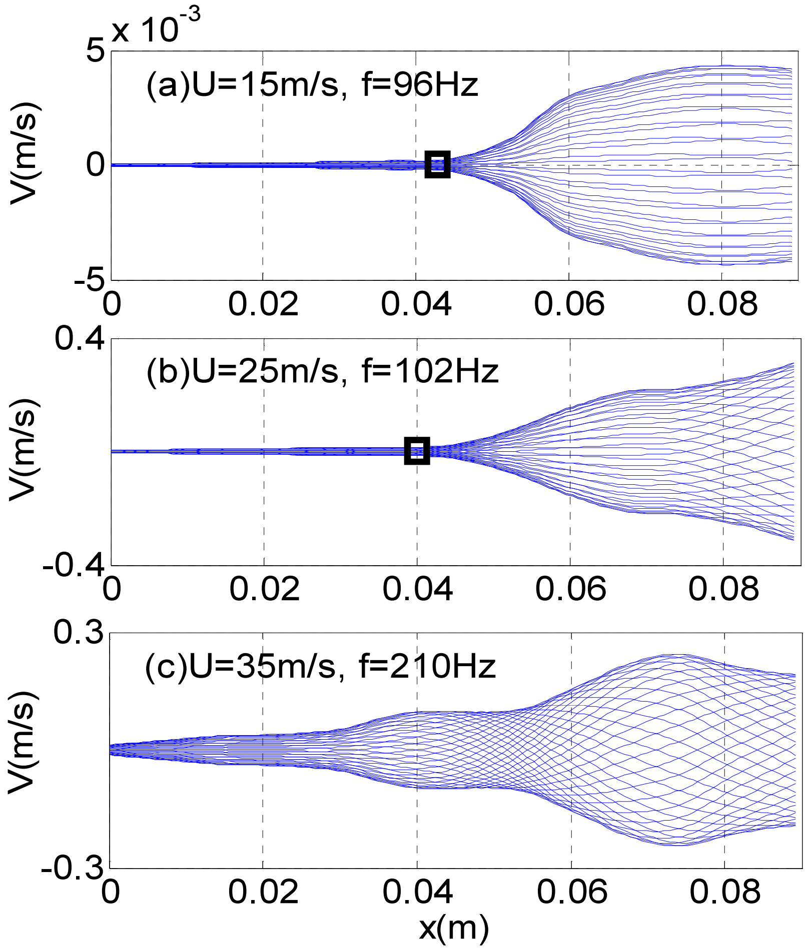


Figure 3.12 The evolution of the streamwise envelope of the membrane for T=50N

**Table 3. 1 Distribution of the vibration mode component for three velocities**

| | 1st mode | 2nd mode | 3rd mode | 4th mode |
|---|---|---|---|---|
| U=15m/s | 80% | 9% | 9% | 1% |
| U=25m/s | 74% | 20% | 3% | 2% |
| U=35m/s | 44% | 29% | 16% | 10% |

## 3.4 Conclusions

The fluid loading on the membrane is found to be very important to influence the occurrence of the instable vibration on the tensioned membrane in the drum-like silencer. Two directions of the flow passing over the gap of the membrane have been investigated. One is axial flow and the other is cross flow. The characteristics of the unstable vibration due to two kinds of flow past over a tensioned membrane wall have been investigated experimentally. Based on the findings in the current chapter, several conclusions have been drawn as follows:

(1) The critical flow speed for the occurrence of the vibration instability of the membrane due to the flow past over membrane in the axial or tangential direction has been found. There is close agreement between the experimental data and prediction from the modified theoretical model based on potential theory. The peak frequency of the vibration increases with the increment of both loading tension and the flow speeds.

(2) For the axial flow past over the membrane, at low flow speeds, the first mode is dominant at all peaks in the frequency spectrum while at high supercritical flow speed, the first mode remains dominant only at the first two peaks in the spectrum and the second mode becomes prominent at other peak frequencies. This is similar to the findings (Raman, 2001) that clustering phenomenon is determined by the ratio of the

bending stiffness to the tension.

(3) For the tensioned membrane with a uniform cross flow, there are three kinds of modal combinations for the vibration of the tensioned membrane in the instability phenomenon. At low flow speed, the first mode of vibration is dominant. And at critical flow speed, the first and second modes of vibration are coupled together and the coupling becomes dominant. At high supercritical flow speed, the higher order mode becomes more and more obvious.

# Chapter 4 Numerical studies on the noise control of a dipole source by the silencer with tensioned membranes

## 4.1 Introduction

Having investigated the instability phenomenon of the membrane in Chapter 3, the use of the tensioned membrane on the control of the dipole noise source is going to be studied in the ventilation system practically. In order to avoid the occurrence of flow induced vibration, two main considerations are reviewed here for the new design based on the findings in Chapter 3:

1) The instable vibration destroys the performance of the silencer, but it can be suppressed by the increment of the tension, which means the tension can compensate for the drop of the noise reduction. The application of the silencer or any modification on it is focused on the optimized performance at a lower tension without flow. So, in the presence of flow, the probable unstable vibration will be prohibited by slightly increasing the tension.

2) As far as the instability of the tensioned membrane is concerned, the cross flow effect attributed to the air leakage through the gap is more crucial than that under the condition of the axial flow. Thus, factors that may induce cross flow should be eliminated in the future design.

The use of the tensioned membrane has been extensively studied (Huang, 2002, Choy and Huang, 2009) to control the plane incident sound waves at the propagation path. However, the design concept can be quite different when a dipole noise source is put just inside the silencer. In this situation, the noise radiation is expected to be reduced by the control of the source rather than through the propagation path. The motivation originates from the innovative idea of employing the reactive method to suppress the sound radiation from an axial flow fan proposed by Huang (2010). The radiated noise is abated by putting the noise source, e.g., the fan, at the center of an expansion chamber, in which the fan can be regarded as a pure dipole source. The numerical procedure for the simulation of a simplified ducted fan noise radiation with casing treatment has been conducted by virtue of the spectral method of Chebyshev collocation. Preliminary experiments have been conducted to verify the numerical findings. In general, the experimental results are in good agreement with the numerical predictions. The noise reduction derives from two mechanisms, one being the reduction of sound intensity by the confined duct, the other being the wave reverberation effect in the chamber by the junctions. However, one drawback of the design in practice is change of the fan induced flow in the case of the expansion chamber. The flow drawn through the duct is much smaller due to the obvious pressure losses at the two junctions. To keep the same flow condition, the inner segment of the expansion chamber is covered by a thin PVS membrane. The membrane is considered to be acoustically transparent but can confine the flow. As the flow speed of the fan increases, however, the stress force is introduced on the membrane and the large deformation of the membrane appears due to the pressure difference induced by the flow. The deformation brings the undesirable interference with the acoustic field and flow field which is excluded in previous study.

An alternative method is proposed here by applying the tension on the membrane to overcome the deformation. Logically, the enclosing dipole by the tensioned membrane shares the same configuration of the drum like silencer. But, several questions may arise when the silencer with tensioned membranes is employed in the dipole source control: (a) does the tensioned membrane destroy the effect on the noise attenuation? (b) what is the coupling relationship between the membrane's vibration and the reflection in the cavity? (c) what is the difference between the mechanism of the noise abatement in the control of the monopole and dipole sources? In this chapter, the performance of dipole noise reduction by the silencer with tensioned membranes is investigated numerically based on a simplified 2D model. And the analysis aims at answering the above problems and the physics behind. Further studies with a realistic 3D model and the experimental validation on the noise reduction of the axial flow fan will be presented in the next chapter.

In what follows, the numerical methodology and model are described firstly in detail to explain the theoretical background. With the numerical model established, the optimization procedure is carried out and the optimal results are also presented in terms of the mass ratio and the tension of the membrane. Finally, the mechanism behind to explain the performance of the silencer is discussed and the discrepancies with the noise control of a monopole source as well.

## 4.2 Numerical method

A finite element modeling procedure is established to investigate the performance of the noise control for a dipole source by the silencer with tensioned membranes. Although a theoretical formulation has already been established in (Huang, 2010) to simulate the fan noise control in a circular duct for linear interaction between sound and structure, its direct application to the current study is inappropriate for reasons given below. In Huang (2010), the spectral method of Chebyshev collocation with domain decomposition is employed. The advantage of that method lies in the rapid convergence and great accuracy compared with other methods such as the fourth order finite difference method (Huang, 2008). However, in the current design, the coupling between the membrane vibration and the acoustic field plays a significant role. Although it is possible to extend the existing theoretical formulation to cover the full structural-acoustics couplings, it can be too complicated to be feasible in practice. Besides, to calculate the radiation contribution from the dipole source, the results should undergo Fourier transform in circumferential direction, which limits the application of this method to circular configurations only. It is hard to extend the said theoretical formulations to a real three dimensional (3D) silencer design which may involve complicated geometrical configurations. Due to versatility of the finite element method in modeling the complex geometries and multi-physics problems, a finite element model is more suitable and feasible for the current study.

### 4.2.1 The theoretical model

Figure 4.1 shows the two dimensional (2D) configuration of the dipole source control by the silencer with two pieces of tensioned membranes. It consists of three main parts, including the upstream and downstream duct, and a cavity-backed membrane in the middle segment. The loudspeaker or the fan, which can be considered as the dipole source, is located at the center of the cavity-backed membrane. The duct and the backed cavity have a height of $h^*$ and $h_c^*$, respectively. The length of the three parts of the duct from left to right is symbolized as $L_{up}^*$ , $L_c^*$ and $L_d^*$ . The asterisks denote dimensional variables while the corresponding dimensionless ones are shortly introduced without asterisks. The leading edge and trailing edge of the membrane are simply supported at $\left|x^*\right| = L_c^*/2$, and the tension is loaded in the axial direction $x^*$ . The flexible membrane has a mass per unit length $m^*$ , and the tensile force $T^*$ .

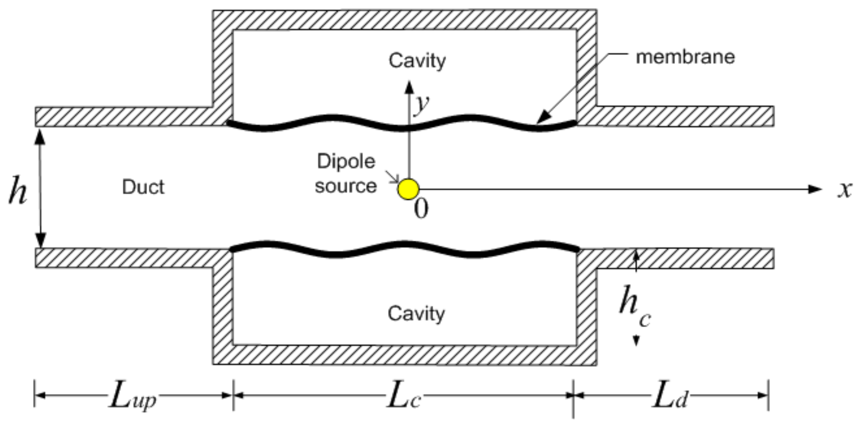


Figure 4.1 2D simulation model of the dipole noise control by the silencer with tensioned membranes

The governing equation for the lower membrane vibration is

$$m^* \frac{\partial^2 \eta^*}{\partial (t^*)^2} - T^* \frac{\partial^2 \eta^*}{\partial (x^*)^2} + (p_+^* - p_-^*) = 0 \quad , \tag{4.1}$$

where $\eta^*$ is the membrane displacement, and $(p_+^* - p_-^*)$ is the fluid loading on the membrane located at $y^* = -h^*/2$. Positive loading means a net force acting downwards, and positive modal impedance, which is introduced later, refers to positive loading induced by an upward membrane vibration velocity. Structural damping in such a thin membrane is normally very small and is excluded.

To simplify the derivation, all the variables are firstly nondimensionalized as follows by three basic quantities $\rho_0^*$ , $h^*$ and $c_0^*$ .

$$x = \frac{x^*}{h^*} \ , y = \frac{y^*}{h^*} \ , \ t = \frac{c_0^* t^*}{h^*} \ , h_c = \frac{h_c^*}{h^*} \ , f = \frac{f^* h^*}{c_0^*} \ , \ \omega = \frac{\omega^* h^*}{c_0^*} \ , \ k_0 = 2\pi f \ , m = \frac{m^*}{\rho_0^* h^*} \ ,$$

$$T=\frac{T^*}{h^*\rho_0^*(c_0^*)^2}\ ,\ \ p=\frac{p^*}{\rho_0^*(c_0^*)^2}\ , \tag{4.2}$$

where $m$ is the mass ratio of the membrane to the air and $T$ is the dimensionless tensile force. In reality, $T$ is calculated by dividing the total force applied on the membrane by $\rho_0^*(c_0^*)^2 A_0^*$, where $A_0^*$ is the cross section of a rectangular duct. Based on such a normalization scheme, the first cut on frequency of the rigid walled duct is $f=0.5$ . Besides, the dimensionless angular frequency $\omega$ is equal to the dimensionless wave number $k_0$ and they are interchangeable.

Through the dimensionless process, Eq. (4.1) becomes:

$$m\frac{\partial^2\eta}{\partial t^2}-T\frac{\partial^2\eta}{\partial x^2}+(p_+-p_-)=0 \tag{4.3}$$

On the other hand, the acoustical field of the entire domain satisfies the in homogeneous Helmholtz equation:

$$\nabla\cdot(-(\nabla p-q))-k^2p=Q\,. \tag{4.4}$$

In the above dimensionless form, $q$ and $Q$ respectively refer to the dipole source and monopole source, which are optional. In the present study, the dipole source of the loudspeaker or the fan noise is treated as an entirety. At the low frequency limit, $f\to 0$ , the dipole radiation is rapidly turned into plane waves. Thus the normal vibration of the membrane is subjected to the plane wave excitation.

The boundary condition on the hard walls is well known,

$$\frac{\partial p}{\partial n} = 0 \ , \tag{4.5}$$

where $n$ is the local outward normal direction .The rigid boundary is one where the normal component of the particle velocity vanishes and it is of a homogeneous Neumann type.

As for the boundary with the impedance, it is the generalization of both hard and soft boundaries as expressed in the frequency domain by the following formula:

$$n \cdot (\nabla p - q) + \frac{i\omega p}{Z} = 0 \quad . \tag{4.6}$$

Where $Z$ is the acoustic input impedance of the external domain. From a physical point of view, the acoustic input impedance is the ratio between the sound pressure and the normal particle velocity. The impedance boundary can be approximately regarded as a locally reacting surface, that is, a surface for which the normal velocity at any point depends only on the pressure at that exact point.

The outgoing wave can be simply described as

$$ik_0 p + \frac{\partial p}{\partial n} = 0 \ . \tag{4.7}$$

The outgoing wave condition for a plane wave is applied for the exits at the two ends of the duct in this chapter. The impedance for open end condition is to be considered in next chapter for the experimental verification in practice. Concerning Eqs. (4.6) and (4.7), the impedance $Z$ is unity for the outgoing wave.

For harmonic wave, the vibration velocity of the membrane can be expressed as

$$V = \frac{\partial \eta}{\partial t} = i\omega\eta \ , \tag{4.8}$$

As shown in Eq. (4.3), the vibration is fully coupled with the acoustical loading from the dipole source. The vibrating velocity of the membrane $V$ can be expanded as a series of *in vacuo* modes with modal amplitude $V_j$, for the simply supported boundary at the leading and trailing edges,

$$V = \sum_{j=1}^{\infty} V_j \sin(j\pi\xi) \ , \tag{4.9}$$

Here $V_j$ is the $j^{th}$ complex modal amplitude of membrane's vibration and $\xi = x / L_c + 1/2$ is the local axial coordinate.

After the expansion of $V$, the Eq. (4.3) then becomes

$$L_j V_j + 2\int_0^1 (p_+ - p_-)\sin(j\pi\xi)d\xi = 0 \ , \tag{4.10}$$

where

$$L_j = [mi\omega + \frac{T}{i\omega}(\frac{j\pi}{L})^2], \quad j = 1,2,3,... \ . \tag{4.11}$$

And $L_j$ is regarded as the structural impedance, which is dependent on the physical properties of the membrane such as the mass ratio, tension and so on.

Further, the pressure loading $(p_+ - p_-)$ on the membrane consists of two components, namely the sound radiation in the main duct $p_{+rad}$ and the pressure inside the cavity $p_{cav}$ which is the combination of the radiation on the lower surface of the membrane $p_{-rad}$ and the reflection in the cavity $p_{-ref}$ . As described in the following expression:

$$(p_+ - p_-) = p_{+rad} - (p_{-rad} + p_{-ref}) = p_{+rad} - p_{cav} \quad . \tag{4.12}$$

The complex amplitude of the radiated sound $P_{+rad}$ is the sum of contributions made by all individual membrane vibration modes, which can be expressed in the following equation:

$$P_{+rad} = \sum_{j=1}^{\infty} V_j R_j \quad , \tag{4.13}$$

where $R_j$ is the complex amplitude of the radiated sound by the induced vibration of the $j^{th}$ mode with unit amplitude and the expression for $R_j$ is given in Huang (2002). The related index $\gamma_j$ is used later to refer to the radiation contribution of each single mode, denoted as $V_j R_j$ , towards the total radiation. Note that $V_j R_j$ is complex and can be represented by a vector, then the interference between two different modes can be found by the separation angle of the vectors.

As for the resultant pressure loading, it contains the source mode of index $j$ as well as of all other induced modes. Suppose $(p_+ - p_-)_j$ is the radiation pressure caused by the modal vibration of unit amplitude, the total modal impedance is defined as,

$$Z_{jl} = 2\int_0^1 (p_+ - p_-)_j \sin(l\pi\xi) d\xi \quad , \tag{4.14}$$

where subscript $j$ refers to the source vibration mode while $l$ the resulting pressure coefficient. Then $Z_{jl}$ can be decomposed in terms of the pressure components with the help of Eqs. (4.12) and (4.14) :

$$Z_{jl} = 2\int_0^1 (p_{+rad} - p_{cav})_j \sin(l\pi\xi) d\xi = Z_{+rad} - Z_{cav} \quad , \tag{4.15}$$

Here $Z_{+rad}$ and $Z_{cav}$ denote the modal impedance in the duct and cavity, respectively. The details of the derivation process for the impedance are given in Huang (2002), and the expressions for them are not repeated but are still employed for further analysis.

Last but not the least, three typical noise indicators can be used to show the level of noise abatement. These are insertion loss, noise reduction and transmission loss. Normally, in order to focus on the performance of the control element, transmission loss (TL) is adopted as it is independent of the impedance of both the noise source and the downstream condition. And it is easy to predict but somewhat difficult to measure in the current situation. It is difficult to have anechoic condition at the end of the duct when there is flow. On the other hand, insertion loss which is easy to measure is commonly used in the realistic applications. Therefore, the insertion loss (IL) is chosen as the main index to evaluate the performance of the noise reduction. To do this, two ducts are established to compute the IL: one being the straight duct with the uniform cross section area; the other being the noise source enclosed in the center of the silencer. The sound energy at the exits of the duct is obtained by integrating $p^2$ on the whole boundary area for each duct. The IL is then found as

$$IL = 10\log_{10}\left|\frac{\int_{Str} {p_{Str}}^2 ds}{\int_{Exp} {p_{Exp}}^2 ds}\right| , \tag{4.16}$$

where 'Str' and 'Exp' denote the straight duct and the expansion chamber respectively, 's' is the exit surface area.

### 4.2.2 The finite element modeling and its validation

The accuracy of the finite element simulation depends mostly on the mesh property, size and the solver. To guarantee the reliability of the simulation, it is necessary to verify the finite element analysis with a well established method. To solve the coupled system numerically, the finite element software package Comsol Multiphysics®, which is the extended version of the Partial Differential Equation Toolbox of the popular computing language MATLAB®. Based on the previous models reviewed, the new problem is principally the combination of two independent but typical configurations. They are the dipole control enclosed in the expansion chamber and the coupled structure of the well developed drum-like silencer.

In order to build up the simulation model, two acoustic domains are used. One is the acoustic domain to describe the sound pressure field with a dipole while another is that without sound source. In order to validate such dipole source model by finite element method, the simple configuration of a circular expansion chamber with the dimensionless length of 9.1 and expansion ratio of 4.6 enclosing a dipole source is to be modeled in the first step. When the mesh size is 0.1, the duct and cavity geometries have 4424 and 1050 triangle elements, respectively. Further refinement of the mesh size from 0.1 to 0.05 gives an improvement of 0.01% on the IL result. The deviation is below 0.2dB on average. Figure 4.2(a) compares the IL spectra obtained from both the Fourier Chebyshev spectral method and experimental results (Huang, 2010) with the Finite element method for the dipole control of noise source inside the expansion chamber. The three curves agree well especially at the low frequency range of interest. For the high frequencies, small deviation appears but the general trend matches each other. Such deviation is caused by the coarse mesh scheme for the short wavelength.

On the other hand, the performance of drum silencer without the sound source in the middle has been well investigated both analytically and experimentally (Huang, 2002 and Choy, 2002). The performance of it is also simulated by the finite element method in this study. Figures 4.2(b) shows the comparison of transmission loss (TL) of the drum-like silencer predicted by the FEM and Fourier Chebyshev spectral method while Figure 4.2(c) shows the comparison of reflection coefficients predicted by these two methods. It can be seen that the results by the two methods match each other very well. No obvious deviation can be observed except those at the resonant peaks. In light of these results obtained from the simple expansion chamber with dipole source and drum silencer without sound source, the finite element model is regarded to be sufficiently accurate for the purpose of the study on the drum-like silencer with the installation of the dipole in the middle of the duct.

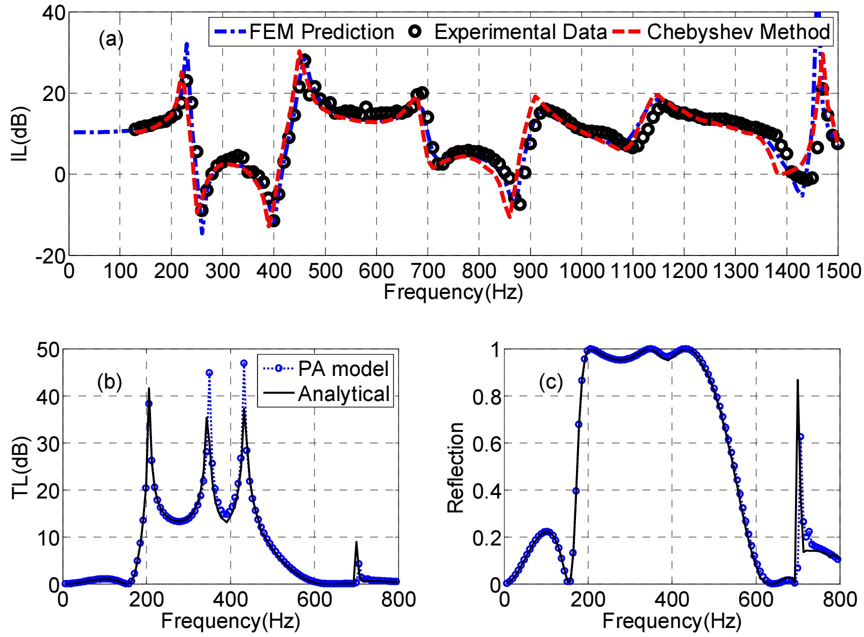


Figure 4.2 Validation of the simulation methods (a) The comparison of the IL control by the dipole source using the FEM with Chebyshev collocation method and experimental results (Huang, 2010) (b) The verification of the drum silencer TL using the simulation with the analytical method

## 4.3 IL spectra and modal interaction

The main objective of the project is to achieve the best performance of the noise reduction in a broad frequency range by the present silencer, especially near the first BPF of the axial flow fan which is normally below 500Hz (0.15 after normalized) and carries most energy. Note that for such configuration, the cavity depth instead of its length is expected to dominate the noise reduction because of the cancellation effect inside the cavity. Thus, the default cavity shape used in this study has a length of $L_c = 3$ and a depth of $h_c = 2$, respectively. In order to attain the broadband reduction, the stop-band which was commonly seen in (Huang, 2002) is adopted here. The stop-band is defined as a frequency range between which the IL (or TL) is everywhere above or at least equal to a criterion value. Expressed symbolically,

$$IL|_{f\in[f_1,f_2]} \geq IL_{cr} \quad \text{and} \quad r_f = f_2/f_1 \ , \tag{4.17}$$

where $r_f$ is the ratio of frequency limits of the stop-band, or the logarithmic bandwidth.

In the current optimization scheme, the criteria value $IL_{cr}$ is defined as the maximum IL obtained from the performance of the simple expansion chamber with the same size of the cavity of the drum-like silencer. With reference to the IL pattern of a pure expansion chamber that has been shown in (Huang 2010), it is found that the maximum IL can be observed at the frequency approaching zero (DC frequency). Based on the criterion value, the optimization procedure is proceeded in order to find out the maximum $r_f$ at different mass ratios m and search for the corresponding optimal tension. It is expected that the silencer can render the desirable performance at the widest stop-band especially in the low frequency region. Such desirable stop-band can also cover the frequency range for the fluctuation of the blade passing frequency due to the change of the rotational speed of the fan. Now the target frequency ratio $r_f$ is at least one octave so that the noise abatement can be achieved when the axial flow fan is operating at various rotational speeds.

### 4.3.1 The optimal spectrum

The optimal results of the overall spectra are presented here before the discussion and analysis of the modal response. In this study, the default cavity shape has a length of $L_c = 3$ and a depth of $h_c = 2$, respectively. We found that the cavity depth is expected to dominate the noise reduction because of the cancellation effect in the cavity. Figure 4.3 shows the performance of the current silencer with the optimal physical parameters for different corresponding the structure-to-air mass ratios.

Figure 4.3(a) shows the corresponding optimal tension $T_{opt}$ for different mass ratios m based on the maximum stop-band scheme. The $T_{opt}$ keeps nearly constant when $m \leq 0.6$ and then decreases sharply to a very low value from $m$=0.6 to $m$=0.8. When

$m$ is beyond 0.8, the $T_{opt}$ remains very small value. Figure 4.3 (b) shows the variation of the corresponding maximum frequency stop-band ratio $r_f$ at different mass ratios with the corresponding optimal tension in Figure 4.3(a). When the mass is increased, the achievable maximum bandwidth $r_f = f_2 / f_1$ decreases. The abrupt change of $r_f$ occurs when $m = 1$ and when the mass ratio $m$ is not greater than unit, $r_f$ achieves at least 2.15, which is still larger than one octave. We found that the

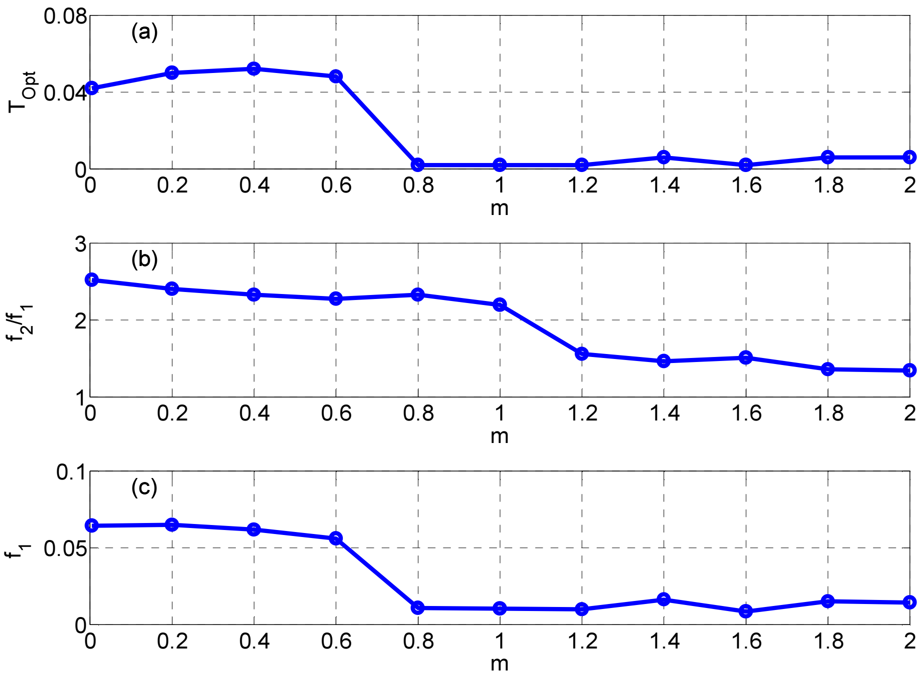


Figure 4.3 Performance optimization of the silencer for the logarithmic bandwidth (a) The variation of the optimal tension $T_{opt}$ with $m$ (b) The variation of $r_f$ as a function of the mass (c) The dimensionless lower band limit $f_1$

performance of the silencer becomes worse immediately as $m$ is larger and drops below the criterion. It is because the membrane is difficult to be excited into the vibration when it is too heavy. Figure 4.3 (c) shows the variation of the lower limit frequency $f_1$ with the variation of mass ratio $m$. The lower limit frequency $f_1$ decreases when mass ratio $m$ is increased. Besides, $f_1$ falls strikingly from 0.06 to a very low level of 0.01 as $m$ reaches 0.8. Therefore, the drop of $f_1$ corresponds with the decrease of $T_{opt}$. Considering the normalized first BPF of a fan usually below 0.14, the silencer is only effective at a low mass ratio and the frequency band ratio $r_f$ is desirable. With reference to the Figures 4.3(b) and 4.3(c), both $r_f$ and $f_1$ change little when $m$ is below 0.4. In general, the optimized result depends much on the mass ratio because large mass ratio will degrade the performance significantly. However, another important factor is that $T_{opt}$ should not exceed the yield point of material. As a result, the optimal performance is found with two requirements of $0.04 \le T_{opt} \le 0.06$ and $m \le 0.6$. Finally, optimal tension $T_{opt} = 0.05$ and mass ratio $m = 0.4$ are selected for the discussion in the following sections. The corresponding $r_f$ is found to be 2.35 while $f_1$ is 0.062.

Figure 4.4(a) illustrates the comparison of the performance between the present silencer with the optimal tension T=0.05 at the mass ratio of 0.4 (solid line) and expansion chamber with the same geometrical size (dotted line). The horizontal dashed line is the threshold level of 9.6 dB which is the maximum IL value for the expansion chamber. It is evident that the IL spectrum of the expansion chamber has a peak performance at the DC frequency, while that of the current silencer experiences a zero dB and even negative IL when the frequency is below 0.06. When the frequency is beyond 0.06, the IL tends to be increased and 10dB IL can be maintained continuously within certain frequency range. On the other hand, IL of the expansion chamber and drum silencer approaches zero at $f = 0.17$ and high order modes in the duct appear beyond $f = 0.2$ when considering the height of the cavity $h_c = 2$. The corresponding wavelength of the zero IL at $f = 0.17$ is 5.9, which is about twice of the membrane length. For the present setting, the lower and upper bandwidth limits are $f_1 = 0.062$ and $f_2 = 0.0145$ and the corresponding stop-band $r_f = 2.35$ is obtained. Such frequency range is the range of interest for current study. Three main peaks are observed at $f = 0.07, 0.136, 0.196$ and labeled as open circular point for easy reference, while the two troughs are at $f = 0.044, 0.146$ and symbolized as the rectangular point. Figure 4.4(b) displays the corresponding $rms$ level of the membrane vibration response calculated by $V_{rms} = (\sum_j |V_j|^2 / 2)^{\frac{1}{2}}$, which stands for the response integrated over the whole membrane .The most striking feature is the appearance of two peaks marked as the open rectangular at the frequencies when the trough point exactly occurs in the IL spectrum. In other words, the trough characteristics are directly dependent on the amplitude of the induced membrane vibration. The sound radiates efficiently towards the two ends of the duct at the two dips so that the noise abatement is extremely weak. As is shown later, the acoustic interference of sound radiated by different parts of the membrane is explored in terms of the vibration modes.

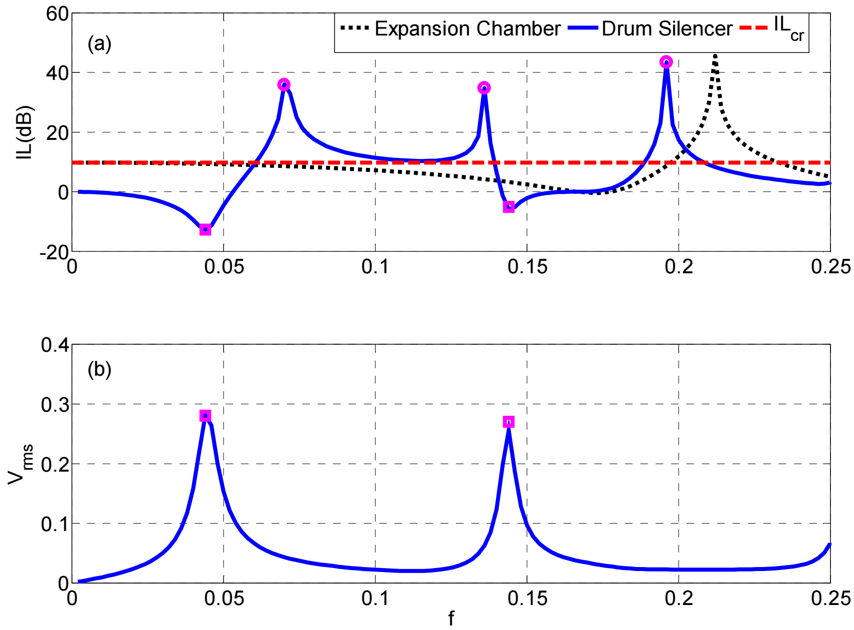


Figure 4.4 Comparison of the IL spectra between the drum silencer at the optimal tension and the expansion chamber for the dipole source

### 4.3.2 Modal radiation

Figure 4.5 presents the modal response of the first four modes for the default membrane at the optimal performance. The IL spectrum is given on the top part of the figure to facilitate the related discussion between the peak and trough frequencies analyzed in Figure 4.3(a), and the modal response. The four columns below illustrate the response from different aspects. The vibration amplitude of each individual mode, $|V_j|$, is shown on the left column first. The second column shows the amplitude of the modal radiation coefficient $|R_j|$. The third column is the amplitude of the single modal radiation $|V_j R_j|$. The last column indicates the modal contribution to the total sound radiation $\gamma_j$ at the two ends of the duct.

The most prominent feature is that the even mode of the membrane response is dominant compared with that of odd modes with reference to the amplitude of the vibration as shown in Figure 4.5(1a) to (1d). Despite the radiation ability of each mode is comparable as shown in Figure 4.5 (2a) to (2d), the total sound radiation $|V_j R_j|$ of the odd modes is still tremendously less than that of the even modes. The similar behavior can be observed for the radiation contribution $\gamma_j$ as indicated in the last column. In this regard, the odd mode effect can be neglected and this reflects the control characteristics of the dipole source in nature.

The corresponding resonance frequencies are indicated by the vertical dashed line and it will be analyzed first. As shown in Figure 4.5(1b), there are two sharp peaks in the second mode amplitude $|V_2|$ and the corresponding frequencies are $0.044, 0.146$ , which are also seen in two peaks of the root mean square vibration amplitude shown in Figure 4.4(b). Similar relationship can be observed in Figure 4.5 (1d) when $f = 0.146$ for the fourth mode $|V_4|$.Actually the peak frequencies which are highly dependent on the tension will be shifted. The two trough points in the IL spectrum can be related to these peak frequencies. As shown in Figure 4.5(4b), it can be observed that there is a positive peak at $f = 0.044$ . The sound radiation towards both upstream and downstream mainly results from the sound radiation contribution from the second mode which is controlled by the dipole source. On the other hand, with respect to the second trough point at $f = 0.146$ in the IL spectrum, there is a negative peak of the modal contribution $\gamma_2$ as shown in Figure 4.5(4b) and a positive peak of modal contribution $\gamma_4$ as shown in Figure 4.5(4d).

Therefore, there is the intermodal coupling and cancellation between the second and the fourth modes and this results in the trough point of IL pattern. Meanwhile, the degree of the intermodal coupling can be found in the first column of Figure 4.5. For instance, the amplitude of $|V_2|$ is much larger than that of $|V_4|$ when the frequency is below 0.12 as shown in Figure 4.4(1b) and (1d), respectively. Beyond $f = 0.12$ , both vibration response of the second and the fourth modes are larger and they are comparable. In other words, the coupling effect becomes stronger with increasing frequency, and the details of the interference are to be analyzed in the next section. Apart from the two trough frequencies, the radiation contribution is nearly flat at a very low level close to zero. Thus it is believed that there is little contribution of the radiation on the IL performance at these frequencies, in other words, the noise radiation towards outside was effectively prohibited.

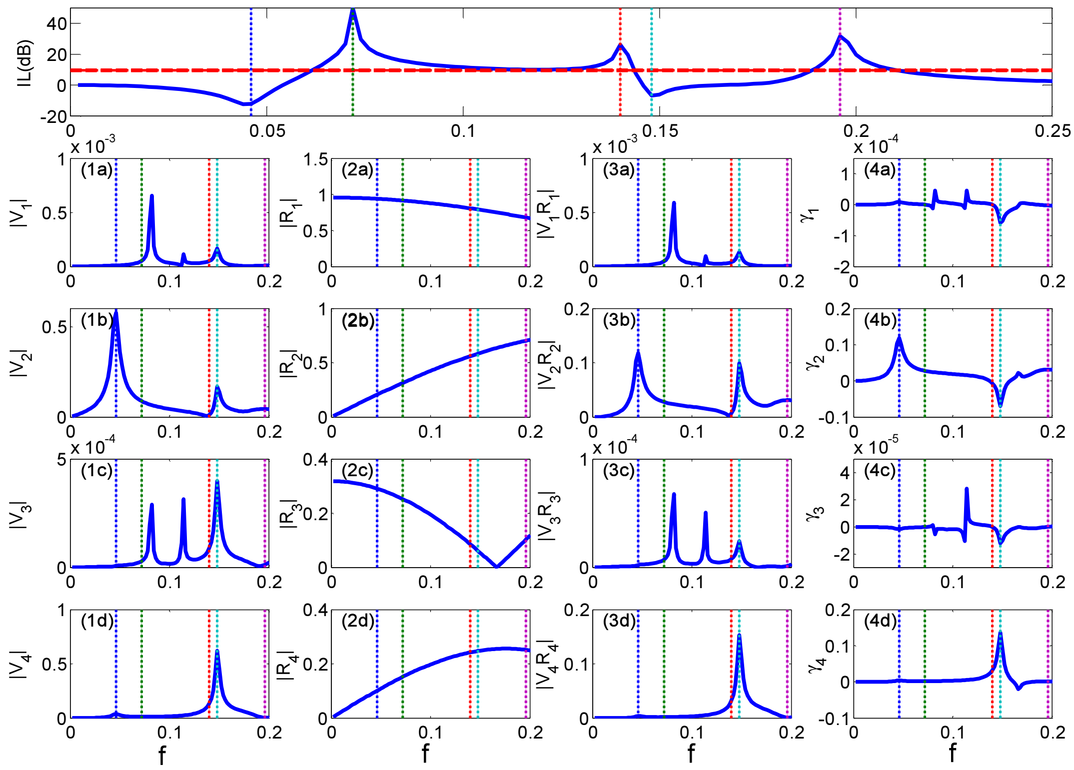


Figure 4.5 Modal radiations. The top figure is the IL spectrum at the optimal tension for the purpose of indicating the important frequencies. The first column on the left is the modal amplitude $|V_j|$, the second column is the modal radiation coefficient $|R_j|$, the third column is the single modal radiation $|V_j R_j|$ and the last column on the right is the modal contribution $\gamma_j$.

### 4.3.3 Parameter study

In this section, the effect of the tension and membrane length on the IL performance of the silencer is investigated when the mass ratio of the membrane is fixed at $m = 0.2$. In order to understand the physics behind, the modal impedance analysis will be discussed in the Sec. 4.3.4. Figure 4.6(a) shows the variation of IL spectrum with the increment of tension for the default configuration with the membrane length of 3. The horizontal dashed line in each sub-figure is 10dB as the reference value. It is clear that the stop-band for IL above the critical value 10dB tends to shift towards high frequencies as the tension increases. Meanwhile, the frequency band becomes wider when the optimal tension below $T = 0.05$ and the lower frequency limit also increases with $T$ .

Beyond the optimal tension, the performance of the silencer deteriorates drastically and the stop-band for IL over the criterion level tends to be narrow and this is undesirable. The optimal IL performances for membrane with their corresponding optimal tensions at different lengths are shown in Figure 4.6(b). Although the criterion values for different cavity lengths are different, the deviation from 10 dB is small. Thus, the criterion of 10 dB is also used. For the length $L_c = 2$ as shown in Figure 4.6(4b), the second peak of IL spectrum does not exceed 10dB and the valley between the first and second peaks is even lower. Besides, the stop-band for IL over the criterion level is extremely narrow in this case. From the observation of the IL pattern at different lengths from $L_c = 3$ to $L_c = 5$, we found that the condition to achieve acceptable wide stop-band over criterion level is that $L_c$ should be larger than 2. And the lower frequency limit $f_1$ reduces when $L_c$ increases. However, the most remarkable feature is that there exits second peak followed by an immediate trough.

Such sharp rise and dip prohibits the further growth of the stop-band $r_f$ , particular for the case of $Lc = 4$ and $Lc = 5$. Otherwise, the IL level will be kept to be very high everywhere until the third peak. For example, the frequency range of the high noise reduction for the membrane with length of 5 is from $f = 0.044$ to $f = 0.164$ if the drop point of the second trough around $f = 0.1$ is not considered.

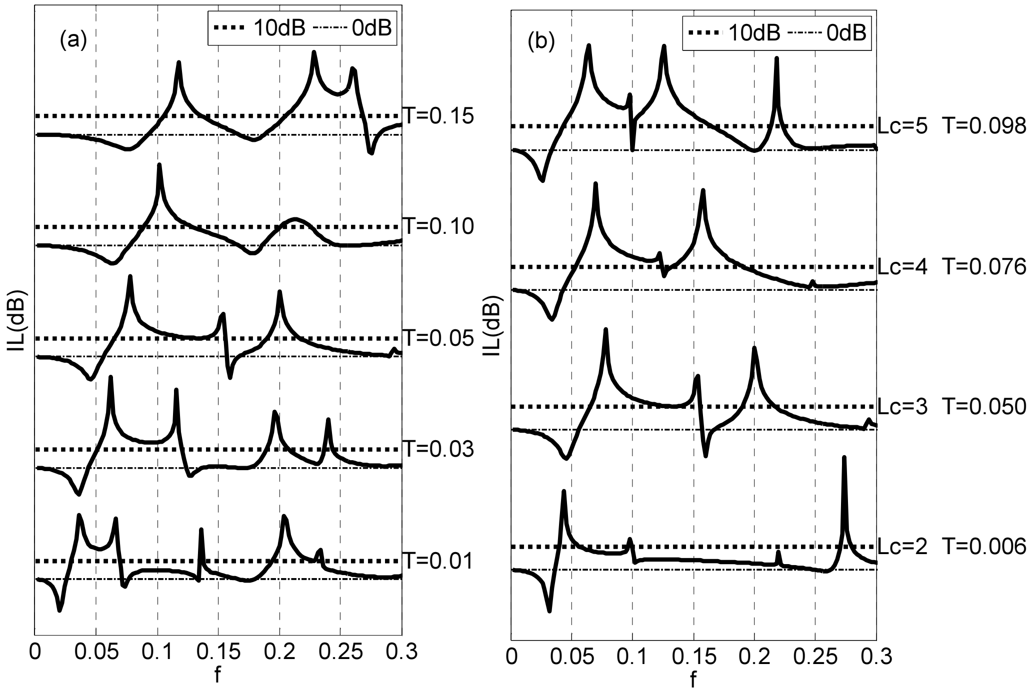


Figure 4.6 Parameter study on the IL performance of the dipole control by the drum silencer (a) The IL spectra with the increment of tension at the length of 3(b) The IL comparison of different membrane length at the optimal tension

#### 4.3.4 Modal impedance

In order to differentiate the physics behind the variations of the spectra, the modal impedance component is calculated by virtue of the decomposition of the fluid loading on the membrane with the help of the modal impedance analysis. Figure 4.7 shows the variation of the structural reactance $L_j$ of the second mode when the physical properties of the structure changes. The open circle is labeled as the zero impedance point for reference. The effects of tension, mass and length of the membrane are depicted in Figure 4.7(a), (b) and (c) respectively. Figure 4.7(a) shows the imaginary part of $L_j$ for the fixed $m = 0.2$ with the variation of tension. It is apparent that there is substantial change of the reactance especially in the very low frequency range $f < 0.1$ when the tension is increased by a small amount. In addition, the impedance tends to be negative and even goes to infinite at the frequencies near DC when there is tension. For the zero tension, the reactance will be positive and becomes zero at DC frequency. Such negative reactance means that the membrane becomes rather stiff with the increase of tension at low frequencies. It also tends to shift to higher frequencies with the increase of tension. This is the reason why the lower limit frequency shown in Figure 4.6(a) also shifts to higher frequencies. Because of the high stiffness property of the membrane, the sound cannot penetrate through the membrane to the cavity within this low frequency range. Therefore, below $f_1$ the sound is radiated to the left side of the duct directly and hence the cancellation of the dipole sound radiation within the membrane region is small and it results in very low IL value.

On the contrary, the effect of the mass ratio on $L_j$ is totally different from that of tension as displayed in Figure 4.7(b). The effect of mass becomes more significant when the frequency is greater than $f = 0.05$ . The massive loading leads the reactance to become positive when it is increased. The line with zero mass is presented by solid line. Based on Figures 4.7(a) and 4.7(b), when $f \leq 0.05$ , the introduction of the membrane probably changes the structural impedance mainly due to the tension instead of the added mass. The membrane becomes stiff due to the high negative value of impedance at very low frequencies and hence the sound radiation from the dipole source cannot penetrate the membrane into the cavity and it results in no sound cancellation inside the cavity. Therefore, the IL spectrum of the drum silencer with small tension is always lower than that of the expansion chamber at such very low frequencies and this is unfavorable for the present study. When $f \geq 0.05$ , the reactance decreases from positive to negative as the tension increases, while it increases from negative to positive with the increasing mass ratio. The noise reduction can benefit from the tradeoff between the two effects of the reactance, thus the IL pattern is close to but higher than that in the simple expansion chamber.

Finally, the structural impedance of the membrane with various lengths and optimal mass ratio is compared in Figure 4.6(c). It is found that the impedance gets close to each other except for the deviation of $L_m = 2$ . With reference to Figure 4.6(4b), the stop-band to achieve the criterion level is extremely narrow at this length. The failure of the broadband performance probably results from the limitation length inside the cavity for the sound cancellation. As for other lengths, there is small deviation of the impedance curves so that the structural impedances of the different membranes at the optimal performance nearly coincide.

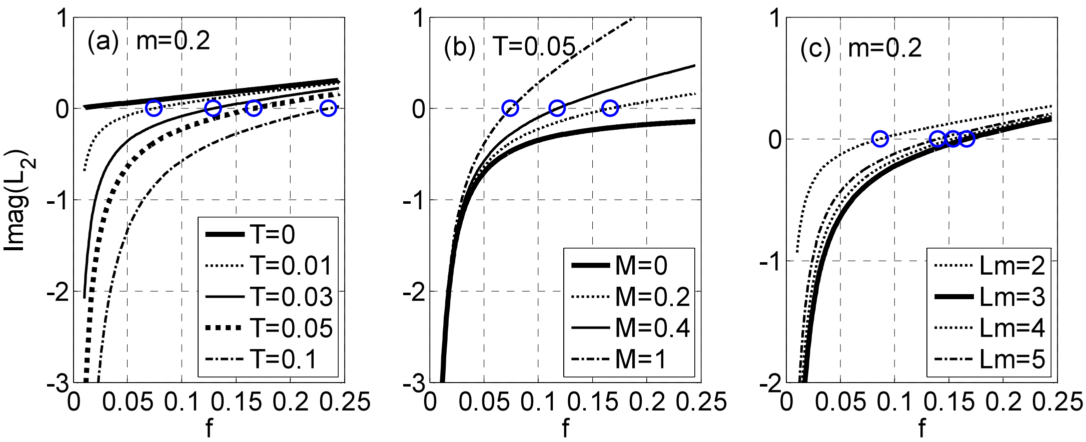


Figure 4.7 Structure impedance comparison of the membrane at different physical properties (a) Structural reactance with the increase of tension (b) Structural reactance as a function of mass ratio (c) Structural reactance of different membrane lengths with the optimal tension

### 4.3.5 The resonance frequency

The components of total impedance of the second mode $Z_{22}$ and fourth mode $Z_{44}$ are to be analyzed for decoupling the important features of such a complicated system. The components of the reactance composed of radiation, cavity reflection and structure are shown in Figures 4.8 (a) and 4.8(b) for the chosen optimal membrane with $m$=0.4 and $T$=0.05. The total reactance of $Z_{22}$ and $Z_{44}$ is shown in Figures 4.8(c) and 4.8(d) respectively. The open circles indicate the zero impedance of the *in vacuo* membrane modes and the total reactance. The structural contribution vanishes at frequencies $f = \frac{j}{2L_c}\sqrt{\frac{T}{m}} = 0.118, 0.236$ for $j = 2,4$ . On the other hand, the reactance diverges at the cavity modes according to the relationship of the cavity length and the wavelength. In the current example, the divergent frequency is about $1/6$ for the first two even modes, thus the corresponding wavelength is twice of the cavity length.

At very low frequencies, it is clear that the high stiffness appears because of the dominance of the structural impedance (thick dashed line) for both vibration modes in Figures 4.8(a) and (b). It is difficult for the membrane to respond and vibrate and for the sound to penetrate into the cavity as well. As frequency increases, the radiation impedance in the main duct (thin line) is prominent and is possible to cancel out the structural contribution. The balance is reached at $f = 0.044$ for the second mode as shown in Figure 4.8(c), where the total impedance disappears and the coupled system resonates. This also corresponds to the strong vibration of the membrane at the second mode as displayed in Figure 4.4(1b). Meanwhile, $|V_4|$ is very small for $f \leq 0.1$ ,

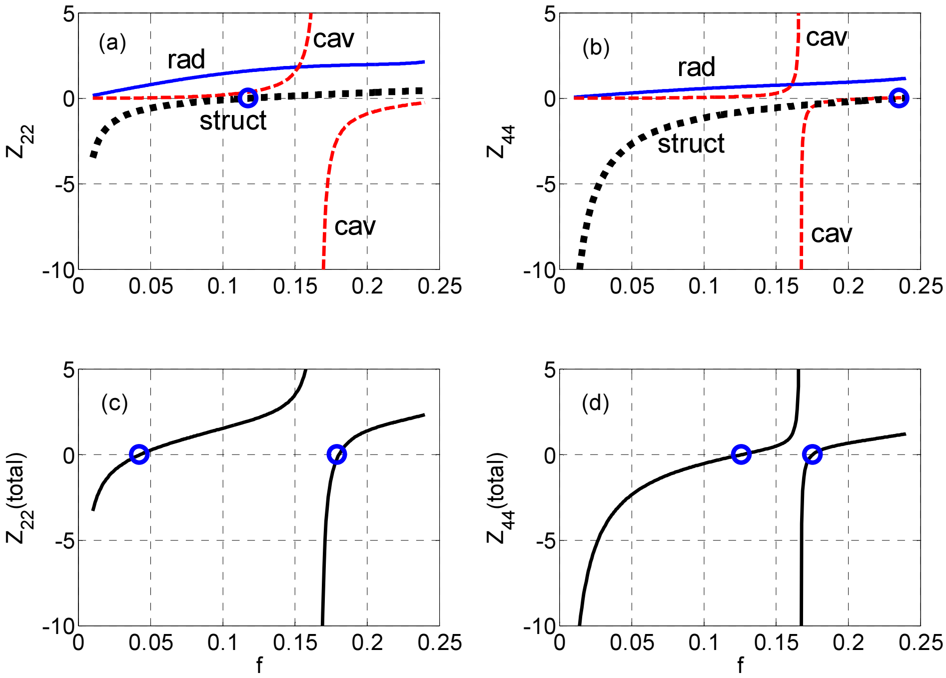


Figure 4.8 Reactance of the second and fourth modes and resonant frequencies. (a) Shows the component variation of the second mode reactance against frequency. The components consist of radiation (solid line), cavity reflection (thin dashed line), and the structural properties (thick dashed line). (b) Exhibits the fourth mode components in the same way. (c) Shows the total reactance of the second mode for which the zero reactance is marked by an open circle. (d) Shows the total reactance of the fourth mode for which the zero reactance is also marked by an open circle

the cross modal coupling between the second and the fourth modes can be ignored. In contrast, the total impedance of the fourth mode approaches zero at $f = 0.13$, which is below the divergence of the cavity mode (thin dashed line). The vibration and the contribution towards the sound radiation at both second and fourth modes match in magnitude near the divergence frequency, see Figures 4.5(3b) and (3d). Concerning the zero structural impedance of the second mode at $f = 0.118$, the cross modal interaction is regarded to be very strong here and is expected to be responsible for the feature of the second peak followed by a trough in the IL spectrum. Besides, the zero points of the membrane's impedance at different tensions as indicated in Figure 4.7(a) roughly correspond to the peak-trough position in IL spectrum as shown in Figure 4.5(a). This serves as another proof for the shift of the abrupt drop.

Beyond the second trough in the IL spectrum, the near zero IL is displayed for both the silencer and the expansion chamber at the similar frequency range of $f = 0.16 \sim 0.18$ as shown in Figure 4.5(a). The reason is mainly due to the divergence of the cavity mode as mentioned above. The cavity becomes very stiff to prohibit the vibration of the membrane and hence the sound cannot penetrate the cavity and no cancellation of the radiated sound from the dipole source.

### 4.3.6 The peak points

In this section, the vibration characteristics at the peak points shown in Figure 4.4(a) and the decompositions of the vibration velocity are to be analyzed. The interference pattern at a frequency point between the two peaks is also selected to illustrate the control features by the membrane. Figure 4.9 shows the response of the membrane at the first peak of $f = 0.072$. The amplitudes of $V_j$, $R_j$ and $R_jV_j$ of the first ten modes are shown in Figure 4.9(a), (b) and (c) respectively. According to Figure 4.9(a), the second mode is obviously dominant and it is totally excited by the dipole source, which is preferable in the current study. Although its amplitude is much larger than that of any other modes， its effectiveness in sound radiation should be lower than that of the first mode. Moreover, the radiation contributions by $R_2V_2$ and $R_4V_4$ are also represented by a vector in the real imaginary space in Figure 4.9(d). The contributions from the second and fourth modes are nearly in phase, but the fourth mode is not effective in radiating sound when comparing the length of the vector. Therefore, the radiation efficiency at this peak only relies on the *in vacuo* second mode of vibration. Figure 4.9(e) shows the membrane vibration distribution over the entire length. An almost perfect second mode shape of membrane vibration is observed. Such phenomenon is also observed at a higher frequency peak of $f = 0.196$ .

Figure 4.10 shows the response of the membrane at the second peak of IL spectrum at $f = 0.142$ . Basically, the fourth mode of vibration appears to be dominant, but it has less radiation capability than the first two modes. With reference of Figure 4.10(d), the radiation contribution in terms of the vector from the second and the fourth modes is almost equal in magnitude. Besides, the interference between these two modes can be observed by virtue of the phase relationship. The vibration shape of the membrane in Figure 4.9(e) displays a distorted fourth mode which is coupled with the second mode and this makes the amplitude enlarged near the center of the membrane.

Figure 4.11 shows the response of the membrane at the peak of IL spectrum at $f = 0.1$. Compared with the vibration at the first two peaks at $f = 0.072$, the contribution of the second mode appears to be diminished while that of the fourth mode increases in Figure 4.11(c). At this frequency, the second mode is generally dominant. As shown in Figure 4.11(d), the modal contribution for sound radiation of fourth mode is comparatively weak. For the resultant response of the membrane, the second mode vibration, although distorted, is also found to be dominant when the velocity distribution of the whole membrane is examined as shown in Figure 4.11(e).

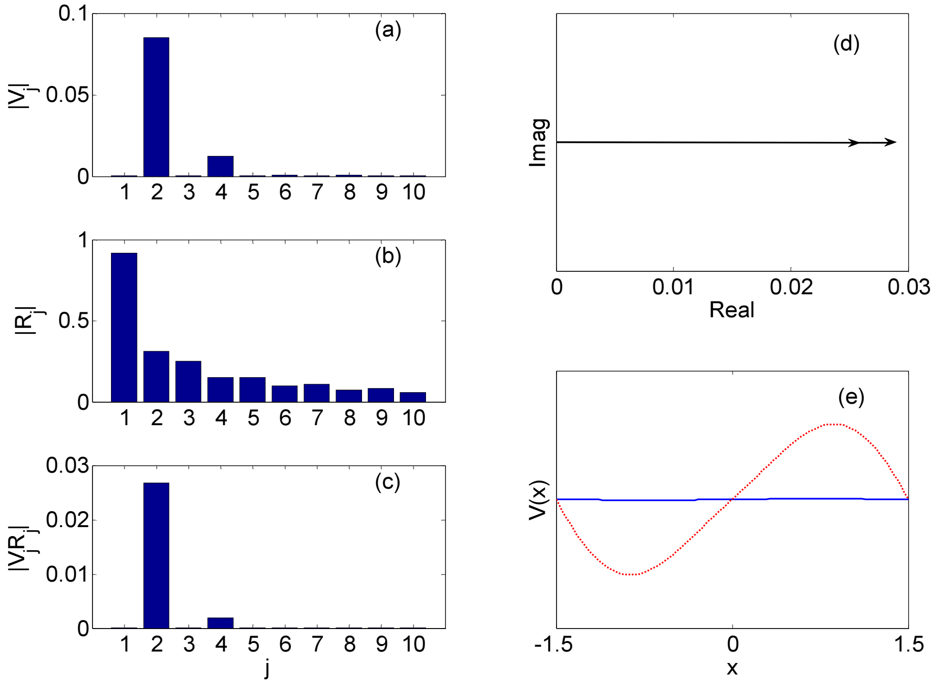


Figure 4. 9 The response of the membrane at the first peak of f=0.072.

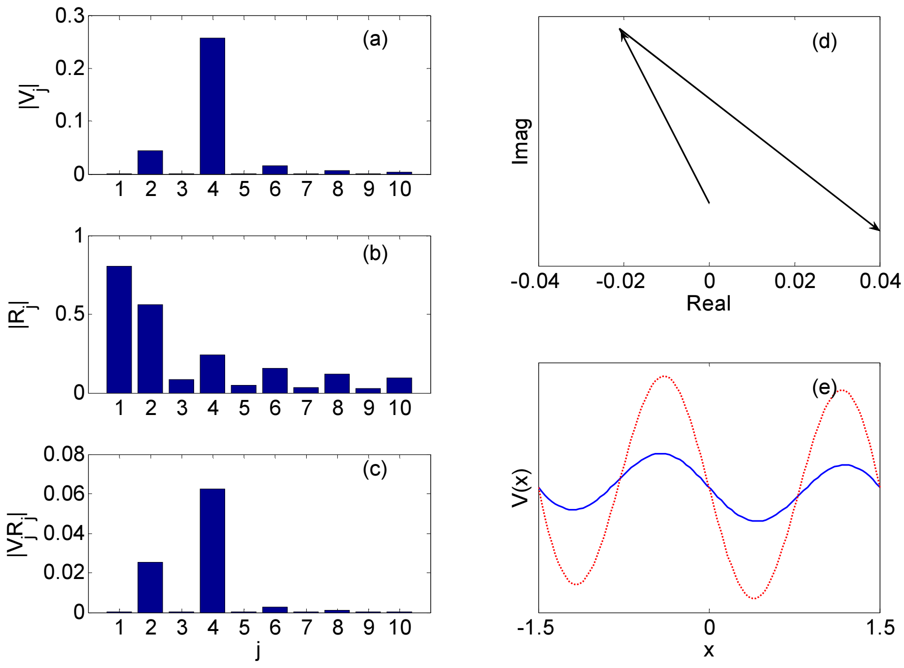


Figure 4.10 The response of the membrane at the second peak f=0.14.

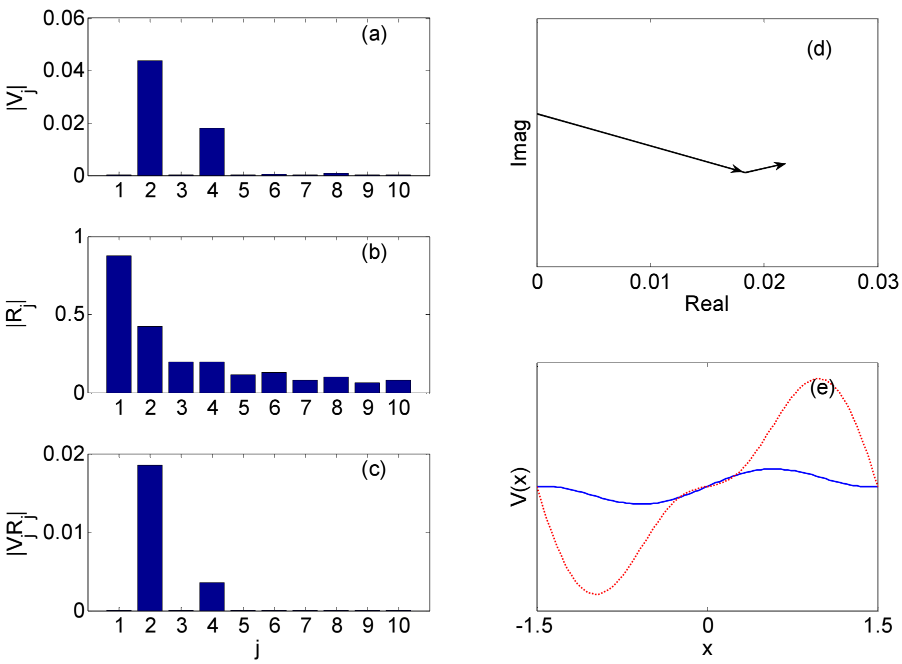


Figure 4.11 The response of the membrane at f=0.1 where the IL can be kept higher than 10 dB.

## 4.4 Conclusions

The full coupling between the dipole sound and cavity backed membrane in a two-dimensional model have been investigated numerically. Although the feature of using the membrane is similar to the previous study (Huang, 2002), the mechanism to reduce the noise is totally different. The method of the noise abatement aims at the control of the sound source rather than the propagation path of the sound. The optimization study is carried out to find the effects of several parameters, such as the tension, mass ratio, on the performance of the noise reduction. The fluid loading exerting on the membrane and the corresponding vibration response are also investigated in order to explain the IL pattern. Conclusions can be drawn as below:

(1) With an appropriate low tension on the membrane, the IL of the silencer can be achieved to be higher than 10dB over a frequency range with a stop-band $r_f = 2.15$ which is more than one octave. In other words, the noise reduction can outperform that of a simple expansion chamber by at least 5dB on average in the frequency range of interest for the particular configuration studied here. The response of the membrane induced by the dipole source indicates the dependence on the control ability of the second mode and fourth mode of the membrane vibration. Thus it can be said that the primary feature of the even modes is very crucial on the noise reduction.

(2) IL values appear to be very low at DC frequencies for the silencer, which is the

most important difference compared with that for the expansion chamber. The detailed analysis demonstrates that the structure becomes stiffer due to the tension when the frequency approaches the DC frequency. Consequently, the deformation of the membrane is structurally hard and will not be easily excited to vibrate well by the radiated sound from the dipole source. Besides, the stiffness also prohibits the penetration of the sound into the cavity. Most of the radiated sound from the source propagates towards both upstream and downstream directly; hence the IL is expected to be too low.

(3) The two negative troughs occurred just outside the stop-band region in the IL spectrum. It implies that there is the strong sound radiation. However, the induced vibration patterns of the membrane therein are not the same. At the low frequency, the second mode vibration solely contributes to the sound radiation. In contrast, the cross modal interaction between the second and the fourth mode leads to the high radiation effectiveness at the second trough. Another important feature is the drastic drop of the IL following the second peak in the IL spectrum. This happens since the structural impedance vanished immediately followed by the disappearance of the system impedance. Beyond the second trough, the near zero IL displays for both the silencer and the expansion chamber, which is mainly due to the divergence of the cavity mode.

(4) In general, the membrane vibration involves the coupling effect of the even modes

gradually between the two IL peaks in the IL spectrum. The dominance of the sound radiation seems to be shifted from the contribution of the second mode to the fourth mode in the current model. The compromise between the radiation decrease of $\gamma_2$ and the increase of $\gamma_4$ is believed to control and sustain the high IL over the frequency range between the two IL peaks.

# Chapter 5 Noise abatement of ducted axial flow fan by the dipole control

## 5.1 Introduction

The current study mainly seeks to mitigate the sound radiation by the ducted axial flow fan. In Chapter 4, the use of the tensioned membrane in the dipole source control has been proved to be very promising in the duct system. To do the practical study, this chapter will firstly demonstrate that when proper modifications are made, the fan noise can be modeled as a distributed source which is very close to the ideal dipole source. The effect of non compactness is negligible because of near zero spinning pressure mode of the leading radiation (Huang,2005). The advantage of such strategy lies in the little requirement of source prediction for the complicated situation of the fan.

As the dipole source by the fan is distributed circumferentially in the fan rotation plane, the 2D finite element model in Chapter 4 cannot describe the ducted fan system precisely. In this chapter, the numerical modeling is extended to a 3D configuration, which represents a realistic ducted axial flow fan system. Experimental studies are also conducted to validate the 3D numerical models. The flow speed generated by the fan is limited to be low in the ventilation system, say below 20m/s. A specially-designed test rig is constructed to eliminate the lateral gap along the edge of the membrane for the cross flow so that the flow induced vibration is avoided.

In what follows, to do the practical study, Sec. 5.2 will firstly demonstrate that when proper modifications are made, the fan noise can be modeled as a distributed source which is very close to the ideal dipole source. In Sec. 5.3, the theoretical background is introduced very briefly, and the simulation model is established to predict the insertion loss of the fan noise in the infinite length duct and a finite duct length with the exit boundary condition of the open end, respectively. The optimization of the silencer's performance is executed and the numerical results are presented in Sec.5.4 with the vibration modes of the membrane. Sec. 5.5 describes the experimental validation for the insertion loss of the fan noise in the real configuration. This includes the performance of both the loudspeaker and fan as the dipole source. Finally, the conclusions will be drawn in Sec. 5.6.

## 5.2 Dipole characteristics of the sample fan noise

We focus on reducing tonal noise radiation of a cooling fan at the first blade passing frequency (BPF) by using a reactive method of controlling the noise source. Generally speaking, the radiated noise by the fan or any machine with moving blades consists of monopole from the blade motion, dipole from unsteady forces on blades, and quadrupole emanating from the turbulent jets. The dipole component arising from the fluctuations is most important compared with the other two when the fan is at low speed. In this regard, the original fan is properly modified to achieve the maximum dipole noise by eradicating the other noise components for the experimental validation later.

To analyze the dipole feature of the fan noise, the basic theory and mechanism to quantify the noise components is examined herein. The axial flow cooling fan used here is very common in the market, and it is comprised of a rotor with B blades and S motor struts. The dominant noise source of the fan comes from the unsteady lift force on the rotor blades, which consists of two components: thrust force $T_f$ in the flow direction, drag $D_f$ in the circumferential direction against the rotation. The two components are usually induced from two kinds of aerodynamic interactions, respectively. One is between the rotor blades and downstream struts and the other is between the distorted inlet flow by the sharp edges of the incomplete bellmouth and the rotor. The unsteady force distribution on the blade surface can be expressed by the summation of many isolated point forces with a thrust and drag component. The amplitude of the far field acoustic pressure due to the rotation at the frequency of the $m^{th}$ harmonic of the fundamental BPF is given below (Lowson, 1970):

$$c_{m_f B}^{(rotor)} = \frac{i m_f \omega B^2 S}{2\pi c_0 r_0} \sum_{k_f=-\infty}^{k_f=\infty} i^{-\nu} \left( T_{kS}^{(rotor)} \cos\phi - \frac{\nu}{m_f BM} D_{kS}^{(rotor)} \right) \times J_\nu (m_f BM \sin\phi),$$
$$\nu = m_f B - k_f S, \tag{5.1}$$

where $B$ and $S$ are the rotor blade and strut numbers, respectively; $M = \omega r_s / c_0$ is the rotational March number of point source at radius $r_s$ where the interaction occurs; $\nu$ is regarded as the differential of two frequency index, one is the index of BPF harmonics $m_f B$ and the other the index of source frequency, where $m_f$ and $k_f$ is any integer. $T_{kS}^{(rotor)}$ and $D_{kS}^{(rotor)}$ are the amplitude of the unsteady force components of thrust $T_f$ and Drag $D_f$ on the rotor blades, $c_0$ is the speed of sound and $\phi$ is the angular position of the first strut relative to the observer on the horizontal plane .

The most important parameter is frequency index differential $\nu = m_f B - k_f S$ , or the index of spinning pressure mode. Here, the observed noise of frequency index is $m_f B$ since other frequency components are cancelled among themselves when all the rotor blades radiate sound with a fixed phase relation determined by the rotation. The source frequency index is $k_f S$ because of the blockage by the struts during one cycle of rotation. The amount of sound power radiation and the appearance of the acoustic directivity depend highly much on this index value. On one hand, the thrust noise radiates rather loudly when the two indices coincide as $\nu = m_f B - k_f S = 0$ . Under this condition, the noise radiated by all blade strut interactions simply add up, and the resultant becomes a simple dipole in the axial direction. In addition, the drag noise will vanish, as can be seen by the numerator $\nu$ of the drag term in Eq. (5.1). On the other hand, for the mismatch of the two frequency indices $\nu = m_f B - k_f S \neq 0$ , another factor of the motion of the source , namely the Doppler effect , can be utilized to characterize the noise pattern by the Bessel function $J_v(z)$ , where $z = m_f BM \sin\phi$ . In fact, the argument of the Bessel function $BM$ is usually less than 0.2 for the small cooling fan operating at low speeds. As a consequence, $|z| \le 1$ is obtained under moderate high frequency and $J_v$ can be approximated through Taylor expansions:

$$J_0(z) \approx 1 - \frac{z^2}{4} \; ; J_1(z) \approx \frac{z}{2} \; ; J_{|v|>1}(z) \approx \frac{1}{\sqrt{2\pi v}} (\frac{ze}{2v})^v \quad . \tag{5.2}$$

Referring to Eq.(1), it can be seen that in order to obtain the ideal feature of the dipole in the axial direction for the ducted fan, the most effective and simplest way is to make the frequency index difference to become zero. Then the unsteady force component of $T_f$ radiates the noise most efficiently and $D_f$ vanishes. The effect of non compactness is considered to be very small because of near zero spinning pressure mode of the leading radiation (Huang, 2003). Such strategy also facilitates the prediction of the dipole source.

As far as the original commercial fan in the market is concerned, it usually has 7 blades and 4 struts. The existing fan should be modified with 7 new struts such that $\nu = 0$ (see Figure 5.1(a)) can be obtained. In order to simulate the original configuration of fan, the outer frame is also attached shown in Figure 5.1(b) so that the confinement effect of the casing is included. The noise spectra of the modified fan at different rotational speeds are measured. As shown in the spectrum in Figure 5.1(c)-(g), the first BPF is shifted to higher frequency when the rotational speed is increased. It is very important that the first BPF mainly lies in the frequency range of 250Hz to 500 Hz. In this study, we will focus on the fan noise attenuation in this specific range, and the total noise reduction in the broadband frequency range of interest is the main concern during the simulation model.

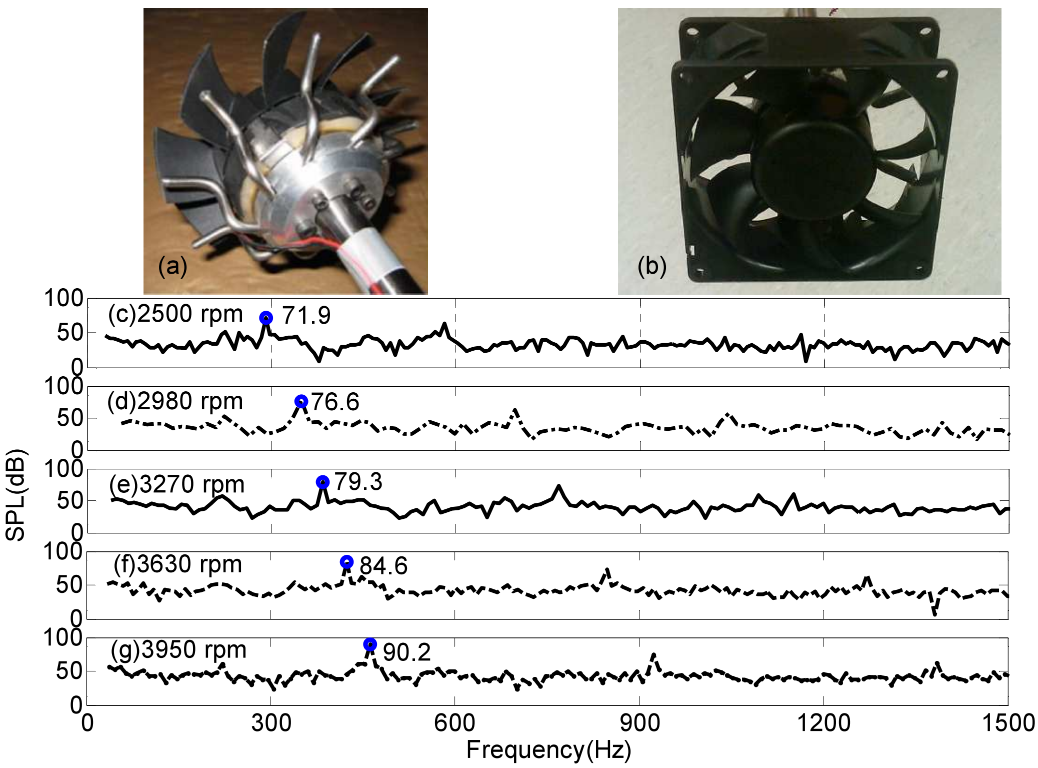


Figure 5.1 Noise spectra of the modified commercial cooling fan. (a) The back view of the AVC cooling fan with the 7 blades and 7 modified struts (b)The front view of the fan with the original casing (c)-(g) The spectra comparison of the fan noise in the axial direction for different rotational speeds

## 5.3 The 3D finite element modeling

Figure 5.2 shows the 3D configuration of the fan with the noise control by the four membrane silencer. It can be divided into three parts: the main duct, the cavity and the membrane. For the duct, there are upstream and downstream sides with the same cross section of $h \times h$, and a length of $L_{up}$ and $L_d$, respectively. For the cavity, it is in the cylindrical shape with radius R and length $L_m$, and the inner surfaces are covered by four tensioned membranes (only the upper one shown here as the blue surface for a clear illustration of the inside). Note that it is very difficult to install four individual cavities outside the four membranes for the rectangular duct in reality. Therefore, the complicated 3D model is constructed with a circular cavity outside for convenience and more accurate calculation.

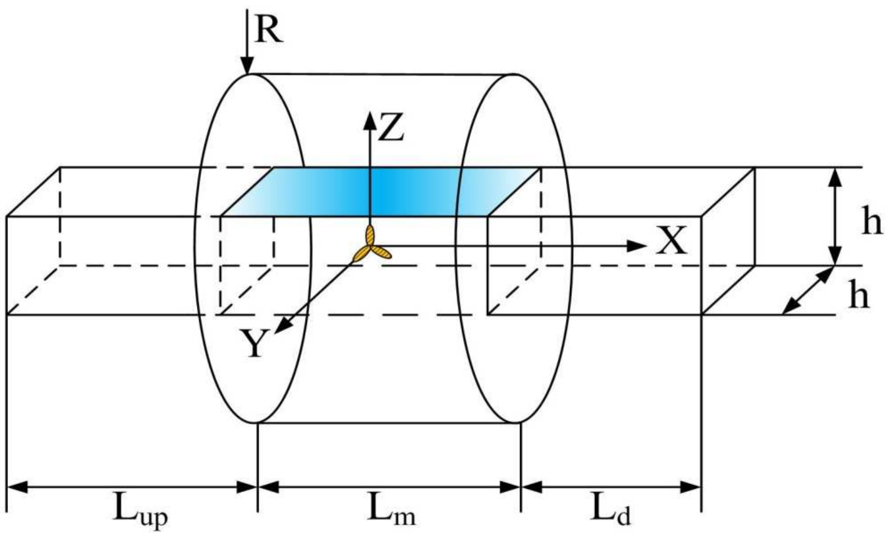


Figure 5.2 Configuration of the 3D simulation model of axial fan inside an expansion chamber covered by four tensioned membranes

The axial flow fan is regarded as a pure dipole source and placed at the middle along the axial direction. The membranes are simply supported at both the leading and trailing edges, and the tension is applied along the axial direction. The two lateral edges of each membrane can be kept to be free for vibration. Further numerical study indicates that there is little difference on the result of the noise reduction performance when the lateral edges are fixed but without tension in the spanwise direction. In the current calculation, the fixed lateral edges are adopted since they can prohibit the acoustical leakage in the practical configuration. The simulation process is performed with the aid of the commercial FEM software Comsol Multiphysics ®, which is an extended package of MatLab ® to solve the problems for multiphysics modeling.

The acoustical field of the entire domain satisfies the inhomogeneous Helmholtz equation:

$$\nabla \cdot (-(\nabla p - q)) - k^2 p = Q, \tag{5.3}$$

where $q$ and $Q$ respectively refer to the dipole source and monopole source, which are optional.

The boundary condition on the hard walls is well known,

$$\frac{\partial p}{\partial n} = 0 , \tag{5.4}$$

where $n$ is the local outward normal direction .

Generally, the boundary condition of the duct exit with terminating impedance $Z$ can be expressed in the following form,

$$n \bullet (\nabla p - q) + \frac{i\omega p}{Z} = 0 \ . \tag{5.5}$$

The terminating impedance for the realistic radiation condition is usually complex. The real part (radiation resistance) represents the energy radiated away from the open end in the form of sound waves, and the imaginary part (radiation reactance) represents the mass loading of the air just outside the open end. For unflanged and flanged open ends, respectively, the empirical formula of the radiation impedance of the circular pipe (Levine,1947; Atig,2004) is

$$Z = \begin{cases} \frac{1}{4}(ka)^2 + i0.61ka \\ \frac{1}{2}(ka)^2 + i\frac{8}{3\pi}ka \end{cases} , \tag{5.6}$$

where $a$ is the radius of the pipe. When a rectangular duct of cross section $h \times h$ is used, $a$ is assumed to be $\sqrt{h \times h / \pi}$ based on the area equivalence.

Specially, for the outgoing wave condition of a plane wave,

$$Z = 1 \ . \tag{5.7}$$

The governing equation for the lower membrane vibration is

$$m\frac{\partial^2\eta}{\partial t^2}-T(\frac{\partial^2\eta}{\partial x^2}+\frac{\partial^2\eta}{\partial y^2})+(p_+-p_-)=0 \tag{5.8}$$

where $\eta$ is the membrane displacement, $(p_+-p_-)$ is the fluid loading on the membrane, $m$ is the mass ratio of the membrane to the air and $T$ is the tensile force.

For harmonic wave excitation on the membrane, the vibration $V(x,y)$ is expanded into the *in vacuo* modes of the simply supported membrane expressed by $\varphi_{jl}(x,y)$ ,

$$\varphi_{jl}(x,y)=\sin(\frac{j\pi x}{L_m})\sin(\frac{l\pi y}{h}) \quad , \tag{5.9}$$

and the vibration can be stated as

$$V(x,y)=\sum_{j=1}^{\infty}\sum_{l=1}^{\infty}V_{jl}\varphi_{jl}(x,y) \quad , \tag{5.10}$$

then the amplitude of the vibration mode (*j, l*) can be obtained from the following expression

$$V_{jl}=\frac{4}{L_m h}\int_0^h dy\int_0^{L_m}V(x,y)\varphi_{jl}(x,y)dx \quad . \tag{5.11}$$

The index IL is adopted to assess the performance of the silencer on the fan noise reduction. It is defined as the loss power resulting from the insertion of the silencer with tensioned membranes. To obtain the best performance of the silencer, the frequency ratio $r = f_2 / f_1$ has been used to find the widest stop-band performance of the silencer in Chapter 4, where $f_1$ and $f_2$ are two consecutive frequencies between which IL is above a criterion value. However, the ratio can be fairly large for a very low $f_1$, thus it may be invalid if using the large value to stand for the broad bandwidth. The total transmission loss $TL_t$ was introduced with a low frequency based weighting function as the new cost function (Choy, 2009). Such function eliminated the undesirable discontinuity of the attenuation.

In the present study, we place an emphasis on the noise reduction in a specified frequency range of 250 Hz to 500Hz based on the measured spectra of the axial flow fan. Thus, the total insertion loss $IL_t$ is used during the optimization procedure, but the coefficient of the weighting function is omitted for simplification since the frequency range is fixed. The $IL_t$, which is greatly dependent on the chosen frequency range, is defined as

$$IL_t = 10\log_{10}\left|\frac{\sum p_{\mathrm{S}tr}^2 \Delta f}{\sum p_{\mathrm{Exp}}^2 \Delta f}\right|, \tag{5.12}$$

where $\Delta f$ is the frequency step and 'Str' and 'Exp' denote the straight duct and the silencer consisting of the membrane and expansion chamber, respectively. Note that the total sound energy before the silencer is inserted should take account into the noise abatement effect of an open end reflection when the performance of a real configuration is predicted.

In all numerical discussions, the parameters are normalized by three basic quantities, the fluid density $\rho_0^*$ , the duct height $h^*$ and speed of sound $c_0^*$ . For the sake of comparative study with the experiments, two relevant parameters emerge,

$$f = \frac{f^* h^*}{c_0^*}, \quad T = \frac{T^*}{h^* \rho_0^* (c_0^*)^2}, \tag{5.13}$$

where $f^*$ and $T^*$ are, respectively, the dimensional frequency and tensile force applied. In the real configuration used later, the duct height $h^*$ is 0.1m.

## 5.4 Silencer performance and its optimization

The performance of noise reduction on a dipole source by the silencer with tensioned membranes is investigated numerically. The default configuration comprises a membrane with length $L_m = 3$ and a cavity with radius $R = 2$ when the dimensionless duct height is unity. The optimal performance of the silencer is obtained by searching for the optimal tension when $IL_t$ is maximum for a specified mass ratio of the membrane.

In the first part, the main duct with an infinite length is studied. Figure 5.3(a) compares the overall IL of the present silencer (thick dash dot line) with a pure expansion chamber, which is calculated from the finite element method(dashed line) and a simplified plane wave theory(solid line) , respectively. The approximation from the plane wave theory on the IL characteristics due to the insertion of the expansion chamber was derived in detail by Huang (2010), and the final expression is given as follows.

$$\frac{W_1}{W}=\begin{cases}\alpha^2, kL_m=2n\pi \\ 1, kL_m=(2n+1)\pi \\ (1+\alpha^2)/2, kL_m=(2n+1)\pi/2\end{cases} \quad \text{, where } n \text{ is any integer.} \tag{5.14}$$

Then the insertion loss can be found by $10\log_{10}(W_1/W)$ in dB, and the spectrum pattern is dependent on the relationship between the chamber length and the wavelength. The peak performance is found at zero frequency (DC frequency) when the chamber is exactly a multiple of a full wavelength. No change is found when the chamber is an odd multiple of half wavelength. Intermediate results appear when the chamber length is any odd multiples of a quarter wavelength.

For the present configuration, as indicated in Figure 5.3(a), the *IL* for the expansion chamber from the plane wave theory and the finite element method both display the peak performance at the DC frequency. The peak value can achieve about 20 dB, which is conspicuous for such a small configuration. For the current silencer with tensioned membranes, the optimal tension is found to be $T=0.06$ , the $IL$ is near zero at the very low frequency. However, for the frequency of interest the noise reduction can reach 10dB everywhere from $f_1 = 245Hz$ to $f_2 = 500Hz$ , with a bandwidth over one octave. In particular, the averaged noise reduction in the frequency range of 300 Hz to 500Hz is about 30dB, which is 10 dB higher than that obtained by the expansion chamber. Another main feature is that all the IL value approaches zero at around $f = 570Hz$ , the corresponding wavelength is 0.6 m which is twice of the default chamber length. In general, the trend here is similar to the results discussed in the two dimensional model. Such phenomenon is elucidated mainly by the modal impedance components in the coupled system. At low frequencies, apart from the high cavity stiffness, the structural stiffness of the membrane is increased tremendously when there is tension. This will prohibit the sound from penetrating the membrane to the cavity. As the frequency increases, the structural impedance will be changed from negative value to near zero. As a result, more radiated sound from the dipole can penetrate the membrane to the cavity and the cancellation occurs inside the cavity due to the reverberant effect. The dip near $f = 570Hz$ mostly results from the divergence of the cavity modes as indicated in 2D model. Figure 5.3(b) and Figure 5.3(c) display the variation of the $T_{opt}$ and $IL_t$ with different mass ratios of the membrane $m$ during the optimization procedure, respectively. It is found that $T_{opt}$ increases with the increment of $m$ , and the maximum $IL_t$ is obtained when the mass ratio $m = 0.6$ is achieved. The characteristic of the linear increase of $T_{opt}$ is the same as the result analyzed in the

2D case, but the maximum $IL_t$ occurs at a different mass ratio. It is known that the resonant frequency of a tensioned membrane is shifted towards the low frequency with increasing $m$ but towards high frequency with increment of $T$. For the default configuration, this optimal result reflects a delicate coupling between the membrane dynamic and the sound field in the frequency range of interest.

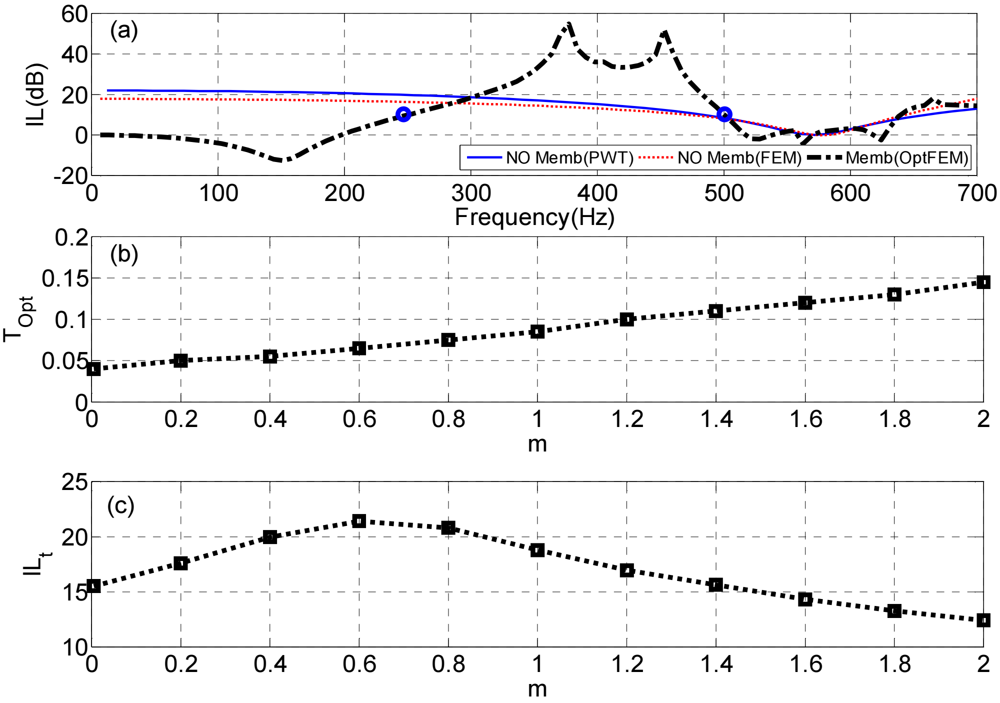


Figure 5.3 Performance optimization of the IL for the fan noise suppression by the silencer with tensioned membranes (a) Comparison of the IL performance of the present model (thick solid dash curve) with the chamber only, the results of the chamber model are calculated by using plane wave theory approximation (solid curve ) and 3D FEM simulation(dash curve) (b) Dimensionless optimal tension against the mass ratio of the membrane (c) Change of $IL_t$ as a function of the mass ratio

Figure 5.4(a) depicts the insertion loss *IL* while Figure 5.4(b) shows the corresponding root mean square vibration velocity of the membrane $V_{rms}$. As shown in Figure 5.4(a), the peaks of IL are labeled by open squares while the trough points are marked by open circles. The corresponding peak of vibration points are also indicated by the same symbols in the spectrum. Two dip frequencies of $f = 157.8Hz$ and $f = 548.8Hz$ in the spectrum are exactly those peaks of the vibration. The subfigures in the left column of the lower part in Figure 5.4 show the vibration velocity distribution at the peak and trough frequencies individually in the growth sequence. Meanwhile, the vibration is decomposed into the first *in vacuo* ten axial modes of $j = 1 \sim 10, l = 1$ , and the amplitude contribution of each mode is illustrated in the subfigure in the right hand side of Figure 5.4. It can be observed that (1) the amplitudes of the vibration velocity at the trough points in Figures 5.4(c) and (i) are much larger than those at the peak frequencies in Figures 5.4(e) and (g). This means that the vibration is strong to radiate the sound to upstream and downstream of the duct; (2) although the 3D effect is observed at the lateral edges of the membrane because of the fixed boundary condition, the first two even modes dominate the vibration instead of the odd modes, which is the reflection of the dipole characteristics; (3) at low frequency, the amplitude component of vibration mainly consists of the second mode pattern. As the frequency increases, the coupling effect of the second mode with the fourth mode becomes more dominant. In summary, the performance on

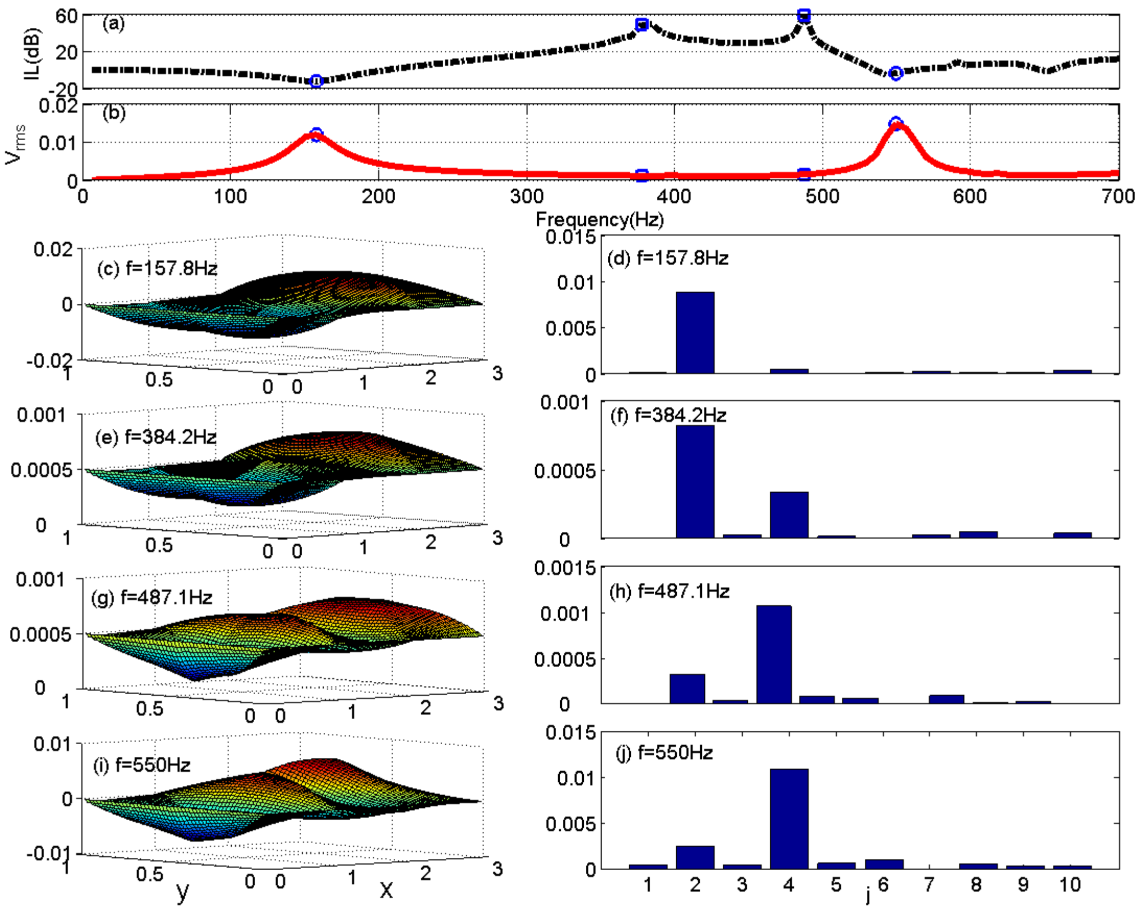


Figure 5.4 The response of the cavity backed, side branch membrane with $L_m = 3, T = 0.065, m = 0.6$ (a) System IL for reference (b) Membrane Vibration Velocity ($V_{rms}$ ,relative scale) (c) Velocity distribution on the membrane at the first IL trough of $f = 157.8Hz$ in the spectrum (d) Modal decomposition of the instantaneous vibration for the first IL trough (e) Velocity distribution at the first IL peak of $f = 384.2Hz$ (f) Modal decomposition for the first peak of IL (g) Velocity distribution at the second IL peak of $f = 487.1Hz$ (h) Modal decomposition for the second IL peak (h) Velocity distribution at the second IL trough of $f = 548.8Hz$ (i) Modal decomposition for the second IL trough

the noise abatement by using the control of the dipole noise source directly depends on the sound radiation of the membrane vibration. The analysis of the modal radiation contribution demonstrates the strong radiation ability at the vibration peaks. The radiation is determined by the interactions between the sound and the membrane in terms of the structural properties. In addition, the system resonance is not necessarily good for the noise reduction because of the strong radiation ability towards outside.

In the second part, to assess the performance of the silencer in practice, the IL is recalculated when the empirical expression (cf. Eq. (5.6)) of the real impedance for the unflanged open end of the finite duct is imposed as the boundary conditions of the duct exit. The dimensionless length of the upstream and downstream ducts is 6.5, which is also to be used in the experiments later. For the membrane with a fixed mass ratio of $m = 0.6$ , the variation of the total insertion loss $IL_t$ with the tension is depicted in Figure 5.5(a). The maximum $IL_t$ of 28dB denoted by the open circle is achieved at a very low tension. The effect of the tension on the $IL$ spectrum is cascaded in Figure 5.5(b), in which the dashed straight line stands for a noise reduction of 10dB for reference. With the optimal tension, the desirable $IL$ can reach at least 10 dB in the frequency range of 280 Hz to 520 Hz, which covers the different blade passing frequencies in Sec. 5.2. As the tension increases, the frequency range in which the considerable noise abatement appears is shifted towards high frequencies. This is attributed to the change of structural impedance at different tensions. In addition, the $IL$ patterns at high frequencies for all tensions are similar, which means the tension effect is weak at $f > 700Hz$ . Concerning the non existence of the frequency shift therein, the potential reason for such behavior is reflection effect at the exit of ducts.

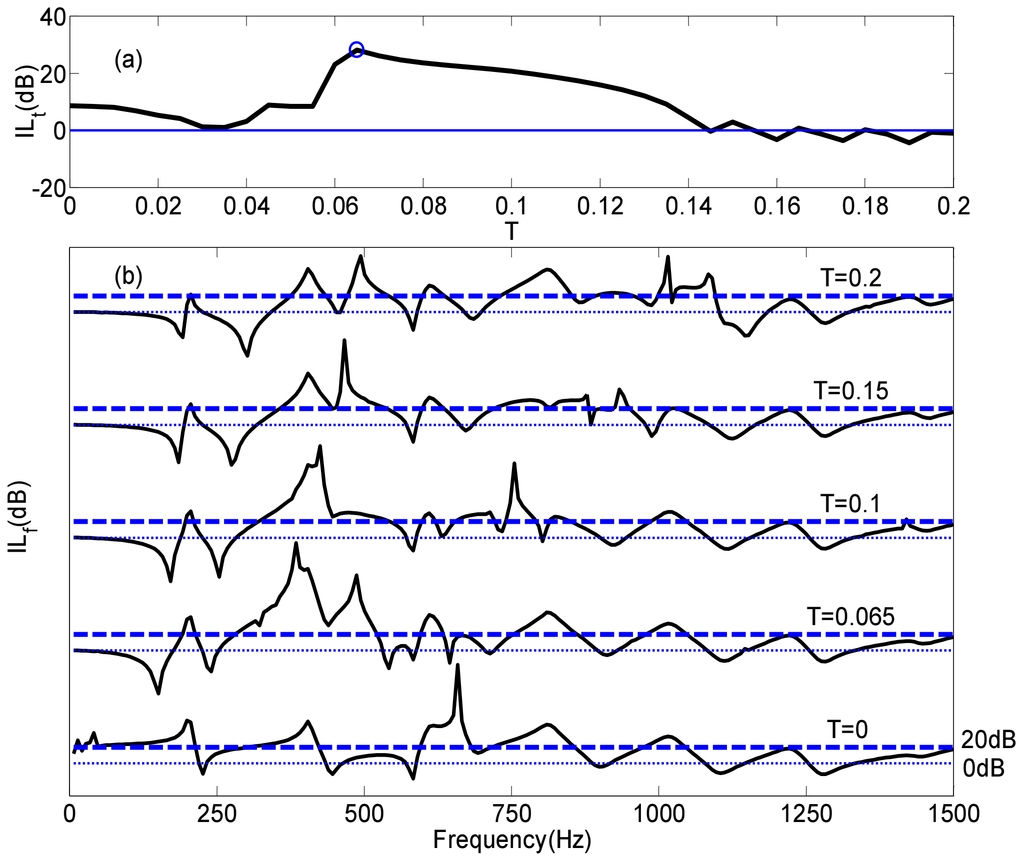


Figure 5.5 Insertion loss of the silencer with a real open end impedance (a)The total insertion loss $IL_t$ as a function of $T$ (b) Comparison of the $IL$ spectra for different tensions

## 5.5 Experimental validation

The main objective of the experimental study is to verify the simulation model established and demonstrate the feasibility of the axial flow fan noise reduction in practice. Two steps are carried out in the current configuration. Firstly, a small loudspeaker of 75 mm in diameter is utilized to simulate the dipole sound radiation. Secondly, a commercially available axial flow cooling fan is adopted for checking its feasibility in the real application. The effect of the impedance at the exit is also considered. The open end condition is applied in the current situation. As shown below, the description of the experimental configuration is based on the latter test since it is simply a replacement of the fan by the loudspeaker.

### 5.5.1 Experimental rig

The experimental set up is illustrated in Figure 5.6. The rectangular duct wall is made of 15 mm thick acrylic and is considered to be acoustically rigid. The cross section of the main duct is $100mm \times 100mm$ . The first cut on frequency in the rigid duct is about 1700 Hz which is much higher than the upper limit of the measured frequency range. The outside circular cavity has a radius of 200mm and the length was 300mm, which is the same as the membrane length. When the chamber is sandwiched in the middle of the whole duct, the upstream and downstream segments are 650mm long. The inner surfaces of the cavity are covered by four membranes tensioned along the axial direction. The membrane is made of stainless steel from Precision Brand®, and has a dimension of 300mm long, 100mm wide and 0.025mm thick. The density is $7.8g/cm^3$ and the Young's modulus is $193GPa$ .

The leading edge of the membrane is simply fixed and the trailing edge is stretched and attached to a moveable tensile machine, for which the design details are given in (Choy and Huang, 2002). The tensile force applied is calculated as $T^* = A\,E\varepsilon$, where $T^*$ is the dimensional tension, $A$ is the cross section of the membrane , $E$ is the Young's modulus and the strain $\varepsilon$ is measured by virtue of a strain gauge glued to the surface of the membrane. The strain gauge type is FLA-3-11-1Lt, which can compensate the temperature change of the membrane during the vibration. The mass ratio of membrane is approximated as $m = M^*/(\rho_0^* h^*) = 1.4$ , and used in the numerical prediction.

To eliminate the flow and acoustic leakage, the lateral edges of every two membranes are covered with a small flat plate of L shape so that the effective width of the membrane becomes 98mm. Then, the lateral edges are entirely glued to the small plates of L shape without any stress in the span-wise direction. It is believed that such little reduction in width has little influence on the performance in the experiment. In addition, the flow velocity measured by traversing a hot wire probe across the inlet section of the duct suggests that the average flow velocity generated is lower than

6m/s. Therefore, both acoustic and cross flow leakage through the gaps is very weak.

As shown in Figure 5.6, the radiated noise is measured both at 20cm upstream and downstream of the open end symmetrically, and the microphone position is offset by 3cm from the center line with a deviated angle of $\theta = 30°$ from the near-side duct opening plane . The offset distance is far enough to satisfy the inverse square law . One pair of 1/2-in. microphones of B&K type 4189 are used and supported by Nexus Conditioning Amplifier type 2693. The maximum flow speed generated by the fan is 5.6m/s in the duct and 2.5m/s at the exit measurement point of the microphone. When using windscreen, such small effect of the noise can be neglected. The windscreen effect was investigated by T.D. et al(2005) and Frede(1966)，the results indicated that when the flow speed is below 9m/s for B&K microphones , good signal to noise level is obtained. Besides, the angle of $30°$ can eliminate the flange effect and reduce the flow effect. The noise radiation of sinusoidal signal is simulated by a loudspeaker connected to the Function Generator Hioki 7075 via a power amplifier (B&K Type 2716C), while the fan is controlled by a regulated power supply. Windscreen is also used during the fan noise measurement for the sake of the flow effect. The signals from the microphones are acquired through AD converter (NI DAQ Card 6062E). The process is controlled by a Matlab® program and the measured frequency ranges from 110Hz to 1500Hz with an increment of 10Hz for the loudspeaker test.

The difficulty and concept of the modification for the simulation of a perfect dipole source by the real fan in the axial direction (as shown in Figure 5.1) is revealed in Section 5.2. The fan rotor has a diameter of 82.5mm and the outside frame has a dimension of $92mm \times 92mm \times 38mm$ . The fan assembly is held as a cantilever by a very rigid cylinder, as shown in Figure 5.1(a), the position of the fan is adjustable along the axial direction and the other end of the cylinder is clamped. The sound radiation from the source placed at the center of the straight duct (or silencer) is measured at the exits of both the upstream and downstream as $p_{up}$ and $p_{dn}$ by two microphones at the given points outside the duct symmetrically. Besides, the sound radiated from one near open end of the duct can reach the microphone located on the other far side, but such cross influence is assumed to be very small.

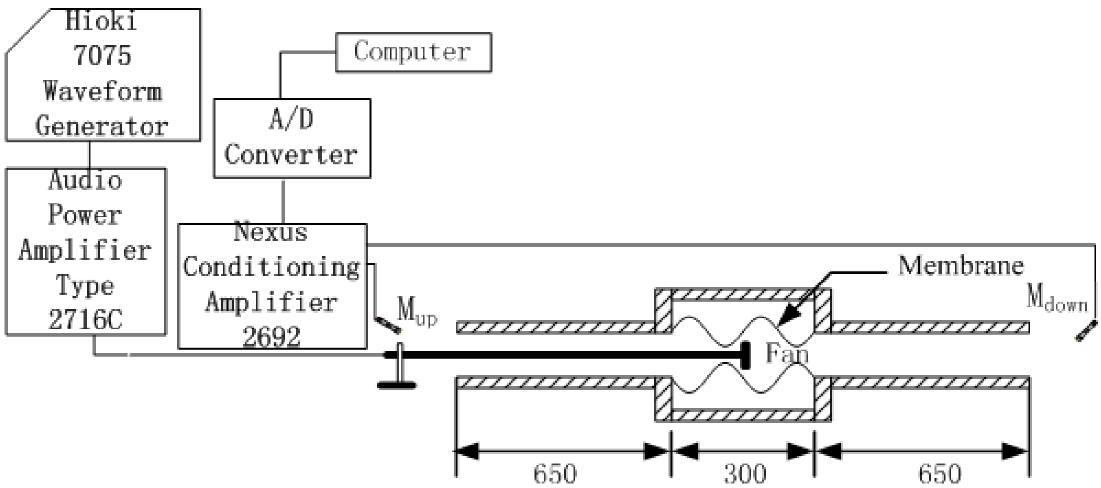


Figure 5.6 The experimental configuration with two microphones at the two exits of the duct

### 5.5.2 Signal processing

In the experiment, the main index $IL$ to quantify the performance of the silencer is defined as the difference of the sound pressure levels measured at the fixed points between the two configurations of the straight duct and drum like silencer, respectively. In reality, the radiation from the loudspeaker and the fan is not an ideal dipole. It is evitable to extract the dipole part of the noise source from the real source during the signal processing. The radiated sound approaching the two openings is plane wave when the duct is long enough. Reflected sound is also scattered by the fan blades and the junctions, and combined with the radiation from the induced vibration of the membrane. Technically, it is very difficult to decompose all wave components in such a complex environment for the coupled system. Nevertheless, it is probable to model the whole coupled configuration of the cavity backed membrane and the fan as an equivalent source. We follow the decomposition procedure in (Huang, 2010), the radiation of the source is then considered to consist of two parts, one dipole with anti-phase relation in the upstream and downstream regions, and the other monopole with in-phase relation. The pressure component is a function of the reflection coefficient of the open ends, and the pressure ratio between the two microphones($p_{up}/p_{dn}$). The expressions are applied here, two kinds of IL are employed for the experiment, one for the raw data $p_{up}$ directly at upstream measurement point and the other for the dipole radiation $p_d$ after decomposition, written as

$$IL_{up} = 20\log_{10}\frac{\left|p_{up}\right|_{str}}{\left|p_{up}\right|_{memb}},\quad IL_{d} = 20\log_{10}\frac{\left|p_{d}\right|_{str}}{\left|p_{d}\right|_{memb}}, \tag{5.15}$$

where 'str' and 'memb' denote the data measured with the straight duct and the membrane type silencer, respectively.

### 5.5.3 Experimental results and discussions

In the first step, a small loudspeaker is used to simulate the dipole source instead of the fan. Roughly speaking, the comparisons between the predicted and the experimental result show a satisfactory agreement except for the very low frequency range of 100Hz to 250Hz and this confirms the validation of the numerical simulation. The curves seem to be smoother than those of the real fan as shown in Figures 5.7 and 5.8. This may be due to the pure sinusoidal signal by the generator compared with the noise components from the fan. Besides, there exist some fluctuations in the insertion loss spectrum at the low frequency range. The main reason possibly comes from 1) the damping at the lateral edges in the real configuration; 2) the minor difference of the tension on the four membranes and 3) the low frequency limit of the loudspeaker performance, which is too small to produce a good frequency response at low frequencies. The tension may not be the optimal value but for the purpose of the comparison only. The dashed straight line denotes a noise reduction of 20dB as a reference IL value.

Focusing now on the experimental data for the loudspeaker test, it can be noted in Figure 5.7(a) that the sound pressure level of the extracted dipole radiation for the straight duct configuration (dashed line) is mostly higher than that for the silencer with tensioned membranes (solid line), especially within the frequency range below 900Hz. The upper frequency limit is given as 1500Hz, which is slightly lower than the first high order cut on frequency of 1700Hz but at least covers the first three orders of the blade passing frequencies of the fan in the current study. The raw IL measured at the upstream point, $IL_{up}$ , shown in Figure 5.7(b) as the solid line, is compared with the prediction for the pure dipole model as indicated in dashed line. By and large, the experimental data agrees well with the calculation although some deviations occur at very low frequencies, especially at the first two trough points. Such difference may be attributed to the damping ratio in reality because the sound radiation is reduced by the damping, particularly at the lateral edges, and thereby IL increases. When the dipole extraction scheme is adopted, the IL of the dipole component, $IL_d$ , is exhibited as the solid line in Figure 5.7(c). It is obvious that the new curve is much closer to the numerical prediction in terms of the overall IL level and the spectral pattern except near f=300Hz. Such discrepancy also exists in the ducted fan measurement, and it is attributed to the whole system resonance. The noise abatement can reach an averaged value of 30 dB in the frequency range of 320Hz to

420Hz at a tension of T=0.15 (dimensional tension:220N).

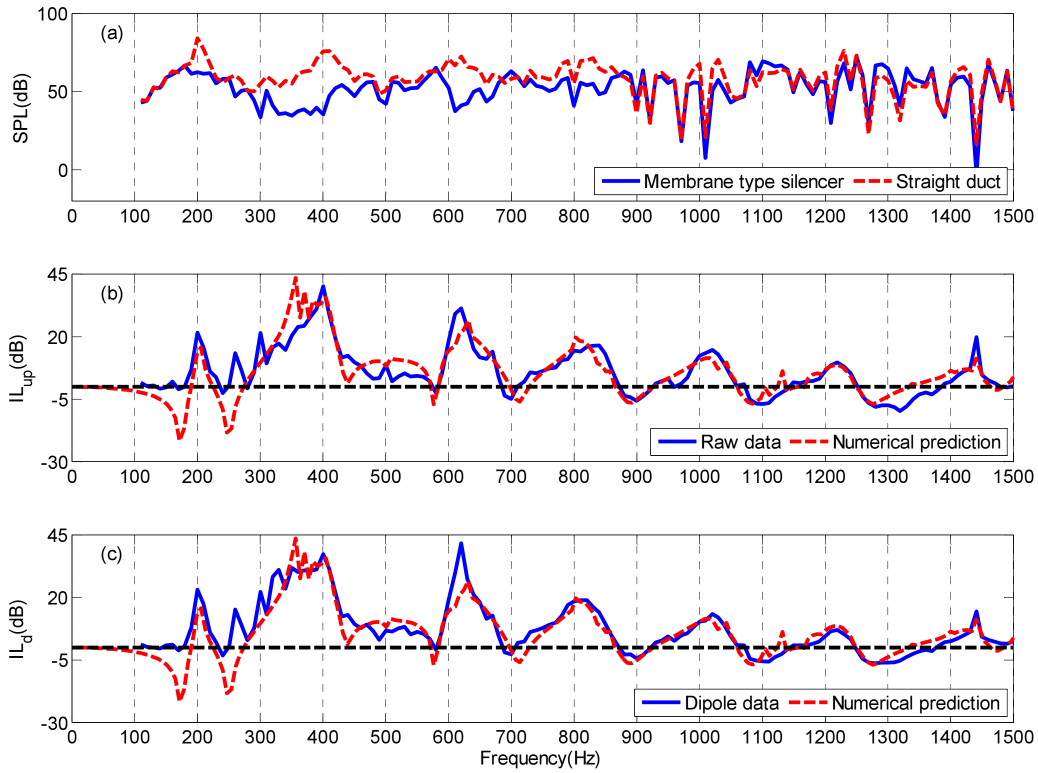


Figure 5.7 Comparison between the prediction and the experimental result for the loudspeaker as the dipole source (a) Spectra of the dipole sound radiation at the exits of both straight duct and the chamber duct (b) Comparison of the measured insertion loss at the upstream exit of the duct with the numerical prediction (c) Comparison of the same measured insertion loss after decomposition by the plane wave theory with the numerical prediction

Correspondingly, the experimental results for the fan test at the same tensile loading on the membrane are shown in Figure 5.8, which is presented similarly as Figure 5.7. The most prominent difference is the sharp peaks, which are the multiples of 400Hz in the present example, due to the blade passing events. The great difference appears at the first two blade passing frequencies of the fan in the sound pressure level spectrum

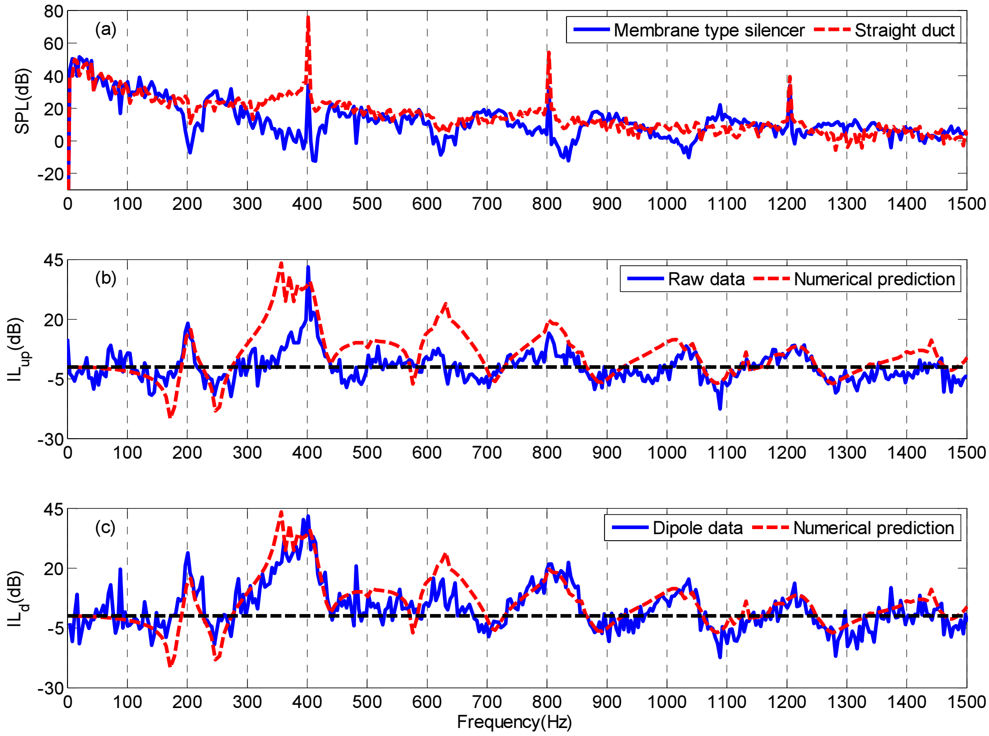


Figure 5.8 Experimental validation of radiated noise control of the real axial flow fan as the dipole source (a) Spectra of the fan noise radiation at the exits of both straight duct and the chamber duct (b) Comparison of the measured IL at the upstream exit of the duct with the numerical result (c) Comparison of the same measured IL after decomposition by the plane wave theory with the numerical prediction

in Figure 5.8(a), in which the noise is expected to be reduced. The raw IL for the upstream measurement point is compared against the prediction as shown in Figure 5.8(b). There is a broad agreement of the basic trend between the two but one difference occurs just below 400Hz. It is believed that such disagreement is mainly caused by the discrepancy between the simulation model of the dipole radiation and the real fan. This is further proved by Figure 5.8(c), where the dipole extraction procedure is executed. The experimental IL curve has much closer agreement with the prediction with regard to the overall level and the spectral pattern has been improved a lot. It is apparent that the fan noise can be suppressed successfully and significantly by 40 dB at the first BPF of 400 Hz, meanwhile by 20 dB at the second BPF of 800Hz as well.

## 5.6 Conclusion

This chapter emphasized on the experimental validation for the numerical simulations of the fan noise reduction by the silencer with tensioned membranes from a dipole point of view. The numerical methodology is briefly described in a 3D model, and the performance of the noise abatement is discussed for the acoustic configuration of both finite and infinite ducts. The experiment conducted in the real duct comprises two individual tests of different dipole sources, one being the loudspeaker and the other being the radiated noise from the axial flow fan. The following conclusions are derived from the results and the analysis.

(1) Based on the measured noise spectra of a real axial flow fan, the optimal performance of the noise reduction is investigated in the frequency range covering the blade passing frequencies with various rotational speeds. The numerical results imply that, for the current silencer with infinite length duct, the IL in the frequency range of interest achieves 10dB higher on average than that obtained by a pure expansion chamber.

(2) The good performance of the silencer directly results from the sound radiation control of the membrane by the dipole source. The radiation contribution towards outside is mainly determined by even modes of the induced membrane vibration, which reflects the dipole characteristic of the noise source. Such interactions between the sound and the membrane are related to the structural properties. .

(3) As for the real duct, it is finite with both ends open to the environment, thus the standing waves form at the upstream and downstream ducts due to the end impedance. The reflection has a pronounced effect on the IL pattern at high frequencies. As to the first real duct experiment, the result by using the loudspeaker as the dipole source has a good agreement with the predictions when the boundary condition of a real impedance is installed. Therefore, the numerical method is verified.

(4) For the practical application of the noise reduction on the axial fan, although the raw IL implies that the dipole characteristic of the fan noise is not ideal, the IL pattern is generally consistent with the predictions. Further, the agreement is considerably improved when the dipole component of the fan noise radiation is extracted from the raw data. It is found that the noise reduction can achieve about 40 dB and 20dB for the first and second blade passing frequencies, respectively. Besides, the optimal tension is found to be low so that it is easier to achieve and implement in practice.

# Chapter 6 Conclusions and recommendations

## 6.1 Conclusions

The features and mechanism of the flow-induced vibration of the tensioned membrane in the duct has been studied extensively. In addition, the feasibility of developing a silencer with the tensioned membrane to control noise source with flow has also been investigated. The configuration shares the feature of drum-silencer but the working principle to reduce noise and its usage are totally different. It is proved that such tensioned membrane can abate the axial fan noise radiation in the duct effectively. The axial fan is considered as the dipole sound source. The coupling between the dipole source, acoustic loading attributed to the backed cavity and the membrane has been investigated. The performance of such silencer has been studied numerically and experimentally.

In order to describe the phenomena of flow induced vibration, the characteristics of the wall pressure is examined to distinguish the aerodynamic and acoustic loadings under flow. These two components are resolved through the analysis of the correlation of the pressure fluctuation of any two points of the wall surface. By comparing the frequency range of the energy distribution of these two components in the pressure wave number frequency spectrum, it is found that the dominant excitation force on the membrane is aerodynamic and it becomes more obvious as the flow speed increases.

The flow-induced vibration of the tensioned membrane is characterized in terms of the critical flow velocity and the modes of vibration. In order to render the free boundary condition of the membrane, there is a very thin gap between two edges of the membrane and the surface of the duct walls. In this regard, there are two different aerodynamic excitation mechanisms. The air passing by the membrane in the axial direction is called axial-flow, and the flow leakage through the gap tangentially is named cross-flow. The occurrence of instable vibration was found when the flow speed exceeds a critical value. The critical flow speed was found experimentally for both air flow effect on the tensioned membrane. In particular, for the cross flow model, the experimental results of the critical velocities agree well with the modified predictions from the potential theory.

The modal vibration of the membrane was measured quantitatively. For the membrane with axial-flow, several peak frequencies can be observed obviously in the spectrum in case of flow-induced vibration. The peaks are attributed to the dominance of first and second mode of vibration. For the membrane with cross-flow, the higher order modes of vibration are found to be more obvious when the flow speed increases. In addition, the peak frequency will be higher when the tensile force in axial direction or the flow speed increases. Findings from the study of the flow-induced vibration provide guidelines on the design of membrane-type silencer.

On the other hand, the two-dimensional numerical model has been performed on the application of the silencer with tensioned membranes to dipole noise source control, in which the noise source is located at the center of the silencer along the axial direction. The optimization procedure aims to obtain the maximum stop-band of the noise reduction in the low frequency range below 500Hz. The frequency range is specified with the reference to the BPF of a real axial flow fan. The IL spectrum for an infinite length duct has been investigated, and at the optimal tension the noise reduction of 10 dB is reached over an octave band which covers the frequency of interest. The noise abatement of 10 dB refers to the maximum noise reduction obtained by the pure expansion chamber with the same cavity size as the silencer. The good performance results from the cancellation effect of the dipole controlled noise inside the cavity, while the sound penetration into the cavity is dependent on the structural impedance of the membrane. In contrast, no noise reduction occurs under the condition of strong radiation ability of the membrane vibration.

Finally, the experiments have been conducted on a real configuration of the axial flow fan with a cylindrical cavity covered by four tensioned membranes. A 3D numerical model has also been constructed for the accurate prediction. The simulation on the original fan has been modified to achieve the best dipole feature based on the theory. The total noise reduction in a specific frequency range has been optimized. And the frequency of interest is referred to the first BPF of the axial flow fan under different rotating speeds, e.g.250Hz to 500Hz. For the low frequency range, the noise reduction of the silencer outperforms that of the pure expansion chamber obviously by as much as 10 dB. Special designs at the lateral edges of the membrane have been considered concerning the instability findings. The experimental results from both loudspeaker and the fan noise as the dipole source show a satisfying agreement with the numerical predictions.

## 6.2 Suggestions for future studies

For the main work in this thesis, the first part focuses on the instable vibration of a flexible wall subjected to flow, which is essentially a fluid structure interaction problem. And the second part develops the application of the expansion chamber with tensioned membranes to a dipole noise source control. On the basis of the current study, future work can be carried out in the following areas to fully understand the mechanism of the vibration instability of a flexible panel under flow and to extend the control application of the dipole noise source in the duct system.

(1) As far as the instability of the flow past the flexible panel is concerned, the boundary conditions at leading and trailing edges of the panel play a vital role in the critical velocity results and vibration modes. The prediction of the critical velocity for the flow past a tensioned membrane is scarcely seen in the literature, particularly for a real flow condition. The theoretical model is expected to be of great help to illustrate

the complicated coupling among the flow, the structure vibration and even the sound.

(2) As for the cross flow past the membrane, it resembles the classical model of flow past the cantilevered free flexible panel to some extent. From the fluid point of view, the flow perturbation from the upstream will dramatically affect the critical velocity, such as a sharp leading edge. Disturbances from various upstream flow conditions consequently become important concerns that can be developed for the future studies.

(3) Although at least two cavity backed membranes are commonly used in parallel for the real configuration, the distance between the two panels may control the instability in the coupled system, in particular for a small distance where the flow is confined. When the two membranes have an angle deviation from each other, the confined flow may be limited in a tapered type.

(4) For the dipole noise control by the silencer with tensioned membranes, the sound source is located at the center of the configuration, and the sound propagation is controlled in a symmetric way. However, the interest can be focused on the location of the source since the noise reduction mainly results from the sound reflection and cancellation. The cancellation is dependent on the phase relationship of the propagated waves towards the upstream and downstream, while the phase relationship is determined by the change of the location. Therefore, a detailed study is

needed to illuminate the cancellation process with regard to the phase relationship.

(5) To facilitate the sound penetration into the cavity, helium will be filled inside the cavity. Helium gas does not only reduce the cavity mass and the tension but also greatly diminishes the cavity volume. This acoustical advantage is also expected to be effective in the new application.

(6) Similar to the development of the plate silencer, the replacement of the tensioned membrane by the plate can be adopted for further study on the control of the dipole noise source. The sound cancellation is expected to be very effective with the optimal structural impedance of the plate. The bending stiffness of the plate may not be very high according to the result of the low tension on the drum silencer. The pressure loss can also be eliminated by the uniform cross section of the duct.

# References

Abraham,B.M. and Keith,W.L.(1998), "Direct measurements of turbulent boundary layer wall pressure wavenumber frequency spectra," *Journal of Fluids Engineering,*Vol.120,29-39.

Ackermann, U. and Fuchs, H.V. (1989), "Noise reduction in an exhaust stack of a paper mill," *Noise Control Engineering Journal,* 33, 57-66.

Ackermann, U., Fuchs, H.V. and Rambausek, N. (1988), "Sound absorbers of a novel membrane construction," *Applied Acoustics ,*25, 197-215.

Agarwal N. K.(1992), " The sound field in fully developed turbulent pipe flow due to internal flow separation. I: Wall-pressure fluctuations," *Journal of Sound and Vibration,*Vol.169,No.1,89-109.

Alfredson, R.J.(1972), "The propagation of sound in a circular duct of continuously varying cross-sectional area," *Journal of Sound and Vibration,* Vol.23,433-442.

Arguillat,B., Ricot,D., Robert,G., and Bailly,C.(2005), " Measurements of the wavenumber frequency spectrum of wall pressure fluctuations under turbulent flows," *AIAA paper* 2005-2855.

Atig,M., Dalmont,J.P. and Gilbert,J.(2004), "Termination impedance of open ended cylindrical tubes at high sound pressure level," C. R. Acad. Sci. Paris, Series II,299-304.

Banichuk, N.,Jeronen, J.,Neittaanmaki, P.,Tuovinen, T.(2010), "On the instability of an axially moving elastic plate," *International Journal of Solids and Structures,*Vol.47,No.1,91-99.

Bennett,G.J.and Fitzpatrick,J.A.(2008), "Noise source identification for ducted fan system," *AIAA Journal*, Vol.46,No.7,1663-1674.

Bolt, Richard H. (1947), "On the design of perforated facings for acoustic materials," *Journal of the Acoustical Society of America*, Vol.19,No.5,Sep..

Bolton, J.S., Gardner, B.K., and Beauvilani, T.A.(1995), “Sound cancellation by the use of secondary multipoles,” *Journal of the Acoustical Society of America*, Vol.98,No.4, 2343-2362.

Brackenridge,J.B., Geib Jr,F.E., Maidanik,G. and Remmers,G.(1973), “Convection velocities of pressure fields on plane boundaries,” *Journal of the Acoustical Society of America*,Vol.54,No.5.

Bradshaw,P.(1967), “ Inactive motion and pressure fluctuations in turbulent boundary layers,”*Journal of Fluid Mechanics,* Vol.30,No.2,241-258.

Bull, M. K. (1996), “Wall-pressure fluctuations beneath turbulent boundary layers: some reflections on forty years of research,” *Journal of Sound and ibration,*Vol.190,No.3,299-315.

Bull,M.K. and Johnston,J.P.(1981), “Modal content of noise generated by a coaxial jet in a pipe,” *Journal of Sound and Vibration,* Vol.76,95-115.

Burg, J.P. (1967), “Maximum entropy spectral analysis,” *37th Annual Internat. SEG Meeting*, Oklahoma City.

Camussi,R.,Guj,G. and Ragni,A.(2006), “Wall pressure fluctuations induced by turbulent boundary layers over surface discontinuities,” *Journal of Sound and Vibration,* Vol.294 ,177 – 204.

Capone Dean E. and Gerald C.Lauchle(1995), “ Calculation of turbulent boundary layer wall pressure spectra,” *Journal of the Acoustical Society of America*, Vol.98,No.4,2226-2234.

Chang ,Y.B., Moretti, P.M.(1992), “An experimental study on edge flutter in webs,” *ASME Winter annual meeting*,Vol.149, 67-78.

Chang,Y.B., Moretti,P.M.(2002), “ Flow induced vibration of free edges of thin films,” *Journal of Fluids and Structures*,Vol. 16, No.7,,989-1008.

Chase, D.M. (1980), “Modelling the wavevector-frequency spectrum of turbulent boundary layer wall pressure,” *Journal of Sound and Vibration,* Vol.70,29-76.

Chase, D.M. (1987),“ The Character of the turbulent wall pressure spectrum at subconvective wavenumbers and a suggested comprehensive model,” *Journal of Sound and Vibration,* Vol.112,125-147.

Chase, D.M. (1991), “ The wave-vector-frequency spectrum of pressure on a smooth plane in turbulent boundary layer flow at low Mach number,” *Journal of the Acoustical Society of America*,Vol.90,No.2,August.

Chen,S.S.(1989), “Some issues concerning fluid elastic instability of a group of circular cylinders in cross flow,” *Journal of pressure vessel technology*, Vol.111, 507-518.

Chiu,Y.H., Cheng,L. and Huang，L.(2006), “Drum-like silencers using magnetic forces in a pressurized cavity,” *Journal of Sound and Vibration,* Vol. 297, No. 3-5, 895-915.

Choi Haecheon and Moin Parviz(1990), “ On the space time characteristics of wall pressure fluctuations,” *Physics of Fluids A,* Vol.2,No.8,1450-1460.

Choy, Y.S. and Huang,L.(2003), “Drum silencer with shallow cavity filled with helium, ” *Journal of the Acoustical Society of America*, Vol.114,No.3, Sep.

Choy, Y.S. and Huang,L.(2005), “Effect of flow on the drumlike silencer ,” *Journal of the Acoustical Society of America*, Vol.118,No.5, March.

Choy, Y.S. and Huang,L.(2009), “Multiple drumlike silencer for low frequency duct noise reflection,” *Applied Acoustics,* Vol.70,Issues 11-12, 1422-1430.

Choy, Y.S.,Huang,J., Huang L., Zhou,Y.(2007), “An experimental study of flow induced vibration on a tensioned membrane ,” *Journal of Mechanical Science and Technology,* Vol.21,1359-1366.

Chun Sejong, Liu Yingzheng and Sung Hyung Jin(2004), “ Wall pressure fluctuations of a turbulent separated and reattaching flow affected by an unsteady wake, ” *Experiments in Fluids,* Vol.37,537-546.

Corsini,A., Rispoli, F. and Sheard ,A.G.(2009), “Aerodynamic performance of blade tip end-plates designed for low-noise operation in axial flow fans, ” *Journal of Fluids Engineering*,Vol.131,081101,Aug.

Envia,E.(2001),"Fan Noise Reduction: An Overview, "*NASA Technical Memorandum 2001-210699,* Feb., 2-9.

Envia,E.，Wilson,A.G. and Huff,D.L.(2004), "Fan Noise: A Challenge to CAA, " *International Journal of Computational Fluid Dynamics* , Vol.18,No.6,471-480.

Farabee,T.M.and Casarella,M.J.(1991), "Spectral features of wall pressure fluctuations beneath turbulent boundary layers," *Physics of Fluids A,* Vol.3,No.10,2410-2420.

Farabee,T.M. and Geib,F.E.(1991), " Measurements of boundary layer pressure fluctuations at low wavenumbers on smooth and rough walls," *Proceedings of the ASME Symposium on Flow Noise Modelling, Measurement, and Control, Noise Control and Acoustics,* Vol.11,55-68.

Ffowcs Williams, J. E., and Hawkings, D. L.(1969). "Sound generation by turbulence and by surfaces in arbitrary motion," *Philos. Trans. R. Soc.London*, Ser. A 264, 321–342.

Finnveden,S., Birgersson,F., Ross,U. and Kremer T.(2005), "A model of wall pressure correlation for prediction of turbulence-induced vibration," *Journal of Fluids and Structures,* Vol. 20,1127-1143.

Frede, Shode(1966), "Wind screening of outdoor microphones," Bruel & Kjaer Technical Review.

Fuchs, H.V. (1993), "Sound absorbers for heavily fouling exhaust gas systems," *Cement Lime Gypsum 46*,E185-E191.

Frommhold, W., Fucks, H.V. and S.Sheng(1994), "Acoustic performace of membrane absorbers," *Journal of Sound and Vibration,* Vol.170,No.5,621-636.

Gerard,A., Berry,A. and Masson,P.(2005), " Control of tonal noise from subsonic axial fan. Part 2: active control simulations and experiments in free field ," *Journal of Sound and Vibration*, Vol.288,1077-1104.

Gerald.C.Lauchle and Mark A.Daniels(1987), " Wall pressure fluctuations in turbulent pipe flow," *Physics of Fluids,* Vol.30,No.10.

Gerhold,C.H.(1997), “Active control of fan generated tone noise,” *AIAA Journal*, Vol.35,No.1,17-22.

Griffin, S., Lane, S.A.,and Huybrechts, S. (2001), “Coupled Helmholtz resonators for acoustic attenuation ,” *Journal of Vibration and Acoustics,* Vol.123.

Guo,C., Paidoussis,M.P.(2000), “Stability of rectangular plates with free side-edges in two-dimensional inviscid channel flow, ” *Journal of applied mechanics- transactions of the ASME*, Vol.67,No.1, 171-176.

Gutin, L. (1948). “On the sound field of a rotating propeller,” *Zh. Tekh. Fiz. 6,* 899–909.

Hall,D.G. and Woodward,R.P.(1996), “Assessment of noise control measures for a model advanced ducted propulsor, ” *Journal of Aircraft*, Vol.33,No.3,May-June,505-510.

Howe,M.S.(1991), “ Surface pressures and sound produced by turbulent flow over smooth and rough walls ,” *Journal of the Acoustical Society of America*, Vol.90,No.2,August.

Howell, R.M., Lucey, A.D., Carpenter, P.W., Pitman,M.W.(2009), “ Interaction between a cantilevered free flexible plate and ideal flow ,” *Journal of Fluids and Structures*,25,2009,544-566.

Huang,L.(1995), “ Flutter of cantilevered plates in axial flow,” *Journal of Fluids and Structures,* Vol. 9, 127-147.

Huang, L.(1998), “Reversal of the Bernoulli effect and channel flutter,” *Journal of Fluids and Structures,*Vol.12,131-151.

Huang, L. (1999) “A theoretical study of duct noise control by flexible panel,” *Journal of the Acoustical Society of America*, 106, 1801-1809.

Huang, L.(2001), “ Viscous flutter of a finite elastic membrane Poiseuille flow,” *Journal of Fluids and Structures,*Vol.15,061-1088.

Huang, L.(2002), “Model analysis of a drumlike silencer,” *Journal of the Acoustical Society of America*,Vol.112,No.5, Nov.

Huang, L. (2003), “Characterizing computer cooling fan noise,” *Journal of the Acoustical Society of America*,Vol.114,No.6, Dec.,3189-3200.

Huang, L. (2004), “Parametric study of a drum-like silencer,” *Journal of Sound and Vibration*,Vol.269,No.3-5, Jan.

Huang, L. (2006), “Broadband sound reflection by plates covering side-branch cavities in a duct ,” *Journal of the Acoustical Society of America* ,Vol.119,No.5, May.

Huang, L. (2008), “Membrane covered duct lining for high-frequency noise attenuation: Prediction using a Chebyshev collocation method,” *Journal of the Acoustical Society of America* ,Vol.124,No.5, Nov,2918-2929.

Huang, L. and Choy, Y. S.(2005), “Vibroacoustics of three-dimensional drum silencer,” *Journal of the Acoustical Society of America*, Vol.118, No.4, Oct, 2313-2320.

Huang, L. ,Ma, X. and Feng, L.G.(2010), “Suppression of Broadband Noise Radiated by a Low-Speed Fan in a Duct ,” *Journal of the Acoustical Society of America*, Vol.128,No.1, Jul,152-163.

Huang, L. and Wang, J.(2005), “Acoustic analysis of a computer cooling fan,” *Journal of the Acoustical Society of America*,Vol.118,No.4, Oct,2190-2200.

Hudy Laura M. and Naguib Ahmed M.(2003), “ Wall pressure array measurements beneath a separating/reattaching flow region,” *Physics of Fluids,* Vol.15,No.3,706-717.

Huff, D. L.(2007)，“Noise Reduction Technologies for Turbofan Engines,” *NASA. Technical Memorandum*，14495, Sep.，1-10.

Josserand,M.A. and Lauchle,G.C.(1990), “Modeling the wave vector frequency spectrum of boundary layer wall pressure during transition on a flat plate,” *Journal of Sound and Vibration,* Vol.112,523-534.

Kang, J.and Fuchs H. V.(1999), “Predicting the absorption of open weave textiles and micro-perforated membranes backed by an air space,” *Journal of Sound and Vibration ,*Vol.220,No.5, 905-920.

Karvelis,A.V.(1975), “An experimental investigation of the wall pressure fluctuations in piping containing simple control devices,” Ph.D. Thesis, Pennsylvania State University.

Kim Joongny and Sung Hyung Jin(2006), “Wall pressure fluctuations and flow induced noise in a turbulent boundary layer over a hump”, *Journal of fluid mechanics*,Vol.558,79-102.

Kim, Yang-Hann and Seo, Sang-Hyun (2005), “Silencer design by using array resonators for low frequency band noise reduction,” *Journal of the Acoustical Society of America* ,Vol.118,No.4, Oct.

Kim, Sang Ryul , Kim , Yang-Hann and Jae-Hee Jang(2006), “A theoretical model to predict the low frequency sound absorption of a Helmholtz resonator array,” *Journal of the Acoustical Society of America* ,Vol.119,No.4, April.

Koopmann,G.H.,Fox,D.J. and Neise,W.(1988), “Active source cancellation of the blade tone fundamental and harmonics in centrifugal fans,” *Journal of Sound and Vibration*,Vol.126,No.2,Oct.,209-220.

Lai, J.C.S., Bullock, K.J. and Hollis, P.G. (1992), “Turbulence wave number spectra in fully developed smooth pipe flow,” *Experiments in Fluids,* Vol.12,No.6,369-376.

Lau, C. K. and Tang, S.K.(2005), “Sound transmission across duct constrictions with and without tapered sections,” *Journal of the Acoustical Society of America*,Vol.117,No.6, June.

Lauchle, G. C., Mac Gillivray, J. R. and Swanson . D. C. (1997), “Active control of axial-flow fan noise,” *Journal of the Acoustical Society of America*,Vol.101,No.1, Jan.

Lawrie, Jane B.(2010), “Acoustic propagation in 3-D, rectangular ducts with flexible walls,” *Noise -Con*, 240.

Leclercq, D. J. J. ( 1999), “ Modelisation de la reponse vibro-acoustique d’une structure couplee a une cavite en presence d’un ecoulement turbulent,” Ph.D. Thesis, Departement Genie Mecanique, Universite de Technologie de Compiegne.

Leclercq,D.J.J. and Bohineust,X.(2002), “Investigation and modelling of the wall pressure field beneath a turbulent boundary layer at low and medium frequencies,” *Journal of Sound and Vibration,* Vol.257,No.3,477-501.

Lee,I. and Sung, H.J. (1999), “Characteristics of wall pressure fluctuations in separated and reattaching flows over a backward-facing step,” *Experiments in Fluids,* Vol.30,262-272.

Lee,I. and Sung, H.J. (1999), “Development of an array of pressure sensors with PVDF film,” *Experiments in Fluids,* Vol.26,27-35.

Lee,I. and Sung, H.J. (2002), “Multiple-arrayed pressure measurement for investigation of the unsteady flow structure of a reattaching shear layer,” *Journal of Fluid Mechanics,* Vol.463,377-402.

Levine,H. and Schwinger,J.(1948), “On the radiation sound from an unflanged circular pipe,” *Physical Review*, Vol.73, No.4, Feb,383-406.

Lighthill, M. J. (1952). “On sound generated aerodynamically. I. General theory,” *Proc. R. Soc. London*, Ser. A 211, 564–587.

Lu,H.Z., Huang,L., So, R. M. C. and Wang, J.(2007), “A computational study of the interaction noise from a small axial-flow fan, ” *Journal of the Acoustical Society of America*, Vol.122,No.3, Sep.,1405-1415.

Lysak, Peter D. (2006), “Modeling the Wall Pressure Spectrum in Turbulent Pipe Flows,” *Journal of Fluids Engineering,* Vol.128,216-222.

Maa, D.Y. (1975), “Theory and design of micro-perforated panel sound absorbing constructions(in Chinese),” *Scientia Sinic 18*, 55-71.

Nijhof,M.J.J.,Wijnant,Y.H.,Boer,A.D.and Beltman,W.M.(2004), “Optimizing circular side-resonators to reduce computer fan noise，” *Noise-Con*, Jul.

Nijhof,M.J.J.,Wijnant,Y.H.,Boer,A.D.and Beltman,W.M.(2004), “Reduction of fan noise bymeans of (circular) side-resonators：theory and experiment,” *International Conference on Noise and Vibration Engineering, ISMA,* Sep., 20-22.

Oppenheim,A.V. and Schafer,R.W.(1975), “Digital signal processing,” *Prentice Hall, Englewood Cliffs*, New Jersey,553-554.

Qi, D., Aidun,C.K.(1995), “Free edge flutter based on 3D structural characteristics of paper,” *Journal of pulp and paper science and TAPPI engineering conference.*

Raman, A., Wolf, K., and Hagedorn, P.(2001), “Observations on the Vibrations of Paper Webs,” *Proceedings of the International Conference on Web Handling*, 415-439.

Tzou,K.I.,Wickert,J.A., Akay,A(1998), “ Frequency clusters in the spectrum of annular cylinders,” *ASME Journal of applied mechanics*,Vol.65, No.4,797-803.

Selamet, A., Xu, M.B.*and* Lee, I.-J. (2004), “Helmholtz resonator lined with absorbing material,” *Journal of the Acoustical Society of America*,Vol.117,No.2, Feb..

Stewart, P. S., Waters, S. L., Jensen, O. E.(2009) , “Local and global instabilities of flow in a flexible-walled channel,” *European Journal of Mechanics B-Fluids*,Vol. 28, No.4, 541-557.

Sewon Park, Gerald C.Lauchle(2009), “ Wall pressure fluctuation spectra due to boundary layer transition,” *Journal of Sound and Vibration,* Vol.319, No.3-5,1067-1082.

Sharland,I.J.(1964), “ Sources of noise in axial flow fans,” *Journal of Sound and Vibration*, Vol.1,No.3,302-322.

Sherman,C.H.,Ko,S.H. and Buehler,B.G.(1990), “Measurement of the turbulent boundary layer wave vector spectrum,” *Journal of the Acoustical Society of America*,Vol.88,No.1,386-390.

Sun, M.Z.(2007), “Smooth processing methods of vibration signal based on MATLAB,” *Electronic measurement technology,*30(6),Chinese Journal.

Tang, L., Paidoussis,M.P.(2009), “ The coupled dynamics of two cantilevered flexible plates in axial flow,” *Journal of Sound and Vibration*, 323,790-801.

Tang, S.K.and Lau.C.K.(2002), “Sound transmission across a smooth nonuniform section in an infinitely long duct,” *Journal of the Acoustical Society of America*,Vol.112,No.6, Dec.

Tran, Luu, Tung, Duong and Solomon, Latasha(2005), "Evaluation of microphone windscreen performance in a wind tunnel," *Report No.(s): AD-A443313; ARL-MR-0636*

Utsumi,M.(1999), "An efficient method for sound transmission in non-uniform circular ducts," *Journal of Sound and Vibration,* Vol.227,May,735-748.

Vaughan, M., Raman, A.(2010), " Aeroelastic stability of axially moving webs coupled to impressible flows," *Journal of applied mechanics- transactions of the ASME*, Vol.77,No.2.

Walker,B.E., Hersh,A.S., Heidelberg,L.J. ,Sutliff,D.L. and Spencer,M.E.(1999), "Active resonators for control of multiple spinning modes in an axial flow fan inlet," *AIAA* 99-1853,339-348.

Wang, Ch.Q.,Han J. and Huang,L.(2007),"Optimization of a clamped plate silencer," *Journal of the Acoustical Society of America*,Vol.121,No.2, Feb..

Wang, J. and Huang, L. (2006), "Active control of drag noise from a small axial flow fan," *Journal of the Acoustical Society of America*,Vol.120, No.1, Jan,192-203.

Wang, J., Huang, L. and Cheng, L.(2005), "A study of active tonal noise control for a small axial flow fan," *Journal of the Acoustical Society of America*, Vol.117,No.2, Feb.,734-743.

Watanabe, Y., Isogai, Y., Suzuki,S., and Sugihara, M.(2002), " A theoretical study of paper flutter," *Journal of Fluids and Structures* ,Vol.16,No.4, 543-560.

Watanabe,Y., Suzuki,S.,Sugihara,M., and Suroka,Y.(2002), " An experimental study of paper flutter," *Journal of Fluids and Structures*,Vol.16,No.4,529-542.

Welch, P.D.(1967), "The Use of Fast Fourier Transform for the Estimation of Power Spectra: A Method Based on Time Averaging Over Short, Modified Periodograms," *IEEE® Trans. Audio Electroacoustics,* Vol. AU-15, pp.70-73.

Willmarth,W.W.andWooldridge,C.E(1962), "Measurements of the fluctuating pressure at the wall beneath a thick turbulent boundary layer," *Journal of Fluid Mechanics,* Vol.14,No.2,187-210.

Wong,Y.J., Paurobally,R. and Pan,J.(2003), "Hybrid active and passive control of fan noise," *Applied Acoustics,* Vol.64,885-901.

Xu, M.B., Selamet, A., Lee, I.-J. and Huff, N.T. (2003), "Sound attenuation in dissipative expansion chambers," *Journal of Sound and Vibration,* Vol.272, July,1125-1133.

Yi, Sung-II and Lee, Byung-Ho (1986), "Three-dimensional acoustic analysis of circular expansion chambers with a side inlet and a side outlet," *Journal of the Acoustical Society of America*,Vol.79,No.5,May.